Electrochemical Processing in Molten Salt for In-Situ Resource Utilization

Yuta Suzuki

Contents

CHAPTER 1

General Introduction

1.1. A proposal on space exploration scenario after the International Space Station (ISS) program

1.1.1. Background

Many space agencies believe that the next frontier of humankind lies in deep space exploration after the ISS program concludes. Several projects have been planned to explore the possibility of human habitation on the moon and Mars [1–4]. Artemis is a well-known National Aeronautics and Space Administration (NASA) program with the goal to return humans to the moon in 2024 [5] and to realize a comfortable and sustainable stay for mission scientists, engineers, and astronauts. The program requires a small society, community, or village, like an Antarctic base observation station that significantly contributes to weather forecasting and global warming prediction supported by vast data acquisition over long periods of time. Such a space society, composed of a diverse assembly of mankind, should be governed by "International Space Law" supported by human morality created on Earth. Seven countries signed up for the Artemis Accords in October 2020: Australia, Canada, Italy, Japan, Luxembourg, the United Arab Emirates, and the United Kingdom.

In Japan, the Japan Aerospace Exploration Agency (JAXA) successfully sampled the Itokawa asteroid in 2005 and returned samples to Earth in 2010. The

Hayabusa spacecraft was used in this mission, through the successful application of an ion engine and constant scarify-like efforts on the telecommunication system driven through the charging/discharging operation of Li ion battery arrays. Regolith dust particles taken from the Itokawa asteroid surface were supplied to academic laboratories. Mineralogical, geochemical, petrographical, planetary chemical, and isotope ratio analysis is still in progress with the goal to create lunar-logy or to understand new evolution of the solar system. This mission was recognized as the first successful sample return from an asteroid. The Hayabusa 2 mission recently succeeded in bringing back more regolith sample from the Ryugu asteroid on Dec. 6th, 2020. After capsule separation, the spacecraft performed trajectory correction maneuvers three times every 30 min to depart from the Earth's atmosphere, from 15:30 to 16:30 on December 5 (JST). Hayabusa is to engage in an extended mission to 1998 KY26, a fast rotating asteroid, on which the spacecraft will arrive on July 2031.

JAXA anticipates that this sample analysis may "clarify the origin and evolution of the solar system, as well as life matter." JAXA is also planning to engage in a sample return mission, the Martian Moons eXploration (MMX), in which the most scientifically interesting minerals will be safely sampled from the Martian satellite of Phobos in the 2020s [6,7].

For long-term development on the moon and Mars, it is necessary to construct a new resource and energy system that enables an electrical power supply and propellant fuel for deep space flight missions. Since it is expensive to transport a large amount of energy resources on Earth to deep space, the in-situ utilization of space resources (ISRU) for generation of energy and a life supporting system is indispensable. The next section proposes a space exploration scenario based on electrochemical/materials processing as well as environmental science, mineral engineering, and nuclear fuel technology.

1.1.2. In-situ resource utilization (ISRU) for energy generation

JAXA anticipates a lunar base where roughly 10 to 100 people may stay approximately half a year, like “the Showa base” in the Japanese Antarctic Research Expedition program. The Showa base was constructed to begin global environmental observational research under the leadership of Profs. T. Nagata and E. Nishibori in 1957, the International Geophysical Year. It is noteworthy to describe their major achievements:

(1) The explication of the fluctuation history of the global environment by analysis of ice samples taken from the Antarctic deep glacier layer.
(2) The world largest collection of meteorite, including nine pieces from Mars.
(3) The acquisition of observation data linked to the discovery of an ozone hole.

The history of the Showa Antarctic base may provide suggestions for a space exploration scenario due to commonality in both projects: budget limitations estimated beforehand from the number of residents and residence periods.

According to the NASA Gateway project, a lunar surface radar survey mission may be engaged after the ISS program. This survey mission will select an appropriate base site, which will likely be near lunar holes where a large amount of ice water or hydrated minerals are expected to be stored. An oxide mineral wall in a vast rocky cavern may be utilized to reduce cosmic-ray radiation damage to the human body. Materials needed to construct the lunar base building, solar array panels, and energy storage devices, will be transported from Earth by JAXA’s future H-II transfer vehicle. The JAXA/Toyota lunar rover, operated by a fuel cell, will drive around the lunar hole with the goal of exploration and mining mineral and isotope resources to exploit. Microelectromechanical system (MEMS) sensor arrays, controlled with a neural network system, will collect multi-wave signals that reflect the small discontinuity of physical properties corresponding to mineral composition differences. Major targets should be the recovery of reactive metals like O_2 gas as deep space propellant fuel. Then, the electro-metallurgical processing of reactive metals, like Si, Ti, Al, Mg, Fe, and Ni, for self-propagated Si photovoltaic (PV) and lunar base construction materials will follow, as well as mining operations for ^{3}He fusion technology resources. Energy may also be supplied through a solar power satellite (SPS) energy transportation system linked with advanced Li ion and liquid metal battery energy storage technology. Even nuclear battery power generation could be effectively utilized.

Once, MEMS sensors installed in Lunar Rover may find out an appropriate base construction spot, it is necessary to construct a system of grinding, classification and separation as well as electrostatic levitation transportation of fine regolith powder through usage of the bottom of a vast lunar hole. Magneto-Archimedes levitation is one of the attractive techniques for separating process of fine regolith powder under low gravity environment. Regolith mineral processing provides the appropriate mineral oxides to supply molten oxide electrolytes as well as molten salt electrolytes.

ISRU to generate energy and to supply oxygen and lunar base construction materials is mandatory for sustainable space exploration. More than tens of residents are anticipated for this lunar base; before preliminary ISRU, the feasibility and economic aspects based on the scale or size of the lunar base must be evaluated to report to taxpayers. At this time, no official data of this type is available. The present research should be in conjunction with the "Moon Village" design primarily led by the European Space Agency (ESA). On the other hand, NASA has already planned the Lunar Surface Innovation

Initiative program that will develop and demonstrate technologies to use the moon's resources to produce water, fuel, and other supplies [9]. Furthermore, NASA is planning to demonstrate the production of oxygen from the Mars atmosphere (MOXIE: The Mars Oxygen In-Situ Resource Utilization Experiment) [10].

Two promising energy resources are being considered here: solar radiation for solar power and ^{3}He for nuclear power [1]. Solar power generation is possible for approximately 14 days (during daytime). Therefore, it is indispensable to construct solar cells from local lunar material to supply a self-propagating Si PV array system. The most promising candidate for solar cell materials is Si, which is abundant in the lunar regolith as SiO_2.

The other energy resource option is the utilization of nuclear power energy systems for approximately 14 days (during nighttime). ^{3}He is attractive as a nuclear fusion reactor resource but almost no lunar option is expected to practically operate the ITER ("The Way" in Latin) demonstration reactor (constructed in France), even in the next 20 years. Under such a severe situation, the introduction of a "kilo-power" nuclear reactor, which would provide the several tens of kilowatts of electrical power necessary to support the life of less than ten astronauts and is led by NASA and the Department of Energy National Nuclear Security Administration (The Kilopower project), may provide another option. For example, a nuclear battery with ^{238}Pu or ^{210}Po as a thermoelectric power conversion device was originally employed in deep space exploration projects of the 1960s.

Nuclear fission reactions to generate energy heat in the "kilo-power" reactor could be reasonably controlled by changing the location of a boron carbide rod, acting as a neutron absorber, in order to adjust the rate at which ^{235}U fission allows heat output to match the electrical energy load. ^{235}U is loaded on the ground in advance. The generated heat under careful control of highly fission products is carried to the Stirling converters through passive heat pipes. Passive heat pipes filled with liquid sodium immediately transfer the reactor-core heat to one or more free-piston Stirling engines. Liquid Na coolant freely flows without phase transition between 400 to 700°C. This is similar to Na coolant employed in the fast breeder reactor, Monjyu, in Japan. Serious accidents were reported for Monjyu in 1995 and one of the challenging technological targets is how to rationally design the physicochemical interfacial reaction between Na coolant and the steel pipe surface under pressure fluctuations. A Sterling engine is operated by the cyclic compression and expansion of a working gas at different temperatures, resulting in a net conversion of heat energy to the mechanical work. That is, the engine produces a reciprocal motion to drive a linear electric generator. This intrinsically safe principle, in a wide range of environments and scenarios, is adopted to this reactor design. Nuclear meltdown phenomena are uniquely mitigated by several feedback mechanisms, such as a passive cooling system without any mechanical circulating coolant and a self-regulating design creating a fuel negative temperature reactivity coefficient. Although the concept of a "kilo-power" nuclear fission reactor looks attractive in terms of safety, effectiveness, and efficiency, the interfacial corrosion reaction mechanism must be fully controlled for the long-duration operation encountered by the space program.

Therefore, the present author focuses solely on the physicochemical interfacial reactions encountered in the Si electrodeposition process and the corrosion or degradation phenomena between transition metal surfaces and molten salt or molten alkali metal coolants. The electrochemical/materials processing newly encountered in ISRU greatly contributes to the new frontier of high temperature science and technology. Figure 1-1 shows a schematic model of ISRU for energy generation on the moon or Mars. This figure assumes the existence of sufficient lunar regolith, lunar ice, and ^{3}He as natural resources on the moon. The cost evaluation discussion earlier, based on the scale of a lunar base, is now set aside while waiting for the ESA's Moon Village Design.

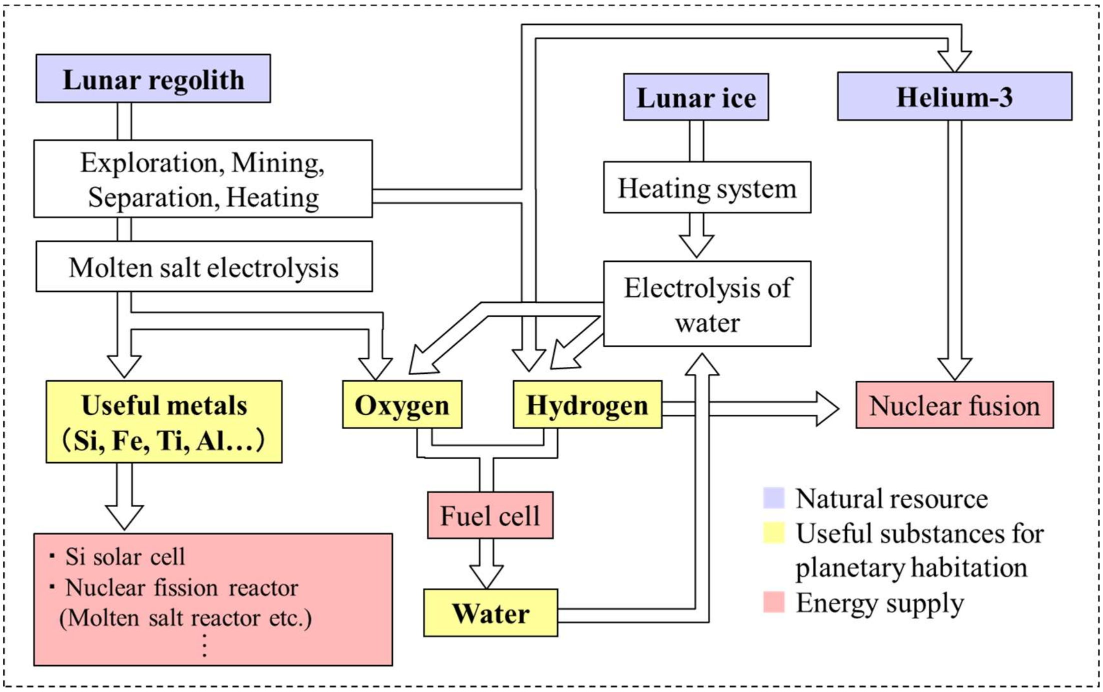

Figure 1-1. Schematic model of new resources and energy systems on the moon or Mars.

Mineral exploration using gamma ray spectroscopy has been employed by the petroleum industry on Earth. Each element is analyzed through the interaction of a high energy neutron colliding with an atomic nucleus, resulting in deaccelerated neutron density. This deacceleration phenomena becomes effective for hydrogen atoms with a similar mass of the neutron to generate captured gamma rays whose strength is related to the moisture component in the crust layer. This method may be applied to monitor or to detect ice water on the lunar surface. Rare-earth transition metal (RETM) alloy compound films electrodeposited in molten salt are utilized as neutron stratification detectors.

The mineral exploration program will likely be scheduled during the operation of the JAXA/Toyota lunar rover in 2029. The separation engineering program for lunar regolith will be drastically renovated based on the modern theory of electrostatic levitation or strong magnetic-field materials science without humidity. At the same time, CO_2 reduction and O_2 generation reactions, which are indispensable for life supporting systems with molten salt electrolysis processes, are also excluded in this thesis. Thus, the physicochemical interfacial phenomena encountered in power generation infrastructures, such as solar cells, fuel cells, and the “kilo-power” reactor under nuclear fission reactions, are examined to challenge the frontier of space engineering that is, ISRU.

1.2. Power generation by ISRU

1.2.1. Regolith sample

Resources for solar cells can be obtained from the lunar regolith. The regolith, which has been defined as “a general term for the layer or mantle of fragmental and unconsolidated rock material, whether residual or transported and of highly varied character that nearly everywhere forms the surface of the land and overlies or covers bedrock [11],” includes abundant mineral resources. Although the mineral composition is different depends on the place of lunar and Martian surface, major components have been estimated by sample survey and remote sensing. As shown in Table 1-1, the range of weight fractions of oxide components in the lunar regolith was determined by Apollo Project sample measurements [11]. The components in the Martian regolith were also analyzed using alpha particle X-ray spectra of Martian dust [12]. From Table 1-1, SiO_2 is the most abundant substance in both cases. In addition, it has been reported that fluorapatite ($Ca_5(PO_4)_3F$), which is a candidate for fluoride ion in molten salt, is existed at concentration of 3–3.8 wt% on the lunar regolith [13].

Table 1-1. Range of weight fractions of principal oxide components in lunar [11] and Martian [12] regolith, as determined from sample measurements.

Oxide	SiO_2	FeO	Al_2O_3	CaO	MgO	TiO_2	Na_2O
Lunar	43–47%	5–16%	13–27%	10–15%	6–11%	1–4%	< 1%
Martian	39–45%	17–21%	9–10%	6–7%	7–8%	～1%	2–3%

1.2.2. Si solar photovoltaic (PV) resources

Silicon, which is the main material for solar cells because of its intrinsic semiconductor characteristics, is abundant as SiO_2 in the lunar and Martian regolith, as shown in Table 1-1. In order to convert solar radiation energy into electrical power in space, Si solar cells will play a crucial role in outer space up to Mars flights (nuclear energy may be the more appropriate choice beyond Mars). The conventional terrestrial process of manufacturing solar grade Si is the Siemens process. In this process, a carbothermal reduction reaction of SiO_2 in an Elkem arc furnace produces metallurgical grade (MG) crude Si (so called MG-Si), which undergoes a chlorination process in a fluidized bed. Various chlorinated metal gaseous species are repeatedly distilled in several hundreds of distillation columns to purify to eleven-nine $SiCl_4$ (rectification process). Then, $SiCl_4$ gas is fed into a thermal decomposition reactor to grow poly-Si around a Si rod heater. Finally, the poly-Si is melted in a purified SiO_2 crucible in the Czochralski (CZ) doping process to get a Si single crystal rod, 450-mm in diameter for semiconductor devices. An extremely severe quality control principle is applied in these products. Silicon with rather poor quality excluded from this inspection as well as the refined Si exposed to slag-metal distribution equilibrium reaction over long period is supplied to the Si PV industry. It is almost impossible to adopt the complicated and energy intensive Siemens process on the lunar surface. Electrochemical/materials processing in molten salt may provide an alternative strategy to generate a self-propagated PV power generation system, as describe below in Section 1.3.

1.2.3. Nuclear energy resources for future technology

Nuclear batteries and the “kilo-power” reactor are two candidates for nuclear energy power generation on a lunar base. Nuclear fusion technology is still far beyond our present engineering capability, from a modern engineering level. ^{3}He is, nevertheless, a useful resource for ISRU for future energy generation options, as well as for terrestrial utilization once fusion reactor blanket damage phenomena is completely solved. The success of the blanket is key to confining the extremely hot plasma above 10^8 K over long durations of time. Now, the international project, ITER, is constructed in South France. An MIT group reported a possible design with a smaller fusion reactor, called “SPARC,” by applying a confinement technique using an advanced high-field, high temperature superconducting magnetic-field. Based on this conceptual design, with a 1.65 m major radius and 0.5 m minor radius operating at a toroidal field of 12 T and plasma current of 7.5 MA, 50–100 MW of fusion power, a fusion gain (Q) greater than two is predicted.

Although the availability of ^{3}He on Earth is limited, the total amount is estimated to be ~4×10^6 kg in the atmosphere and ~109 kg in the mantle [14], the moon has an abundance of ^{3}He because of solar wind. In addition, there is minor additional production by secondary particle interactions with surface elements due to solar and galactic cosmic rays via nuclear spallation [15].

From a long-term point of view, nuclear power sources will be more advantageous for permanently generating electric power. Energy generation on the moon can be expected by fusion reaction using abundant ^{3}He in the lunar regolith. In the early 1950s, a fusion reaction was investigated based on the deuterium (D) and tritium (T) fuel cycle (D-T fuel cycle), as shown in Eq. 1-1.

$$D + T \rightarrow {}^{4}He + {}^{0}n \tag{1-1}$$

Subsequently, two types of fusion reactions using ^{3}He were proposed. One is the so called second-generation fusion fuel based on the D-^{3}He cycle (Eq. 1-2).

$$D + {}^{3}He \rightarrow {}^{4}He + p \tag{1-2}$$

The other is the third-generation fusion fuel based on the ^{3}He-^{3}He cycle (Eq. 1-3).

$$^{3}He + {}^{3}He \rightarrow {}^{4}H + p + p \tag{1-3}$$

The ^{3}He-^{3}He reaction produces no neutrons. Thus, ^{3}He is a potential future clean energy resource on the moon, without the hazardous radiation produced by conventional nuclear power [16].

Nuclear batteries, on the other hand, has been utilized in the field of deep space engineering. Molten salt or liquid metal has been utilized as a battery coolant. Corrosion phenomena between the reactor wall and molten coolant is the most severe problem for both nuclear batteries and in the case of the “kilo-power” reactor.

1.3. Molten salt electrolysis for PVs, reactive metals, O_2 generation, and CO_2 reduction

The electrochemical technique for high temperature electrolytes is a promising method for recovering useful metallic materials and oxygen gas from mineral resources in the regolith. Many studies for extracting metals from lunar sediment by means of molten electrolysis have been reported [17–20]. Many research studies have used high temperature molten oxide as the electrolyte. Although this molten oxide electrolysis is an attractive method for metal recovery from an oxide, it is often technically difficult to construct robust electrolysis systems at severely high temperatures, in terms of physicochemical properties (such as electrical conductivity and viscosity), inert electrode materials, and structural materials.

Molten alkali halide is an attractive candidate as an electrolyte for metal recovery from the regolith. The wide electrochemical window of molten salt among decomposition limits of constituent salt components allows electrowinning of highly electropositive metals. The good thermal stability and generally low vapor pressure are well adopted to high temperature electrochemistry [21]. In addition, molten salt has the ability to dissolve many inorganic compounds such as oxides, nitrides, and carbides.

The design of the molten salt bath, electrode material, and structural material are important for addressing the electrochemical recovery of metallic materials. In this section, the principle of electrochemical reduction of metal oxide at the electrode/molten salt interface is first outlined. Subsequently, issues facing molten salt electrolytes and electrode materials is described.

1.3.1. Principle

The electrochemical processing in high temperature molten salt is an attractive method for manufacturing Si films directly from SiO_2. Figure 1-2 shows a schematic model of molten salt electrolysis for the recovery of useful metal from metallic oxide. In the process, the metallic oxide is first dissolved and metallic cations and oxide anions are formed, as shown by Eq. 1-4.

$$MO_x \rightarrow M^{2x+} + O^{2x-} \qquad (1\text{-}4)$$

Then, the metallic ions (M^{2x+}) are electrochemically reduced to an active metal at the cathode or substrate surface (Eq. 1-5). The oxide ions are electrochemically oxidized on a graphite anode to form carbon monoxide or carbon dioxide gas. However, by replacing the graphite anode with an inert anode, it is possible to generate oxygen gas instead of CO_2 from the evolution reaction (Eq. 1-6).

$$M^{2x+} + 2xe^- \rightarrow M \qquad (1\text{-}5)$$

$$2O^{2x-} \rightarrow x/2\ O_2 + 4xe^- \qquad (1\text{-}6)$$

On the lunar surface, the lunar regolith mainly includes metallic oxide and, in principle, each element can be selectively recovered by controlling the electrode potential.

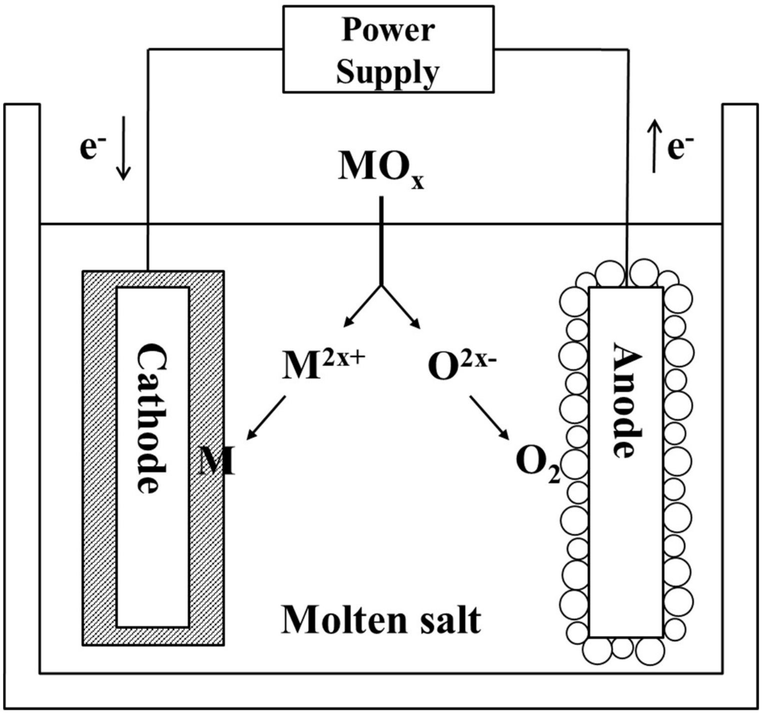

Figure 1-2. Principle of the production of metal (M) from oxide (MO_x) by molten salt electrolysis.

1.3.2. Molten salt electrolyte

Molten alkali halides are the simplest form of dissociated ionic melts, where cations are surrounded by anions and vice versa [22]. In particular, fluoride melts have several advantages, especially the ability to dissolve metallic oxides at lower temperatures. Therefore, it is possible to obtain crystalline Si on a cathode directly from SiO_2 by means of an electrochemical process [23]. In previous studies, fluoride melts were involved in three main research fields: the preparation of fluorine, experiments related to the molten salt nuclear reactor, and the industrial electrolytic production of aluminum [21]. The composition of the fluoride melt affects not only the operating temperature but also the solubility of the oxide and electrochemical behavior of metallic ions. Hence, an understanding of the interactions between ions formed by the dissolving oxide and constituent ions of the fluoride melt is important. However, only a few studies have been reported on the coordination structure of ions in fluoride melt.

1.3.3. Liquid metal electrode

Both solid and liquid metal electrodes can be employed as cathodes for metal recovery from regolith. Solid metal electrodes are much easier to use in melts than liquid electrodes. Liquid metal cathodes are a more feasible electrode material for the future when considering a continuous large-scale smelting process. Previously, the largest and most widespread use of liquid metal pool is the molten aluminum cathode (melting point is 660°C) using the Hall-Héroult process [24]. The interfacial phenomena of the liquid metal electrode/electrolyte have demonstrated close coupling phenomena between the reduction reaction rate and electromagnetic induced melt flow. This phenomenon has provided key opportunities to improve production efficiency at high current densities, exceeding 1 A cm^{-2}, in the fields of industrial smelting process. Such electromagnetic hydrodynamics, including current density distribution inside smelting electrolytic cells, has been analyzed experimentally and numerically from a macroscopic point of view [25] but without considering nucleation phenomena onto the liquid Al cathode.

From these developments in terrestrial and industrial processes, the author proposes a Si recovery process from lunar and Martian regolith using a liquid metal electrode, as shown in Fig. 1-3. In a cell under 1/6th or 3/8th G (G is the gravitational acceleration force level), Si is electrodeposited between the top layer of molten salt and the electrolyte/bottom layer of liquid metal substrates. The electrochemical behavior is often determined by coupling phenomena between the mass transfer rate and morphological variations at the electrolyte/electrode interface. Thus, electrochemical nucleation and growth phenomena at the liquid/liquid interface must be well controlled to create a unique interface in advanced extraction systems for metal recovery. Interfacial turbulence must be well understood to be controlled. Precise measurements of the physical properties of molten salt, especially of molten oxide, is required using an ISS electrostatic levitation furnace (ELF) facility because phase separation in the reactor is mandatory during smooth furnace operation. At the same time, O_2 gas bubble dispersion behavior on an advanced inert anode should be artificially designed, instead of CO_2 evolution onto a graphite anode. Dynamic wettability research at a three-phase interface, composed of O_2, molten salt, and an inert anode surface, is indispensable as well.

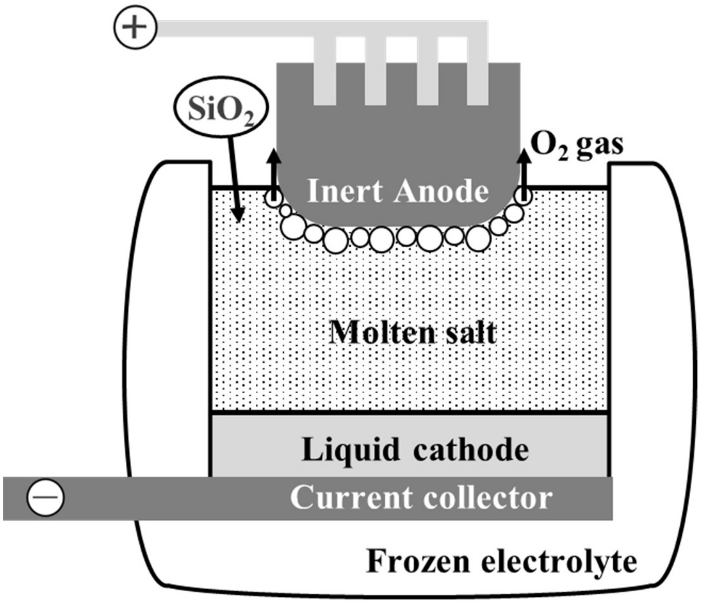

Figure 1-3. Recovery of useful metals in liquid phase on a liquid metal electrode.

1.4. Structural materials in molten salt

For long-term manned activities in space, it is also important to evaluate the durability of structural materials immersed in high temperature molten salt. Corrosion phenomena of structural materials in molten salts must be considered to construct a robust energy generation system using the molten salt electrolysis process and a liquid Na metal cooling system in the heat pipe involved in a “kilo-power” reactor. In general, corrosion of metals in molten salts generally occurs through electrochemical oxidation and the subsequent dissolution of metal atoms into the molten salt, which can be represented as:

$$M + Ox \rightarrow M^{n+} + Red \qquad (1\text{-}4)$$

where M is a metal atom, Ox is an oxidant species in the molten salt, and Red is the corresponding reductant [26]. It is easy to anticipate that the corrosion of metal at the structural material/high temperature molten salt interface progresses on the moon and Mars because of oxygen, which will be used for manned space activities and be generated from electrolysis of oxide as mentioned above. This will seriously corrode the structural material surface.

Structural materials that contact molten salt can be classified into two types: Fe-based material and a Ni-based material. In particular, JLF-1 steel (Fe-9Cr-2W, one of the reduced activation ferritic/martensitic (RAFM) steels) has recently attracted attention in the field of nuclear engineering.

1.5. Outline of this study

As described in the previous section, two types of power generation infrastructures, Si solar cells and nuclear fission (or fusion) reactors, are key technologies for manned space development. The performance of both systems inherently depends on electrochemical/materials processing in high temperature molten salt. Molten oxide electrolysis is indispensable for practical regolith research. Unfortunately, the acquisition of thermodynamic/electrochemical data for molten oxide is presently insufficient. Experiments with an electromagnetic/electrostatic levitator must be conducted in collaboration with JAXA and ESA.

At present, the molten halide system is challenged because of the vast data of achievements stemming from the Al smelting process. Fundamental information related to electrochemical reactions, such as metal electrodeposition and corrosion in high temperature molten halides, is needed for the design of entire power generation systems. In the present thesis, the author investigated the melt structure, electrodeposition process, and corrosion phenomena of structural materials in high temperature molten halide. The outline is as follows, chapter by chapter.

In Chapter 2, a brief explanation of experimental procedures is described. Details of the reagent and measurement systems used in the thesis are included.

Chapter 3 deals with Si electrodeposition in fluoride melt for manufacturing Si film as solar cell material. Specifically, the effect of O^{2-} ions on the coordination structure of silicon ions and the electrodeposition process of Si films in fluoride melt is discussed. In this section, both high temperature Raman spectroscopy and electrochemical measurements are carried out. The characteristics of electrodeposited Si films, such as thickness and current efficiency, are measured by X-ray diffraction (XRD), scanning electron microscopy (SEM), and energy dispersive X-ray spectroscopy (EDS), to discuss the Si electrodeposition process for fabricating high-quality Si layers. Chapter 4 describes the melt structure of fluoride added to SiO_2 for designing optimized molten salt electrolytes for silicon electrodeposition. In order to identify the interactions between silicon ions and constituent ions of the fluoride melts, high temperature Raman spectroscopic data are characterized by density functional theory calculations.

The experimental results of liquid metal cathodes from the standpoint of fundamental interfacial phenomena are presented in Chapter 5. To visualize the interfacial flow phenomena during the electrodeposition process, low temperature aprotic electrolyte and low melting point metal are used as a cathode. In-situ observation is made at the liquid Ga metal/propylene carbonate interface during lithium electrodeposition. The difference between the interfacial phenomena on the solid and liquid Ga substrate is discussed to clarify the relationship between the phase transition process and interfacial flow phenomena.

Chapter 6 describes the corrosion phenomena of major pure metals and alloys as structural materials in chloride melt. The corrosion rate is estimated by electrochemical measurements.

Chapter 7 focuses on JLF-1 steel as a robust structural material for a nuclear fission (or fusion) reactor. In order to clarify macroscopic and microscopic corrosion behavior, electrochemical impedance analysis and electron microscopy are carried out on JLF-1 steel and constituent metals.

The general conclusions of the above experimental and theoretical calculation results are included in Chapter 8.

References

[1] D. Kornuta, A. Abbud-Madrid, J. Atkinson, J. Barra, G. Barnhard, D. Bienhoff, B. Blair, V. Clarkg, J. Cyrus, B. DeWitt, C. Dreyer, B. Finger, J. Goff, K. Ho, L. Kelsey, J. Keravala, B. Kutter, P. Metzger, L. Montgomery, P. Morrison, C. Neal, E. Otto, G. Roesler, J. Schier, B. Seifert, G. Sowers, P. Spudis, M. Sundahl, K. Zacny, G. Zhu, "Commercial lunar propellant architecture: A collaborative study of lunar propellant production", REACH-Rev. Human Space Expl., **13**, 100026 (2019).

[2] M. Ishikawa, "The Unified Scientific Program of Space Environment Utilization and Human Planetary Habitation", Int. J. Microgravity Sci. Appl., **34**, 340303 (2017).

[3] V. Stamenković, L. W. Beegle, K. Zacny, D. D. Arumugam, P. Baglioni, N. Barba, J. Baross, M. S. Bell, R. Bhartia, J. G. Blank, P. J. Boston, D. Breuer, W. Brinckerhof, M. S. Burgin, I. Cooper, V. Cormarkovic, A. Davila, R. M. Davis, C. Edwards, G. Etiope, W. W. Fischer, D. P. Glavin, R. E. Grimm, F. Inagaki, J. L. Kirschvink, A. Kobayashi, T. Komarek, M. Malaska, J. Michalski, B. Ménez, M. Mischna, D. Moser, J. Mustard, T. C. Onstott, V. J. Orphan, M. R. Osburn, J. Plaut, A.-C. Plesa, N. Putzig, K. L. Rogers, L. Rothschild, M. Russell, H. Sapers, B. Sherwood Lollar, T. Spohn, J. D. Tarnas, M. Tuite, D. Viola, L. M. Ward, B. Wilcox, R. Woolley. "The next frontier for planetary and human exploration", Nature Astronomy, **3**, 116 (2019).

[4] W.X. Wan, C. Wang, C.L. Li, Y. Wei, "China's first mission to Mars", Nature Astronomy, **4**, 721 (2020).

[5] M. E. Evans, L. D. Graham, "A Flexible Lunar Architecture for Exploration (FLARE) supporting NASA's Artemis Program", Acta Astronautica, **177**, 351 (2020).

[6] S. Takahashi, N. Ogawa, Y. Kawakatsu, "General Characteristics of Free-Return Ensured Orbit Insertion and Trajectory Design with MOI Robustness in MMX Mission",

Trans. JSASS Aerospace Tech. Japan, **63**, 212 (2020).

[7] Y. Shimizu, H. Kamiyoshihara, T. Nihara, H. Miyamoto, “Experimental Study to Determine the Best Compression Ratio of High-Resolution Images of Small Bodies for the Martian Moons eXploration Mission”, Trans. Japan Soc. Aero. Space Sci, **17**, 404 (2019).

[8] M. F. Palos, P. Serra, S. Fereres, K. Stephenson, R. González-Cinca, “Lunar ISRU energy storage and electricity generation”, Acta Astronautica, **170**, 412 (2020).

[9] J. Vickers, “Lunar Infrastructure and Surface Operations”, ISS R&D Conference: Materials Science in Space Workshop, (2019).

[10] F. E. Meyen, M. H. Hecht, J. A. Hoffman, the MOXIE Team, “Thermodynamic model of Mars Oxygen ISRU Experiment (MOXIE)”, Acta Astronautica, **129**, 82 (2016).

[11] G. H. Heiken, D. T. Vaniman, B. M. French, Lunar Source Book, Cambridge University Press (1991).

[12] J. A. Berger, M. E. Schmidt, R. Gellert, J. L. Campbell, P. L. King, R. L. Flemming, D. W. Ming, B. C. Clark, I. Pradler, S. J. V. VanBommel, M. E. Minitti, A. G. Fairén, N. I. Boyd, L. M. Thompson, G. M. Perrett, B. E. Elliott, E. Desouza, “A global Mars dust composition refined by the Alpha-Particle X-ray Spectrometer in Gale Crater”, Geophys. Res. Lett., **43**, 67 (2015).

[13] L. H. Fuchs, “Fluorapatite and other accessory minerals in Apollo 11 rocks”, Proceedings of the Apollo11 Lunar Science Conference, **1**, 475 (1970).

[14] H.E. Johnson, W.I. Axford, “Production and loss of ^{3}He in the Earth's atmosphere”, J. Geophys. Res., **74**, 2433 (1969).

[15] L. J. Wittenberg, E. N. Cameron, G. L. Kulcinski, S. H. Ott, J. F. Santarius, G. I. Sviatoslavsky, I. N. Sviatoslavsky, H. E. Thompson, “A Review of ^{3}He Resources and

Acquisition for Use as Fusion Fuel", Fusion Technol., **21** 2230 (1992).

[16] K. J. Kim, C. Wohler, A. A. Berezhnoy, M. Bhatt, A. Grumpe, "Prospective ^{3}He-rich landing sites on the Moon", Planetary and Space Science, **177**, 104686 (2019).

[17] G. S. Jackson, S. Elangovan, P. E. Hintze "Electrochemical Approaches to "Living off the Land" in Space", Electrochem. Soc. Interface, **29**, 65 (2020).

[18] A. Liu, Z. Shi, X. Hu, B. Gao, Z. Wang, "Lunar Soil Simulant Electrolysis Using Inert Anode for Al-Si Alloy and Oxygen Production", J. Electrochem. Soc., **164**, H126 (2017).

[19] S. S. Schreiner, L. Sibille, J. A. Dominguez, J. A. Hoffman, "A parametric sizing model for Molten Regolith Electrolysis reactors to produce oxygen on the Moon", Adv. Space Res., **57**, 1585 (2016).

[20] C. Schwandt, J. A. Hamilton, D. J. Fray, I. A. Crawford, "The production of oxygen and metal from lunar regolith", Planet. Space Sci., **74**, 49 (2012).

[21] F. Lantelme, D. Inman, D.G, Lovering, Molten Salt Techniques, Vol. 2, R. J. Gale and D. G. Lovering, Ed., Plenum Press, New York (1984).

[22] E. T. Turkdogan, Physical Chemistry of High temperature Technology, Academic Press, New York (1980).

[23] Y. Sakanaka, T. Goto, "Electrodeposition of Si film on Ag substrate in molten LiF–NaF–KF directly dissolving SiO_2", Electrochim. Acta, **164**, 139 (2015).

[24] W. E. Cowley, Molten Salt Technology, D. G. Lovering, Ed., Plenum Press, New York (1982).

[25] R. Moreau, J. W. Evans, "An analysis of the hydrodynamics of aluminum reduction cells", J. Electrochem. Soc., **131**, 2251 (1984).

[26] S. W. Mcalpine, N. C. Skowronski, W. Zhou, G. Tony, M. P. Short, "Corrosion of

commercial alloys in FLiNaK molten salt containing EuF_3 and simulant fission product additives", J. Nucl. Mater., **532**, 151994 (2020).

CHAPTER 2

Experimental Procedures

2.1. Reagents

Reagents for the molten salts used in this thesis are as follows: lithium fluoride (LiF, purity: 98.0%, FUJIFILM Wako Pure Chemical Corporation), sodium fluoride (NaF, purity: 99.0%, FUJIFILM Wako Pure Chemical Corporation), potassium fluoride (KF, purity: 99.0%, FUJIFILM Wako Pure Chemical Corporation), calcium chloride ($CaCl_2$, purity: >99.9%, Kojundo Chemical Laboratory Co., Ltd.), and sodium chloride (NaCl, purity: 99.5%, FUJIFILM Wako Pure Chemical Corporation). The reagents were mixed in various compositions depending on each experiment and then the mixtures were kept under vacuum for more than 48 h at 473 K to eliminate any water. Silicon dioxide (SiO_2, purity: 98.0%, FUJIFILM Wako Pure Chemical Corporation) and lithium oxide (Li_2O, purity: 99.0%, FUJIFILM Wako Pure Chemical Corporation) were used as silicon ion and oxide ion sources in Chapters 3 and 4. In Chapter 5, propylene carbonate (PC, purity: 98.0%, FUJIFILM Wako Pure Chemical Corporation) containing various concentrations of lithium perchlorate ($LiClO_4$, purity: 98.0%, FUJIFILM Wako Pure Chemical Corporation) or silicon tetrachloride ($SiCl_4$, purity: >99.0%, FUJIFILM Wako Pure Chemical Corporation) was used as the electrolyte. For the PC-$SiCl_4$ system, tetrabutylammonium hexafluorophosphate ($TBAPF_6$, purity: >95%, FUJIFILM Wako Pure Chemical Corporation) was used as the supporting electrolyte.

2.2. Measurements and analyses

2.2.1. Electrochemical measurements

A potentiostat/galvanostat (VSP, BioLogic) was used for all electrochemical measurements. All measurements were performed using the three-electrode method under a dry Ar atmosphere.

2.2.2. Surface analysis

- X-ray diffraction (XRD)

An X-ray diffractometer (MultiFlex, Rigaku Corporation) was used to determine a sample composition or crystalline structure in Chapters 4-6. The sample was fixed on the stage and the counter was rotated to produce a given incident angle. The diffraction intensity versus 2θ was recorded. The X-ray was Cu Kα radiation operated at 40 kV and 20 mA.

- Micro-Raman spectroscopy

A micro-Raman spectrometer (LabRAM HR Evolution, Horiba Jobin-Yvon GmbH) with a YAG laser (532 nm) was used in order to identify the coordination structures of silicon ions in molten salt in Chapters 3 and 4. The average output power of the laser was 20 mW (the power density was approximately 2.8 MW cm^{-2}). The Raman spectra were acquired with a 600 gr mm^{-1} grating.

- Scanning electron microscopy (SEM) and energy dispersive X-ray spectroscopy (EDS)

SEM (JSM-7001FD and JSM-5600, JEOL Ltd.) with EDS (JED-2300, JEOL Ltd.) was carried out to observe sample surface morphology in Chapters 4 and 7.

- Glow discharge optical emission spectroscopy (GD-OES)

GD-OES (GD-Profiler2, HORIBA, Ltd.) was used in order to determine the weight fraction of constituent elements in alloy samples in Chapter 6.

- Transmission electron microscope (TEM)

TEM (JEM-2800, JEOL Ltd.) with EDS (JED-2300, JEOL Ltd.) was used in order to reveal microscopic corrosion phenomenon of JLF-1 steel in Chapter 7.

2.2.3. Density functional theory (DFT) calculation

In Chapter 4, DFT calculations with the B3LYP/6-311+G(d) hybrid exchange-correlation functional/basis set framework were carried out in order to optimize geometric structures and determine vibrational modes of Si oxyfluorides. In the calculations, the Gaussian 09 (Revision B. 01) package was used.

2.2.4. Thermal analysis

Thermal properties of the KF-SiO_2 binary system were investigated by thermogravimetry and differential thermal analysis (TG-DTA, DTG-60H, SHIMADZU CORPORATION). The measurement was performed in a dry Ar gas environment.

CHAPTER 3

Effects of Oxide Ions on the Electrodeposition Process of Silicon in Molten Fluorides

3.1. Introduction

There is currently a major focus in the field of Si solar cells on the fabrication of Si films by environmentally friendly and inexpensive processes. The molten salt electrochemical process is a key technology for fabricating polycrystalline Si thin films in an environmentally friendly, simple, and inexpensive manner. In this process, the morphology, crystallinity, and texture of electrodeposited Si can be easily controlled by changing melt conditions and electrochemical parameters, such as applied potentials and current densities.

Since the 1970s, the electrodeposition of Si by a high temperature molten salt electrochemical process has been studied in various molten fluorides, such as LiF-KF [1–4] and LiF-NaF-KF [5,6] containing K_2SiF_6 systems. Subsequently, other fluoride systems, such as NaF-KF [7] and NaF-AlF_3 [8] have also been reported. Since the 2000s, the direct electrochemical reduction of bulk SiO_2 [9–11] and SiO_2 nanoparticles [12–15] in molten $CaCl_2$ at 1123 K has been studied. Recently, the electrodeposition of Si from $SiCl_4$ in molten KF-KCl at 923 K has been reported [16].

In a previous study, the authors examined the electrodeposition of Si in molten LiF-NaF-KF containing SiO_2 powder at 873 K [17]. The authors obtained dense and adherent polycrystalline Si films, with thicknesses of 1–2 μm, by potentiostatic electrolysis. Compared to the molten chloride system, one of the benefits of the molten fluoride system is its high solubility for SiO_2 at a low temperature. Although the solubility process of SiO_2 is an important step for the electrodeposition of Si films, only a few studies have examined the coordination structure of silicon ions in molten fluorides by in-situ measurements. In particular, because certain studies have proposed that the solubility of SiO_2 is enhanced by adding O^{2-} ions in a chloride system [14,15], it is necessary to understand the effects of O^{2-} ions on the coordination structure of silicon ions and electrodeposition process of Si in molten fluorides.

In this chapter, the author examines the dissolution behavior of SiO_2 powder in molten fluorides with and without a Li_2O system using spectroscopic techniques. Li_2O is used as a source of O^{2-} ions. First, molten KF is used as a simple electrolyte to reveal the interaction between KF and SiO_2. The phase diagram of the KF-SiO_2 binary system is described by thermogravimetry and differential thermal analysis (TG-DTA). Using high temperature Raman spectroscopy, which is a useful technique for determining the coordination structure of silicate ions [18], the coordination structure of silicon ions in eutectic KF-SiO_2 is examined. The differences between the coordination structures of silicon ions in the molten LiF-KF and LiF-NaF-KF system, with and without Li_2O, are then discussed. Furthermore, electrodeposition of Si by potentiostatic electrolysis was performed in molten LiF-NaF-KF, with and without Li_2O, at 873 K to examine the effects of O^{2-} ions on the Si electrodeposition process. Then, the electrodeposited Si layers on Ag substrates were characterized using SEM, EDS, and XRD.

3.2. Experimental

LiF (98.0%, FUJIFILM Wako Pure Chemical Corporation), NaF (99.0%, FUJIFILM Wako Pure Chemical Corporation), KF (99.0%, FUJIFILM Wako Pure Chemical Corporation), SiO_2 (99.0%, FUJIFILM Wako Pure Chemical Corporation), and Li_2O (99.0%, FUJIFILM Wako Pure Chemical Corporation) were used as the starting materials. Depending on the experimental conditions, these reagents were then mixed into various compositions. The mixtures were kept under vacuum for more than 48 h at 473 K to eliminate any water.

For the calorimetry studies, KF and SiO_2 powder were mixed by mechanical grinding using a mortar and pestle for over 5 min to obtain a homogeneous mixture. The melting points of the KF-SiO_2 mixture were measured using TG-DTA (DTG-60H, SHIMADZU CORPORATION). The phase diagram of the binary KF-SiO_2 salt mixtures was constructed by plotting the temperatures of endothermic peaks identified on the DTA curves, obtained in the heating process, to avoid uncertainty because of supercooling.

For the Raman spectroscopic analysis, LiF, KF, SiO_2, and Li_2O powders, mixed in various compositions and subject to a drying process, were introduced into a platinum crucible. The crucible was sealed in a hot stage device (10016, Japan HighTech Co., Ltd.) and continuously heated at 100 K min^{-1} under an Ar atmosphere. Raman spectra were obtained using a micro-Raman spectrometer (LabRAM HR Evolution, Horiba Jobin-Yvon GmbH) with a YAG laser (532 nm).

Figure 3-1 shows a schematic illustration of the electrochemical cell and Fig. 3-2 illustrates the electrode configuration employed in Chapter 3. For the electrochemical experiments, all measurements were performed under a dry Ar atmosphere. The cell was heated using a programmable furnace and the temperature of the cell was measured using a chromel-alumel thermocouple with an accuracy of ±1 K. Ag wires (99.99 %, 1-mm diameter, The Nilaco Corporation) and Ag plates (99.5 %, 5 mm × 8 mm × 0.5 mm, The Nilaco Corporation) were used as the working electrodes. The potentials of the electrodes were measured using a nickel wire immersed in a molten electrolyte, which acted as a quasi-reference electrode (QRE). The potential of the Ni QRE was calibrated with respect to a K^+/K electrode, which was prepared by electrodepositing K metal on a Ni electrode. The counter electrode was a glassy carbon rod (3-mm diameter, TOKAI CARBON Co., Ltd.). A potentiostat/galvanostat (VSP, BioLogic) was used for electrochemical measurements.

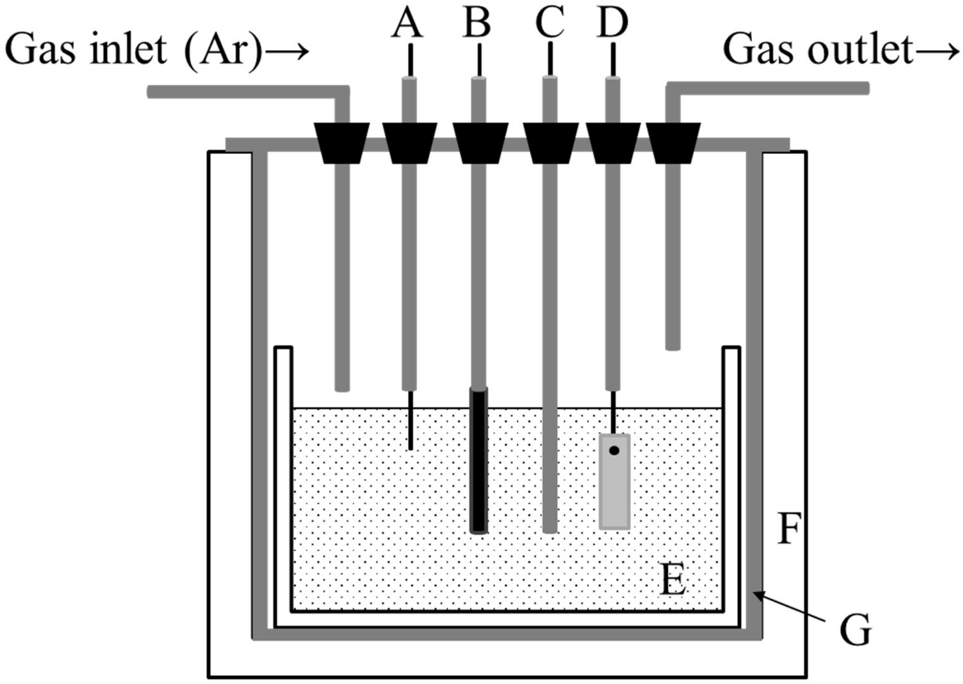

A: Quasi-reference electrode (Ni)
B: Counter electrode (glassy carbon)
C: Thermocouple
D: Working electrode (Ag)
E: Electrolyte (LiF-NaF-KF melt)
F: Electric furnace
G: Stainless steel holder

Figure 3-1. Schematic illustration of the electrochemical cell.

Working electrode

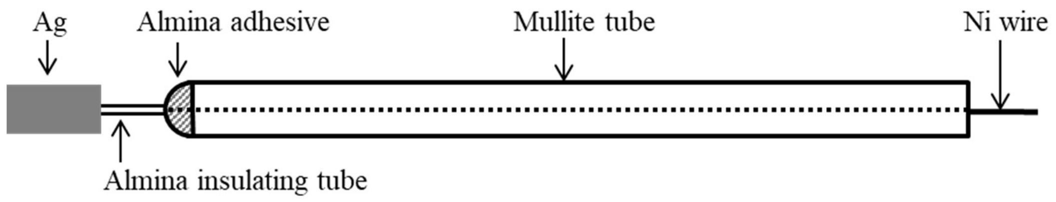

Counter electrode

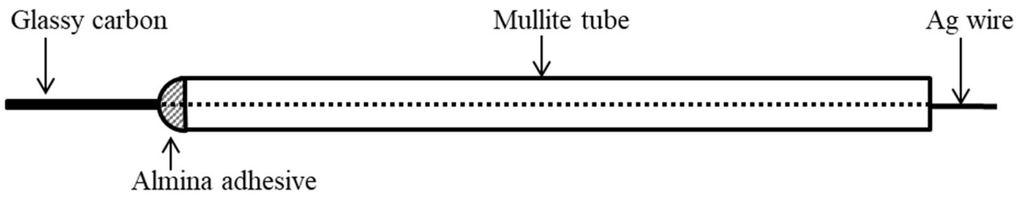

Quasi-reference electrode

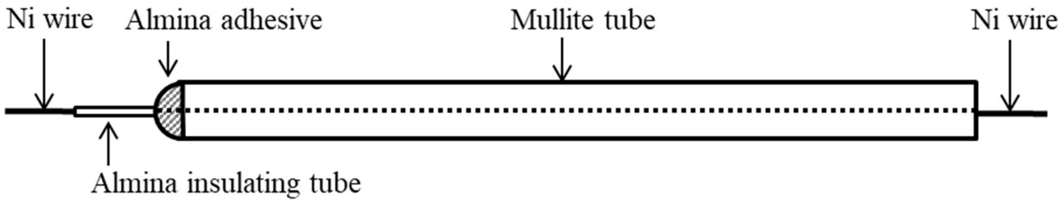

Figure 3-2. Schematic illustrations of the working electrode, counter electrode, and quasi-reference electrode.

All Si samples were prepared by potentiostatic electrolysis and rinsed with water heated to 363 K for more than 6 h. The obtained samples were analyzed by XRD (MultiFlex, Rigaku Corporation) with a Cu Kα line and SEM (JSM-7001FD, JEOL Ltd.). Cross-sectional samples were prepared using a cross-sectional polisher.

3.3. Results and discussion

3.3.1. Coordination structure of silicon ions in a KF-SiO_2 system

In order to investigate the dissolution behavior of SiO_2 powder in molten fluoride systems, KF single melt was selected as the simple fluoride melt. To examine the thermal properties of the KF-SiO_2 system, the melting points at various mole fractions of the KF-SiO_2 were measured using TG-DTA. Figure 3-3 shows the phase diagram of the KF-SiO_2 binary system. These data were collected by continuous heating at 10 K min^{-1} for the TG-DTA measurement for a scan rate sufficiently capable to detect the transition temperature. The phase diagram was a simple eutectic type and the eutectic composition of the KF-SiO_2 system was 50 mol% KF at a temperature of 993 K. This temperature was 990 K lower than the melting point of SiO_2, which indicates that SiO_2 can be dissolved into a new coordination structure of silicon ions by interactions with KF molecules. The eutectic composition determined in the measurement agreed with that reported in a previous study [19]. However, the temperature used in the current study was 73 K lower than the value reported in [19], which might be caused by the difference in sample preparation for DTA measurements.

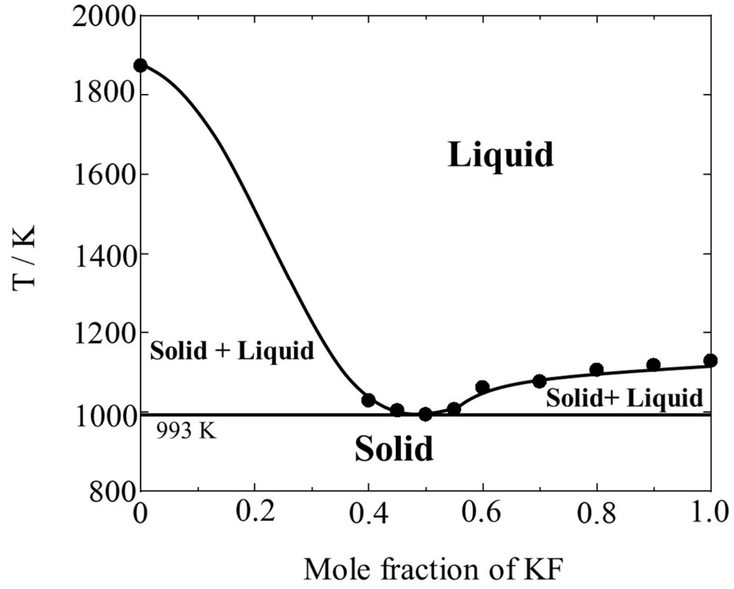

Figure 3-3. Phase diagram of the KF-SiO_2 system.

In order to examine the coordination structure of silicon ions in the eutectic composition of the KF-SiO_2 (50:50 mol%) system, high temperature Raman spectroscopy was conducted. Figure 3-4 shows the Raman spectrum of the melt from 800 to 1200 cm^{-1} at 1073 K. The spectrum contains several wide vibrational bands that can be assigned based on previously reported studies. The band with a maximum at 1100 cm^{-1} corresponds to $Si_2O_5^{2-}$ with one non-bridging oxygen atom. Smaller bands near 850, 920, and 960 cm^{-1} can be attributed to SiO_4^{4-}, $Si_2O_7^{6-}$, and SiO_3^{2-} with four, three, and two non-bridging oxygen atoms, respectively [20,21]. Also, the band with a maximum at 950 cm^{-1} is related to SiO_3F^{3-} [22]. From the Raman spectrum, it was revealed that SiO_2 dissolved as states of various silicate ions in the KF-SiO_2 system. Although it is difficult to quantitatively evaluate the amount of each silicate ion, the $Si_2O_5^{2-}$ ion was considered to be the dominant species because the intensity of the Raman band at 1100 cm^{-1} is considerably larger. These results indicate that fluoride anions may have caused Si-O-Si bond breakage of SiO_2, after which the oxyfluoride or silicate ions formed.

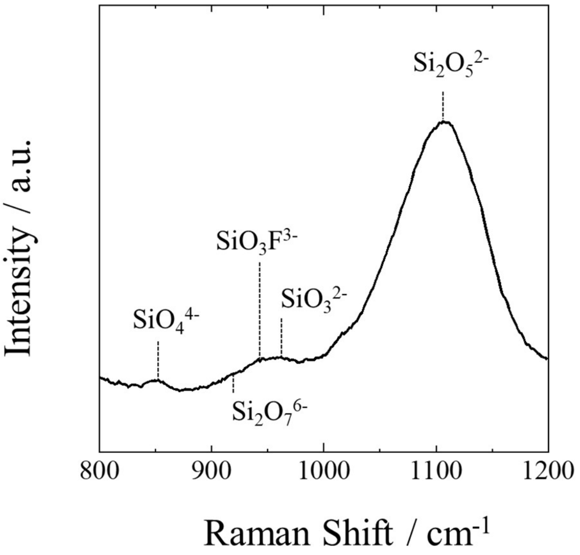

Figure 3-4. Raman spectrum of the KF-SiO_2 melt at 1073 K.

3.3.2. Coordination structure of silicon ions in molten LiF-KF-SiO_2 and molten LiF-NaF-KF-SiO_2 systems with and without Li_2O

The coordination structure of silicon ions was investigated in a molten LiF-KF (51.0:49.0 mol%) system containing 5.0 mol% SiO_2 and a molten LiF-NaF-KF (46.5:11.5:42.0 mol%) system containing 5.0 mol% SiO_2 with and without Li_2O. Compared to KF-SiO_2, LiF-KF and LiF-NaF-KF were more suitable electrolytes for Si electrodeposition because of their low melting points (LiF-KF: 765 K and LiF-NaF-KF: 730 K) and low viscosity.

Figure 3-5 shows the Raman spectra for molten (a) LiF-KF-SiO_2, (b) LiF-NaF-KF-SiO_2, (a′) LiF-KF, and (b′) LiF-NaF-KF at 873 K. Both LiF-KF-SiO_2 and LiF-NaF-

KF-SiO_2 showed several wide vibrational bands, while no bands or peaks were confirmed in the blank LiF-KF and LiF-NaF-KF. Moreover, the Raman spectra of both LiF-KF-SiO_2 and LiF-NaF-KF-SiO_2 systems were similar to those of the KF-SiO_2 system. This indicates that the dissolution behavior of SiO_2 is almost the same in molten fluorides because of the presence of fluoride anions.

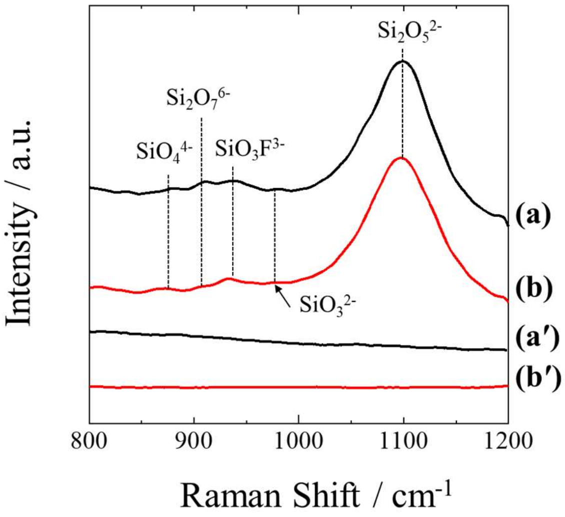

Figure 3-5. Raman spectra of molten (a) LiF-KF-SiO_2, (b) LiF-NaF-KF-SiO_2, (a′) LiF-KF, and (b′) LiF-NaF-KF at 873 K.

Figure 3-6 shows the Raman spectra for molten (a) LiF-KF-SiO_2 with 3.0 mol% Li_2O, (b) LiF-NaF-KF-SiO_2 with 3.0 mol% Li_2O, and (c) LiF-KF with 3.0 mol% Li_2O at 873 K. The Raman band near 1050 cm^{-1} was attributed to Li_2O. The Raman spectra of both types of SiO_2 (Fig. 3-6 (a) and (b)) were almost similar. Comparing the spectra with the Li_2O system (Figs. 3-6 (a) and (b)) to the system without Li_2O (Figs. 3-5 (a) and (b)), the intensity of the Raman band at 935 cm^{-1} due to the SiO_3F^{3-} ion increased after the addition of Li_2O. This indicates that the O^{2-} ions could cleave the Si-O-Si bonds of SiO_2 or silicate ions, such as $Si_2O_5^{2-}$; consequently, the formation of tetrahedron SiO_3F^{3-}

species was promoted.

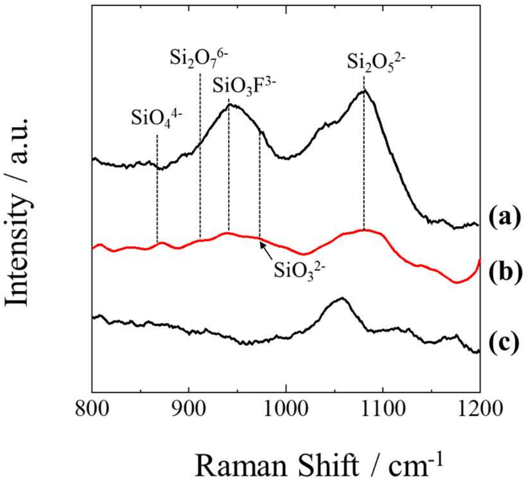

Figure 3-6. Raman spectra of molten (a) LiF-KF-SiO_2-Li_2O, (b) LiF-NaF-KF-SiO_2-Li_2O, and (c) LiF-KF-Li_2O at 873 K.

3.3.3. Electrodeposition of Si in a molten LiF-NaF-KF-SiO_2-Li_2O system

According to high temperature Raman spectroscopy, the addition of O^{2-} ions into the molten fluorides changed the bonding states of the silicon ions. In order to understand the effect of O^{2-} ions on the electrodeposition mechanism in the fluoride melt, Si was electrodeposited in molten LiF-NaF-KF with the Li_2O system. In a previous study, 1–2 µm thick dense polycrystalline Si films were electrodeposited on Ag substrates by potentiostatic electrolysis in molten LiF-NaF-KF, without Li_2O, at 873 K [17].

Figure 3-7 shows the cyclic voltammograms for Ag substrates before and after adding 5.0 mol% Li_2O into the LiF-NaF-KF at 873 K. Before adding Li_2O, a broad and slight cathodic current was observed up to approximately 1.0 V during the cathodic sweep, which was attributed to the reduction of silicon ions dissolved in the melt [17]. The broad cathodic curve represented the multiple coordination structures of the silicon ions, such as SiO_3^{2-}, $Si_2O_5^{2-}$, $Si_2O_7^{6-}$, SiO_4^{4-}, and SiO_3F^{3-}, which were confirmed by Raman spectroscopy. After adding Li_2O, the reduction current significantly increased. This suggested that the solubility of SiO_2 could be enhanced by the change in the coordination structure of silicon ions associated with the addition of O^{2-} ions.

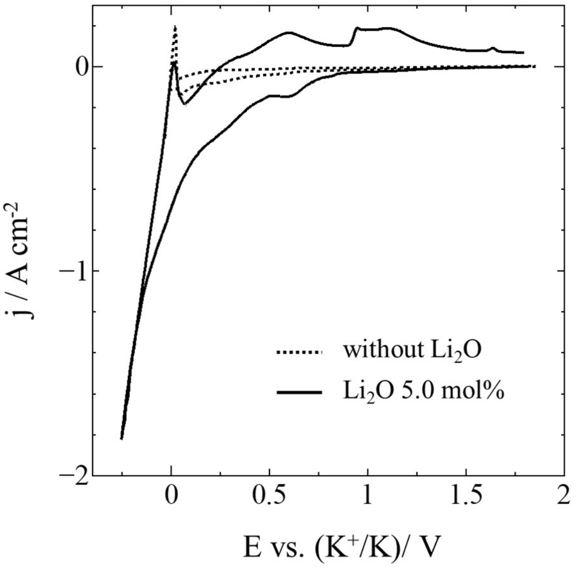

Figure 3-7. Cyclic voltammograms for an Ag electrode before and after adding Li_2O into molten LiF-NaF-KF-SiO_2 at 873 K. Scan rate: 0.1 V s^{-1}.

Based on the results of cyclic voltammetry, potentiostatic electrolysis was conducted where the potentials were considered to be negative enough to form metallic silicon, at 0.2, 0.3 and 0.4 V. Measurements were made for 3600 s using Ag plate cathodes in molten LiF-NaF-KF containing 0.5 mol% SiO_2 with or without 5.0 mol% Li_2O. Figure 3-8 shows cross-sectional SEM images of the samples in both electrolytes. Si layers with thicknesses of a few micrometers were obtained in the cases without Li_2O, whereas the thicknesses of Si layers increased from tens to hundreds of micrometers with Li_2O, especially at 0.2 and 0.3 V. As shown in Fig. 3-9, the electrodeposits of Si were identified using EDS analysis. In Fig. 3-9, the green and red areas correspond to Ag and Si, respectively. Figure 3-10 shows the results of the XRD patterns for the samples. The sample obtained at 0.4 V was partially deposited on the substrate and the majority of the deposits obtained at 0.4 V were exfoliated when rinsed with hot water. This indicated low adhesion between the electrodeposited Si and Ag substrate at that potential. The peaks attributed to polycrystalline Si were found in the samples with electrolytic potentials at 0.2 and 0.3 V, whereas only peaks that could be attributed to the Ag substrate were observed at 0.4 V. The K-Si alloy was also detected in the sample at 0.2 V.

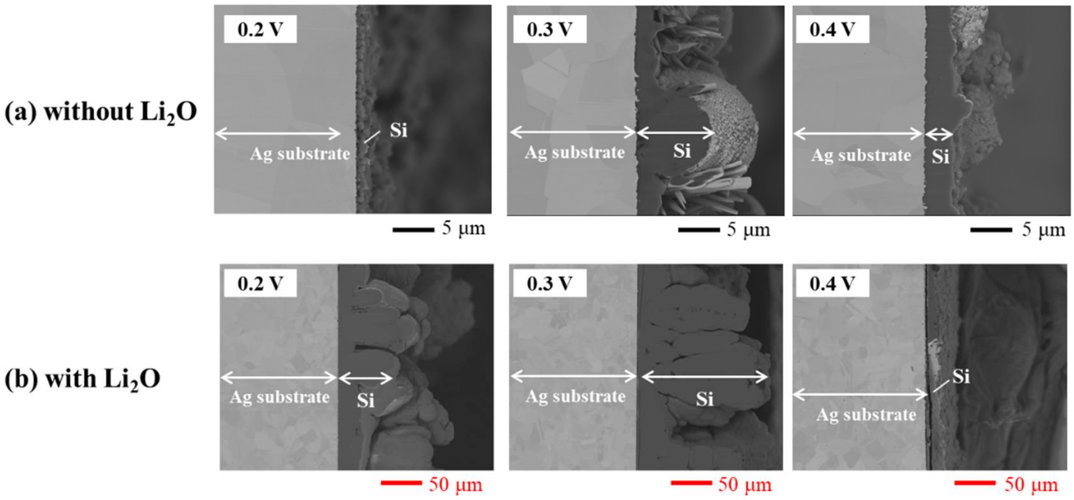

Figure 3-8. SEM images of samples after potentiostatic electrolysis at 0.2, 0.3, and 0.4 V for 3600 s in molten LiF-NaF-KF containing 0.5 mol% SiO_2 (a) without and (b) with 5.0 mol% Li_2O at 873 K.

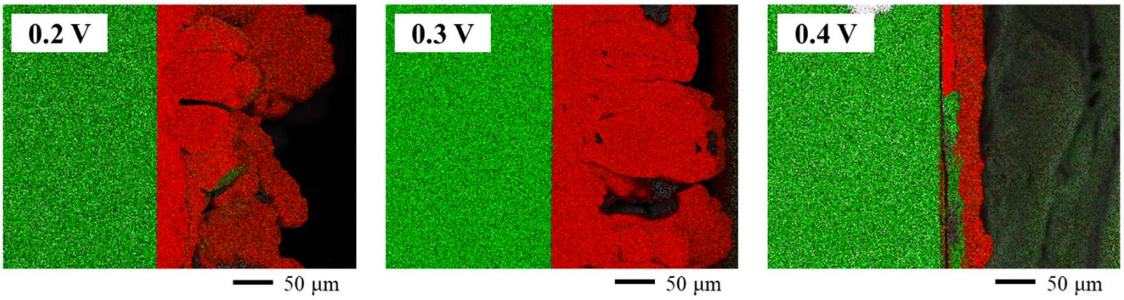

Figure 3-9. EDS element mapping images of the samples after potentiostatic electrolysis at 0.2, 0.3 and 0.4 V for 3600 s in molten LiF-NaF-KF containing SiO_2 with 5.0 mol% Li_2O at 873 K. The green and red areas in the images correspond to Ag and Si, respectively.

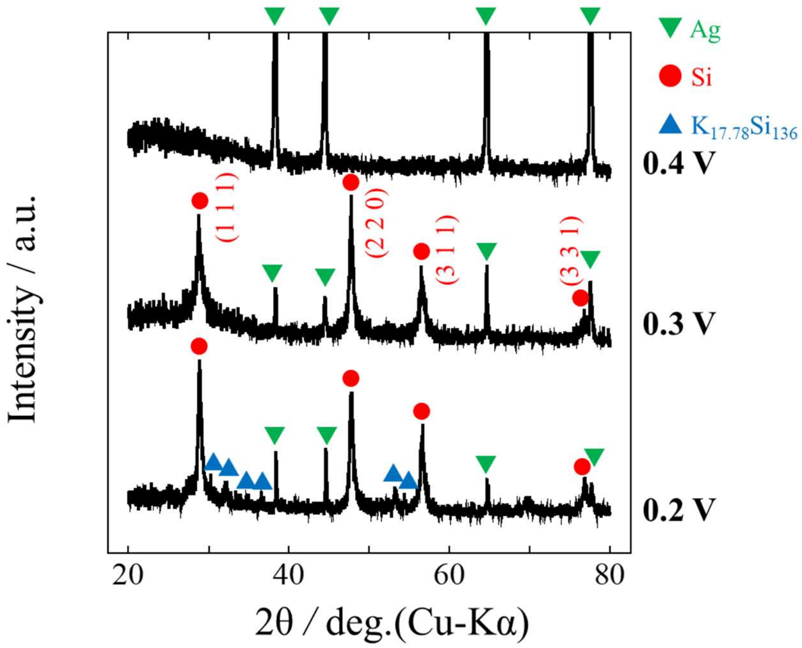

Figure 3-10. XRD patterns of the samples after potentiostatic electrolysis at 0.2, 0.3 and 0.4 V for 3600 s in molten LiF-NaF-KF-SiO_2 with 5.0 mol% Li_2O at 873 K.

In order to investigate the time transient of the morphological variations of the Si layer in LiF-NaF-KF with Li_2O at 873 K, the Si samples were prepared by potentiostatic electrolysis at 0.3 V, where the electrolytic potential forms good adhesion of electrodeposited Si without the formation of any K-Si alloys, for 60, 600, and 1800 s. Figure 3-11 shows the cross-sectional SEM images. Although a flat and dense Si layer was formed at the initial stage of the electrolysis (Fig. 3-11 (a)), the Si layer surface morphology partially changed to an inhomogeneous shape when the thickness reached approximately 10 μm (Fig. 3-11 (b)). With an increase in electrolysis time, the surface morphology became rougher (Fig. 3-11 (c)). This morphological change may have been caused by a comproportionation reaction between electrodeposited Si and silicon ions in the melt [3]:

$$\mathrm{Si} + \mathrm{Si(IV)} \rightarrow 2\mathrm{Si(II)}$$

Once the Si deposit became partially rough due to the above reaction, heterogeneous growth could be enhanced from this roughness at the starting point. Also, the reduction reaction of Si(II) ions could cause the morphological change because of the difference in reduction processes between Si(IV) and Si(II). Table 3-1 lists the thickness of Si layers and current efficiencies of the samples prepared by potentiostatic electrolysis at various potentials for 1 h in molten LiF-NaF-KF, with or without 5.0 mol% Li_2O, at 873 K. The thickness and current efficiencies were significantly enhanced by the addition of Li_2O, which indicated that the coordination structures of silicon ions affected characteristics of the electrodeposited Si, such as denseness, adhesion, and morphology. This indicated that the comproportional reaction could be suppressed by adding Li_2O because of the structural change in the silicon ions. These results suggested that the design of the molten salts bath is a key parameter for fabricating high-quality Si layers with high current efficiency.

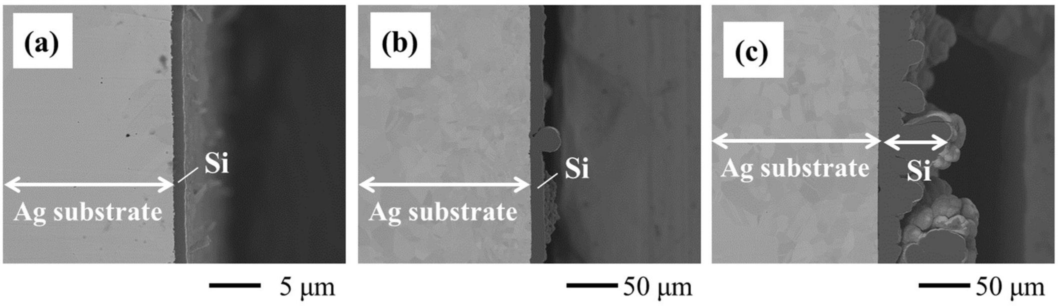

Figure 3-11. SEM images of the samples after potentiostatic electrolysis at 0.3 V for (a) 60 s, (b) 600 s, and (c) 1800 s in molten LiF-NaF-KF containing 0.5 mol% SiO_2 with 5.0 mol% Li_2O at 873 K.

Table 3-1. Thickness of Si layer and current efficiencies of samples prepared by potentiostatic electrolysis at various potentials in molten LiF-NaF-KF-SiO_2 with or without 5.0 mol% Li_2O at 873 K.

Potential / V	Thickness of Si layer / μm		Current efficiency / %	
	without Li_2O	with Li_2O	without Li_2O	with Li_2O
0.7	1	-	23.2	-
0.4	1–3	(island-like deposit)	19.0	6.5
0.3	2–6	40–160	13.3	50.8
0.2	0.2–1	30–100	13.2	49.9

The growth rate of the thickness of the Si layers could be enhanced by adding O^{2-} ions into the molten fluoride; however, the surface morphology of the Si layers must be more carefully controlled by electrochemical parameters. The molten fluoride system, which can fabricate Si films from SiO_2 at low temperatures, has potential for the development of environmentally friendly and sustainable electrolytic systems by combining non-consumable oxygen-evolving anodes, such as boron-doped diamond electrodes [23].

3.4. Conclusions

In Chapter 3, the effects of O^{2-} ions on the coordination structure of silicon ions and electrodeposition process of Si films in molten LiF-NaF-KF mixed with SiO_2 powder, both with and without an Li_2O system, at 873 K were investigated. The following results were obtained:

(1) The phase diagram of the KF-SiO_2 binary system was constructed via TG-DTA measurements. The eutectic composition was 50 mol% and the eutectic temperature was 993 K.

(2) High temperature Raman spectroscopic data revealed that SiO_2 was dissolved by forming Si-F and Si-O bands in molten LiF-NaF-KF and LiF-KF at 873 K and molten KF-SiO_2 at 1073 K.

(3) When Li_2O was added into molten LiF-KF and LiF-NaF-KF, the intensity of the Raman band due to the SiO_3F^{3-} structure increased. This indicated that the O^{2-} ions can cause breakage of the Si-O-Si bonds of SiO_2 or silicate ions, such as $Si_2O_5^{2-}$.

Electrochemical measurements showed that the cathodic current, attributed to the reduction of silicon ions, was significantly increased by adding Li_2O into molten LiF-NaF-KF. The thickness and the current efficiency of polycrystalline Si layers prepared by potentiostatic electrolysis, at 0.2, 0.3, and 0.4 V for 1 h, were improved by adding Li_2O.

These results indicated that O^{2-} ions play a key role in the electrodeposition process of Si in molten fluoride and that the design of the molten salts bath is important for obtaining high-quality Si layers with high current efficiency.

References

[1] U. Cohen, R. A. Huggins, “Silicon epitaxial growth by electrodeposition from molten fluorides”, J. Electrochem. Soc., **123**, 381 (1976).

[2] U. Cohen, “Some prospective applications of silicon electrodeposition from molten fluorides to solar cell fabrication”, J. Electron. Mater., **6**, 607 (1977).

[3] G. M. Rao, D. Elwell, R. S. Feigelson, “Electrodeposition of silicon onto graphite”, J. Electrochem. Soc., J. Electrochem. Soc., **128**, 1708 (1981).

[4] K. L. Carleton, J. M. Olson, A. Kibbler, “Electrochemical Nucleation and Growth of Silicon in Molten Fluorides”, J. Electrochem. Soc., **130**, 782 (1983).

[5] G. M. Rao, D. Elwell, R. S. Feigelson, “Electrowinning of silicon from fluoride systems”, J. Electrochem. Soc., **127**, 1940 (1980).

[6] D. Elwell, G. M. Rao, “Mechanism of electrodeposition of silicon from K_2SiF_6-flinak”, Electrochim. Acta, **27**, 673 (1982).

[7] L. Massot, A. L. Bieber, M. Gibilaro, L. Cassayre, P. Taxil, P. Chamelot, “Silicon recovery from silicon–iron alloys by electrorefining in molten fluorides”, Electrochim. Acta, **96** 97 (2013).

[8] T. Oishi, M. Watanabe, K. Koyama, M. Tanaka, K. Saegusa, “Process for solar grade silicon production by molten salt electrolysis using aluminum-silicon liquid alloy”, J. Electrochem. Soc., **158**, E93 (2011).

[9] T. Nohira, K. Yasuda, Y. Ito, “Pinpoint and bulk electrochemical reduction of insulating silicon dioxide to silicon”, Nat. Mater., **2**, 397 (2003).

[10] K. Yasuda, T. Nohira, Y.H. Ogata, Y. Ito, “Direct electrolytic reduction of solid silicon dioxide in molten LiCl–KCl–$CaCl_2$ at 773 K”, J. Electrochem. Soc., **152**, D208 (2005).

[11] X. Yang, K. Yasuda, T. Nohira, R. Hagiwara, T. Homma, "Kinetic Characteristics of Electrochemical Reduction of SiO_2 Granules in Molten $CaCl_2$", J. Electrochem. Soc., **161** D3116 (2014).

[12] S. K. Cho, F.-R. F. Fan, A. J. Bard, "Electrodeposition of crystalline and photoactive silicon directly from silicon dioxide nanoparticles in molten $CaCl_2$", Angew. Chem. Int. Ed., **51**, 12740 (2012).

[13] J. Zhao, H. Yin, T. Lim, H. Xie, H. Y. Hsu, F. Forouzan, A. J. Bard, "Electrodeposition of photoactive silicon films for low-cost solar cells" J. Electrochem. Soc., **163**, D506 (2016).

[14] X. Yang, L. Ji, X. Zou, T. Lim, J. Zhao, E. T. Yu, A. J. Bard, "Toward cost-effective manufacturing of silicon solar cells: electrodeposition of high-quality Si films in a $CaCl_2$-based molten salt", Angew. Chem. Int. Ed. **56**, 15078 (2017).

[15] X. Zou, L. J., X. Yang, T. Lim, E. T. Yu, A. J. Bard, "Electrochemical formation of a p–n junction on thin film silicon deposited in molten salt", J. Am. Chem. Soc., **139**, 16060 (2017).

[16] K. Yasuda, K. Maeda, R. Hagiwara, T. Homma, T. Nohira, "Silicon Electrodeposition in a Water-Soluble KF–KCl Molten Salt: Utilization of $SiCl_4$ as Si Source", J. Electrochem. Soc. **164**, D67 (2017).

[17] Y. Sakanaka, T. Goto, "Electrodeposition of Si film on Ag substrate in molten LiF–NaF–KF directly dissolving SiO_2", Electrochim. Acta, **164**, 139 (2015).

[18] A. Retsinas, A. G. Kalampounias, G. N. Papatheodorou, "Glass formation and Raman spectra of CaO–SiO_2 glasses towards the orthosilicate limit", J. Phys. Chem. Solids, **99**, 19 (2016).

[19] V. G. Konakov, M. Pivovarov, "Interaction between Components in the KF–SiO_2

System", Glass Phys. Chem., **29**, 69 (2003).

[20] B. O. Mysen, D. Virgo, C. M. Scare, "Relations between the anionic structure and viscosity of silicate melts—a Raman spectroscopic study", Am. Mineral., **65** 690 (1980).

[21] D. Virgo, B. O. Mysen, T. Kushiro, "Anionic constitution of 1-atmosphere silicate melts: implications for the structure of igneous melts", Science, **208**, 1371 (1980).

[22] Y. P. Zaykov, A. V. Isakov, I. D. Zakiryanova, O. G. Reznitskikh, O. V. Chemezov, A. A. Redkin, "Interaction between SiO_2 and a KF–KCl–K_2SiF_6 Melt", J. Phys. Chem. B, **118**, 1584 (2014).

[23] T. Goto, Y. Arakia, R. Hagiwara, "Oxygen gas evolution on the boron-doped diamond electrode in molten chloride system", Electrochem. Solid-State Lett., **9**, D5 (2006).

CHAPTER 4

Raman Spectroscopy for Determination of Silicon Oxyfluoride Structure in Fluoride Melts

4.1. Introduction

Silicon electrodeposition in molten salts has been attractive as an alternative process for manufacturing crystalline-silicon films for solar cells. Many kinds of molten salts, for instance, the fluoride system (LiF-NaF-KF [1,2], LiF-KF [3–6] and NaF-KF [7] melts), chloride system ($CaCl_2$ [8–12] and $CaCl_2$-CaO [13,14] melts), and fluoride-chloride system (KF-KCl [15] melt), have been used for Si electrodeposition. In regards to a Si source, several Si compounds, such as K_2SiF_6 [1–6], $SiCl_4$ [15], and SiO_2 [8–14], have been used as starting materials. Considering ISRU from the moon, SiO_2 is a prominent candidate resource for Si extraction. To fabricate silicon films by a simple and inexpensive process, studies using SiO_2, which is the main constituent of lunar and Martian regolith, as the Si source have recently received attention [8–14].

Fluoride melts have several advantages, especially their ability to obtain crystalline Si directly from SiO_2 at lower temperatures because of the high solubility of oxides. In fact, it has been reported that crystalline Si films were obtained by electrolysis in molten LiF-NaF-KF by adding SiO_2 powder at 873 K [16,17]. The operating temperature, the solubility process of SiO_2, and the electrochemical behavior of silicon ions are dependent on the composition of the fluoride melt. Therefore, understanding the interactions between the silicon ions formed by dissolving SiO_2 and constituent ions of the fluoride melt is beneficial to control the solubility process of SiO_2 and the silicon electrodeposition process. However, only a few studies [18,19] have been reported on the coordination structure of silicon ions.

Raman spectroscopy is a suitable method for investigating coordination structures of metal ions in molten salts [20,21]. For example, several structures of silicon ions in slug systems, such as $Si_2O_5^{2-}$, were proposed by means of this technique [22,23]. Recently, it has been reported that oxide anions could cause breakage of the Si-O-Si bonds of SiO_2, resulting in enhanced solubility of SiO_2 in LiF-NaF-KF melt [17]. Therefore, the dissolution process of SiO_2 in molten salt is a crucial factor for tailoring Si films and it is also necessary to clarify the stable structure of silicon ions in terms of the physicochemical phenomena of high temperature molten salt. However, few studies have been done in fluoride melts dissolving SiO_2 and several questions still remain. These questions include what silicate species exist in the fluoride melts and how can cations, such as Li^+, Na^+ and K^+, affect the coordination structure of silicon ions in the melts.

In this chapter the coordination structures of silicon ions in eutectic LiF-KF, LiF-NaF, and NaF-KF melts with SiO_2, with and without Li_2O, systems are reported. To specify the stable structure of silicon ions in each molten salt, Raman spectroscopy was combined with DFT calculations.

4.2. Experimental

LiF (98.0%, FUJIFILM Wako Pure Chemical Corporation), NaF (99.0%, FUJIFILM Wako Pure Chemical Corporation), KF (99.0%, FUJIFILM Wako Pure Chemical Corporation), SiO_2 (99.0%, FUJIFILM Wako Pure Chemical Corporation), and

Li_2O (99.0%, FUJIFILM Wako Pure Chemical Corporation) were used as the electrolyte materials. The reagents were then mixed in eutectic compositions (LiF-KF = 51.0:49.0 mol%, LiF-NaF = 61.0:39.0 mol%, and NaF-KF = 39.7:60.3 mol%). The mixtures were kept under vacuum for more than 48 h at 473 K to eliminate any water. The melting points of the mixtures were 765 K for the LiF-KF melt, 925 K for the LiF-NaF melt, and 983 K for the NaF-KF melt [24]. The Raman spectra of each sample in molten state were obtained at different temperatures.

For DFT calculations, the Gaussian 09 (Revision B. 01) package [25] was used. Geometry optimization and vibrational frequency calculations of Raman spectra for models of the silicon oxyfluoride monomers were done using DFT with the B3LYP/6-311+G(d) hybrid exchange-correlation functional/basis set framework.

For Raman spectroscopic analysis, eutectic LiF-NaF, LiF-KF, and NaF-KF salts with SiO_2 and with and without Li_2O mixtures were introduced into a platinum crucible. The crucible was sealed in a hot stage device (10016, Japan HighTech Co., Ltd.) and continuously heated at 100 K min^{-1} under an Ar atmosphere. Raman spectra were obtained using a micro-Raman spectrometer (LabRAM HR Evolution, Horiba Jobin-Yvon GmbH) with a YAG laser (532 nm).

4.3. Results and discussion

4.3.1. DFT calculations

In Chapter 3, the coordination structure of silicon ions that composed Si-O-Si bands, such as $Si_2O_5^{2-}$, were confirmed in a molten LiF-NaF-KF melt with SiO_2 by means of Raman spectroscopy. However, information about the interaction between silicon ions and fluoride ions has been limited because few studies have focused on the structure of silicon oxyfluoride in molten fluoride-oxide systems. On the other hand, oxyhalide structures, such as oxychloride glasses, were proposed by Raman spectroscopy in the molten chloride-oxide system [26]. Although few reports have mentioned the existence of silicon oxyfluoride, such as SiO_3F^{3-}, in solid vitreous silica [27], more work is needed for identifying other silicon oxyfluoride species and for elucidating their interaction with silicon ions in the molten fluoride-oxide system. In Chapter 4, several silicon oxyfluorides have been assumed and DFT calculations were carried out to optimize their geometric structures and determine their vibrational modes. Figure 4-1 shows all calculated silicon oxyfluorides. The number assigned to each atom in Fig. 4-1 is the Mulliken charge distribution.

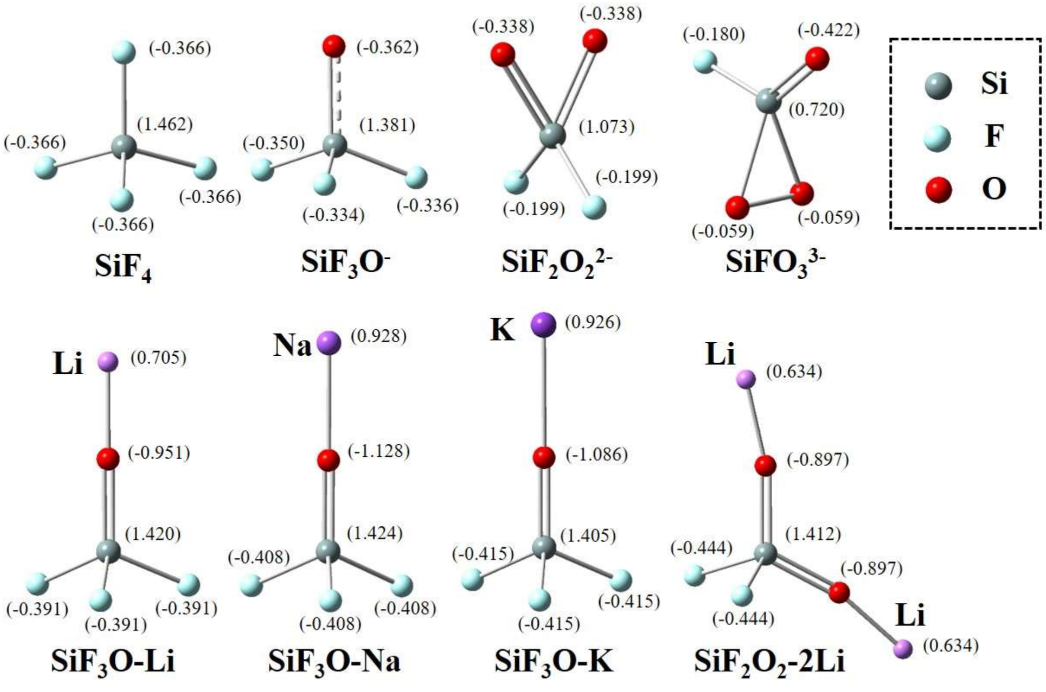

Figure 4-1. Optimized structures of silicon oxyfluoride monomers by DFT calculations. The number assigned to each atom is the Mulliken charge distribution.

As can be seen in Fig. 4-1, two types of silicon oxyfluorides are assumed. One type has a polyatomic ion-like structure, such as SiF_3O^-, $SiF_2O_2^{2-}$, and $SiFO_3^{3-}$, which are composed of Si, O, and F elements. The other is a molecule-like structure, such as SiF_3O-Li, SiF_3O-Na, SiF_3O-K, and SiF_2O_2-2Li, which are composed of anions with ion-like structure and cations of Li, Na, and K. Figure 4-2 represents the simulated Raman spectra with vibrational modes calculated for these species. It can be observed from Fig. 4-2 that most of the Raman shifts range from 400 to 1200 cm^{-1}. The calculated wavenumbers for the vibrational modes of the simulated species are summarized in Table 4-1.Geometric configurations for each vibrational mode are shown in Fig. S4-1 for the ion-like structures and in Fig. S4-2 for the molecule-like structures, in the Supplementary data. The calculated results were compared with experimental data measured by Raman spectroscopy.

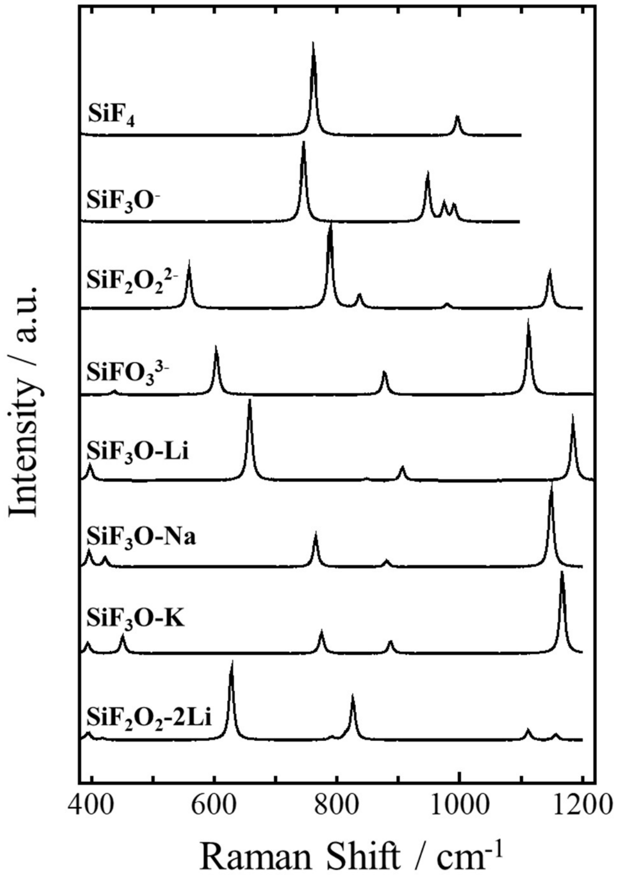

Figure 4-2. Simulated Raman spectra with vibrational modes calculated for the silicon oxyfluoride monomers illustrated in Fig. 4-1.

Table 4-1. Calculated Raman shift wavenumbers for the major vibrational modes of species simulated in this chapter.

Species	Raman shift wavenumber / cm^{-1}
SiF_4	761, 996
SiF_3O^-	746, 948, 975, 991
$SiF_2O_2^{2-}$	559, 789, 837, 980, 1146
$SiFO_3^{3-}$	437, 604, 878, 1113
SiF_3O-Li	658, 848, 906, 1185
$SiFO_3O$-Na	451, 775, 887, 1167
SiF_3O-K	422, 765, 881, 1149
SiF_2O_2-2Li	418, 628, 791, 814, 826, 1112, 1156

4.3.2. Experimental Raman spectra for LiF-KF, LiF-NaF and NaF-KF melts with SiO_2

It is well known from the literature [22,23] that silicon anions composed of Si and O elements, such as $Si_2O_5^{2-}$, have been identified in slug systems. With respect to the molten fluoride system, few studies have obtained experimental data with information on silicon oxyfluoride in the melt. In this chapter, high temperature fluoride melts were analyzed by Raman spectroscopy to identify the silicon oxyfluoride species in the fluoride melt. It can be predicted from the DFT results (Fig. 4-2) that the vibrational modes of oxyfluorides should appear between 400 and 1200 cm^{-1}.

Experimental Raman spectra was obtained for LiF-KF (873 and 973 K), LiF-NaF (973, 1023, and 1073 K), and NaF-KF (1023 and 1073 K) melts with 5.0 mol% SiO_2 between 400 and 1200 cm^{-1}, as shown in Figs. 4-3 through 4-5. These three types of binary fluoride melts were selected to compare the effect of cation (Li^+, Na^+, and K^+)

difference on the coordination structure of the silicon ions. IGOR Pro software (version 6.3.4.0, WaveMetrics, Lake Oswego, OR, USA) was used for data analysis. Each of the observed Raman bands were fit to a Gaussian function. The figures depict the raw data (black bold line), fitting curve (red line), base line (dotted line), residual curve (blue line), and separated bands (black lines). The coordination structures of the silicon ions were determined by comparing the separated bands and the calculated spectra (Fig. 4-2), as summarized in Tables 4-2–4-4.

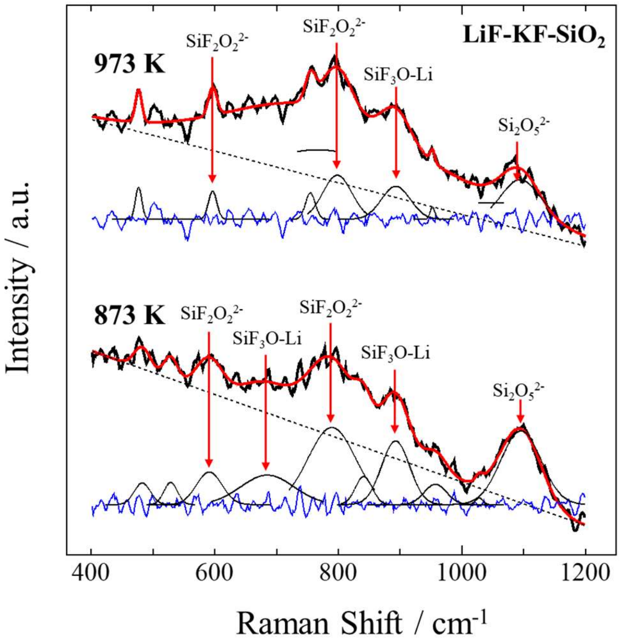

Figure 4-3. Raman spectra of LiF-KF melt with 5.0 mol% SiO$_2$. Raw data (black bold line), fitting curve (red line), base line (dotted line), residual curve (blue line), and separated bands (black lines).

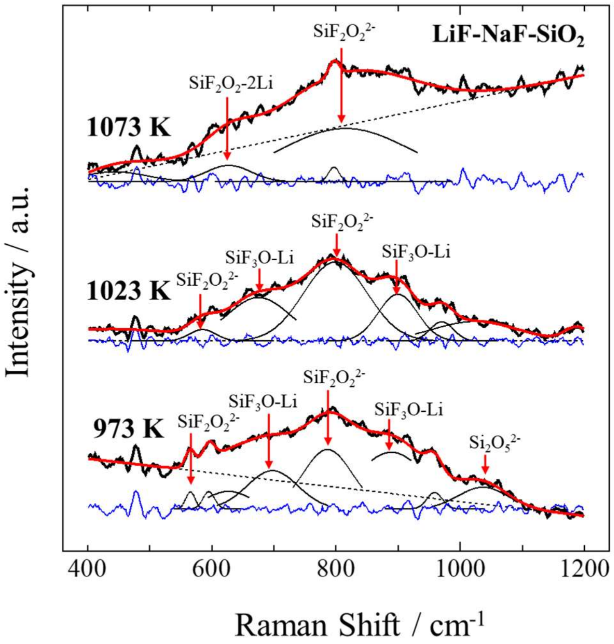

Figure 4-4. Raman spectra of LiF-NaF melt with 5.0 mol% SiO_2. Raw data (black bold line), fitting curve (red line), base line (dotted line), residual curve (blue line), and separated bands (black lines).

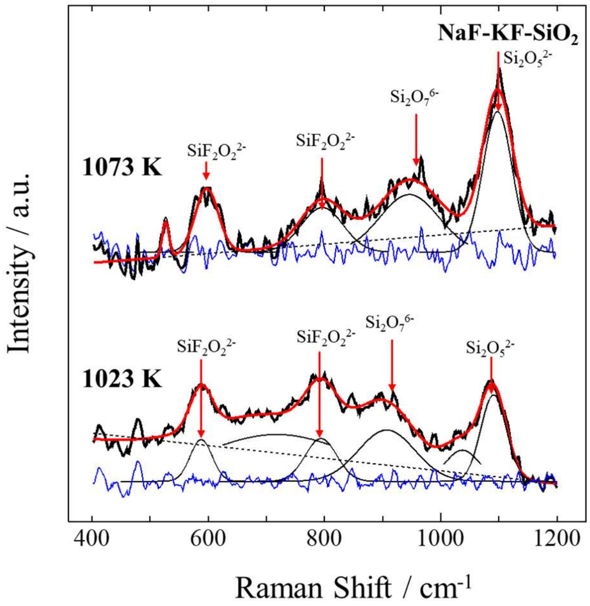

Figure 4-5. Raman spectra of NaF-KF melt with 5.0 mol% SiO_2. Raw data (black bold line), fitting curve (red line), base line (dotted line), residual curve (blue line), and separated bands (black lines).

Table 4-2. Summary of experimental Raman spectra of LiF-KF-SiO_2 melt.

Experimental temperature / K	Fitting value for Raman band / cm^{-1}	Species	Assignment
973	597	$SiF_2O_2^{2-}$	this work
	798	$SiF_2O_2^{2-}$	
	893	$SiFO_3$-Li	
	1094	$Si_2O_5^{2-}$	ref [22,23]
873	591	$SiF_2O_2^{2-}$	this work
	685	SiF_3O-Li	
	790	$SiF_2O_2^{2-}$	
	892	SiF_3O-Li	
	1096	$Si_2O_5^{2-}$	ref [22,23]

Table 4-3. Summary of experimental Raman spectra of LiF-NaF-SiO_2 melt.

Experimental temperature / K	Fitting value for Raman band / cm^{-1}	Species	Assignment
1073	627	SiF_2O_2-2Li	this work
	797	$SiF_2O_2^{2-}$	
1023	585	$SiF_2O_2^{2-}$	this work
	675	SiF_3O-Li	
	799	$SiF_2O_2^{2-}$	
	899	SiF_3O-Li	
973	562	$SiF_2O_2^{2-}$	this work
	698	SiF_3O-Li	
	786	$SiF_2O_2^{2-}$	
	889	SiF_3O-Li	
	1036	$Si_2O_5^{2-}$	ref [22,23]

Table 4-4. Summary of experimental Raman spectra of NaF-KF-SiO_2 melt.

Experimental temperature / K	Fitting value for Raman band / cm^{-1}	Species	Assignment
1073	597	$SiF_2O_2^{2-}$	this work
	796	$SiF_2O_2^{2-}$	
	946	$Si_2O_7^{6-}$	ref [22]
	1097	$Si_2O_5^{2-}$	ref [22,23]
1023	588	$SiF_2O_2^{2-}$	this work
	794	$SiF_2O_2^{2-}$	
	907	$Si_2O_7^{6-}$	ref [22]
	1091	$Si_2O_5^{2-}$	ref [22,23]

In the majority of cases (Figs. 4-3–4-5), Raman bands centered between 1050 and 1100 cm^{-1} were observed and were attributed to a vibrational mode of $Si_2O_5^{2-}$ [22,23]. This result demonstrated that SiO_2 was dissolved in fluoride melts, which is consistent with results obtained in Chapter 3 and a previous study [16]. Also, bands with a large half width in the range of 900–950 cm^{-1}, which were attributed to the vibrational mode of $Si_2O_7^{6-}$ [22], were observed. In addition, Raman bands centered around 580 and 790 cm^{-1} were also observed in most cases. These bands were attributed to the vibrational modes of $SiF_2O_2^{2-}$ by comparing experimental data with calculated Raman spectra (Fig. 4-2). This indicated that SiO_2 was dissolved in the fluoride melts and then some of the silicon ions formed $SiF_2O_2^{2-}$ anions as a stable structure, with interaction between Si, F, and O ions.

The noticeable differences in the results of Raman spectra among LiF-KF, LiF-

NaF, and NaF-KF melts were that the Raman bands near 660 and 900 cm^{-1}, attributed to the vibrational mode of SiF_3O-Li, were observed in LiF-KF and LiF-NaF melts (Figs. 4-3 and 4-4). However, the bands attributed to SiF_3O-Na and SiF_3O-K could not be observed in any melts. In the case of the LiF-NaF melt at 1073 K, the band at 627 cm^{-1} for SiF_2O_2-2Li was also observed. These results indicated that Li^+ could more easily interact with silicon ions, rather than K^+ and Na^+, and silicon ions in the melt could form the molecule-like structure by interacting with Li^+.

4.3.3. Experimental Raman spectra for LiF-KF, LiF-NaF and NaF-KF melts with SiO_2 and Li_2O

It was suggested in the literature [13,14] that solubility of SiO_2 was enhanced by dissolving alkaline Earth oxides in molten salt. Thus, O^{2-} ions formed in the melt by dissolving such an oxide was considered to be a key species for the dissolving behavior of SiO_2. In fact, it has been described in Chapter 3 that O^{2-} ions have potential to change the coordination structure of silicon ions in the LiF-NaF-KF melt with the addition of SiO_2 to the system. This phenomenon plays a crucial role in the electrodeposition process of Si because the difference in coordination structure has an impact on the characteristics of the electrodeposited Si and current efficiency. However, the interaction between silicon oxyfluoride and O^{2-} ions in the fluoride melt remains unclear. In this chapter, the effect of O^{2-} ions was investigated in LiF-KF, LiF-NaF, and NaF-KF melts with SiO_2 by adding Li_2O as a source of O^{2-} ions.

Figures 4-6 through 4-8 show the Raman spectra between 400 and 1200 cm^{-1} for LiF-KF (873 and 973 K), LiF-NaF (973, 1023, and 1073 K) and NaF-KF (1023 and 1073 K) melts with 5.0 mol% SiO_2 and 5.0 mol% Li_2O. The coordination structures of silicon ions were determined by comparing the separated bands and the calculated spectra (Fig. 4-2), as summarized in Tables 4-5–4-7. As shown in the spectra for the LiF-KF system (Fig. 4-6), two remarkable Raman bands around 600 and 970 cm^{-1} were observed. These bands were attributed to the vibrational modes of $SiFO_3^{3-}$ and SiF_3O^-, respectively. This result was obviously different from the spectrum for the LiF-KF melt without Li_2O (Fig. 4-3), which indicated that O^{2-} ions promoted the formation of an ion-like structure. Similar behavior was observed in the LiF-NaF and NaF-KF systems, as can be seen in Figs. 4-7 and 4-8. In addition, the intensity of the Raman band between 1050 and 1100 cm^{-1} for $Si_2O_5^{2-}$ was smaller than the systems without Li_2O. This behavior was consistent with our previous results obtained in the LiF-NaF-KF melt [17], which confirmed that O^{2-} ions could cause breakage of Si-O-Si bonds of $Si_2O_5^{2-}$ or SiO_2, resulting in the formation of silicon oxyfluorides in the melt.

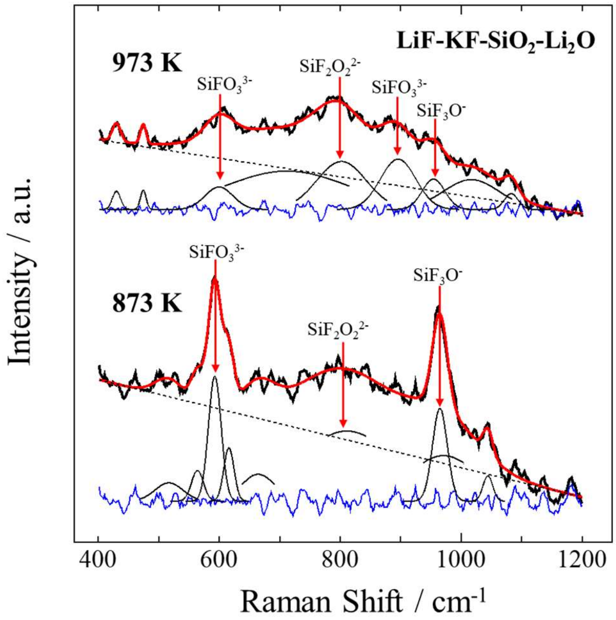

Figure 4-6. Raman spectra of the LiF-KF melt with 5.0 mol% SiO_2 and 5.0 mol% Li_2O. Raw data (black bold line), fitting curve (red line), base line (dotted line), residual curve (blue line), and separated bands (black lines).

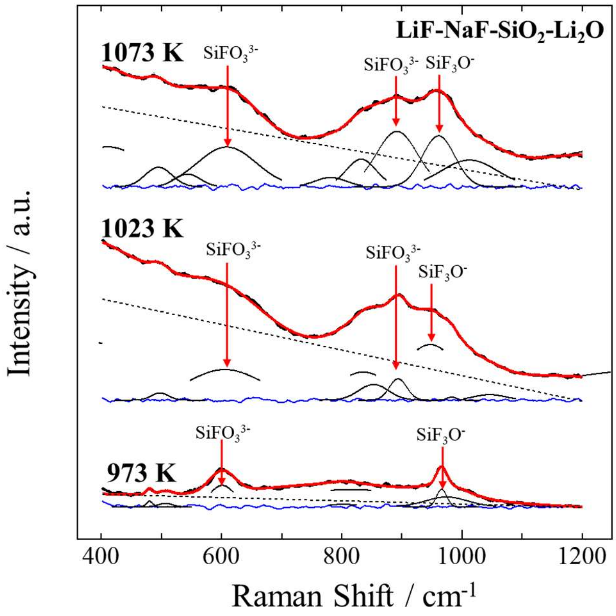

Figure 4-7. Raman spectra of the LiF-NaF melt with 5.0 mol% SiO_2 and 5.0 mol% Li_2O. Raw data (black bold line), fitting curve (red line), base line (dotted line), residual curve (blue line), and separated bands (black lines).

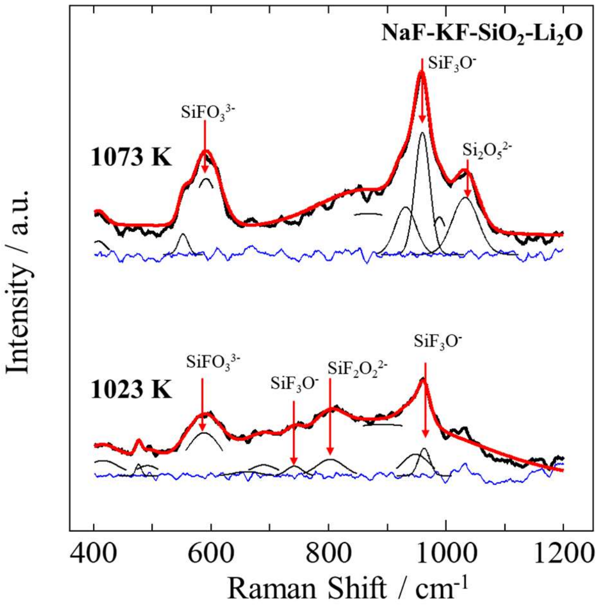

Figure 4-8. Raman spectra of the NaF-KF melt with 5.0 mol% SiO_2 and 5.0 mol% Li_2O. Raw data (black bold line), fitting curve (red line), base line (dotted line), residual curve (blue line), and separated bands (black lines).

Table 4-5. Summary of experimental Raman spectra of the LiF-KF-SiO_2-Li_2O melt.

Experimental temperature / K	Fitting value for Raman band / cm^{-1}	Species	Assignment
973	600	$SiFO_3^{3-}$	this work
	802	$SiF_2O_2^{2-}$	
	896	$SiFO_3^{3-}$	
	954	SiF_3O^-	
873	593	$SiFO_3^{3-}$	this work
	811	$SiF_2O_2^{2-}$	
	965	SiF_3O^-	

Table 4-6. Summary of experimental Raman spectra of the LiF-NaF-SiO_2-Li_2O melt.

Experimental temperature / K	Fitting value for Raman band / cm^{-1}	Species	Assignment
1073	609	$SiFO_3^{3-}$	this work
	892	$SiFO_3^{3-}$	
	961	SiF_3O^-	
1023	606	$SiFO_3^{3-}$	this work
	893	$SiFO_3^{3-}$	
	947	SiF_3O^-	
973	601	$SiFO_3^{3-}$	this work
	966	SiF_3O^-	

Table 4-7. Summary of experimental Raman spectra of the NaF-KF-SiO_2-Li_2O melt.

Experimental temperature / K	Fitting value for Raman band / cm^{-1}	Species	Assignment
1073	592	$SiFO_3^{3-}$	this work
	960	SiF_3O^-	
	1033	$Si_2O_5^{2-}$	ref [22,23]
1023	588	$SiFO_3^{3-}$	this work
	742	SiF_3O^-	
	803	$SiF_2O_2^{2-}$	
	963	SiF_3O^-	

The presence of ion-like and molecule-like structures of silicon ions in fluoride melts is a novel finding. This result expands prior work [17]; the reason why the reduction current of silicon ions increased when adding Li_2O to the LiF-KF-NaF melt at 873 K is related to an increasing amount of the ion-like structure in the melt. Furthermore, these findings could be applicable to other molten salt systems, such as chloride melt mixed with alkaline Earth oxide [13,14], promoting the dissolving process of SiO_2 and the electrodeposition process of Si.

Our study provides a framework for the relationship between the coordination structure of silicon ions and the composition of fluoride melts in terms of thermal equilibrium. However, the kinetic mechanisms of the structural change during the Si electrodeposition process remains to be determined. In the future, this technique should therefore be integrated with the electrochemical measurement of Si deposition in high temperature molten salt.

4.4. Conclusions

In Chapter 4, the interaction between silicon ions and several ions that compose fluoride melts in eutectic LiF-KF, LiF-NaF, and NaF-KF melts with SiO_2 and with and without Li_2O were investigated by combining DFT calculations with Raman spectroscopy. The results are summarized as follows:

(1) Two kinds of coordination structures of silicon ions were identified; one was an ion-like structure, such as $SiF_2O_2^{2-}$ and $Si_2O_5^{2-}$, and the other was a molecule-like structure, such as SiF_3O-Li and SiF_2O_2-2Li.

(2) The experimental Raman spectra for LiF-KF, LiF-NaF, and NaF-KF systems show that the Raman band attributed to SiF_3O-Li is observed in LiF-KF and LiF-NaF

systems. The band attributed to SiF_3O-Na and SiF_3O-K was not observed in any melts. This result indicated that Li^+ more easily interacts with silicon ions rather than K^+ and Na^+.

(3) When Li_2O was added into each of the fluoride melts, the Raman bands of $SiFO_3^{3-}$ and SiF_3O^- were observed. This indicated that O^{2-} ions have potential to promote the formation of oxyfluoride monomers by cleaving the Si-O-Si bands of $Si_2O_5^{2-}$ ions or SiO_2.

The knowledge obtained in this chapter provides the framework for understanding the relationship between the coordination structure of silicon ions and the composition of the fluoride melt. These findings are important for the electrodeposition process of silicon films in fluoride melt in terms of design of the electrolyte.

References

[1] G. M. Rao, D. Elwell, R. S. Feigelson, “Electrowinning of silicon from fluoride systems”, J. Electrochem. Soc., **127**, 1940 (1980).

[2] D. Elwell, G. M. Rao, “Mechanism of electrodeposition of silicon from K_2SiF_6-flinak”, Electrochim. Acta, **27**, 673 (1982).

[3] U. Cohen, R. A. Huggins, “Silicon epitaxial growth by electrodeposition from molten fluorides”, J. Electrochem. Soc., **123**, 381 (1976).

[4] U. Cohen, “Some prospective applications of silicon electrodeposition from molten fluorides to solar cell fabrication”, J. Electron. Mater., **6**, 607 (1977).

[5] G. M. Rao, D. Elwell, R. S. Feigelson, “Electrodeposition of silicon onto graphite, J. Electrochem. Soc.”, **128**, 1708 (1981).

[6] K. L. Carleton, J. M. Olson, A. Kibbler, “Electrochemical nucleation and growth of silicon in molten fluorides”, J. Electrochem. Soc., **130**, 782 (1983).

[7] L. Massot, A. L. Bieber, M. Gibilaro, L. Cassayre, P. Taxil, P. Chamelot, “Silicon recovery from silicon–iron alloys by electrorefining in molten fluorides”, Electrochim. Acta, 96 97 (2013).

[8] T. Nohira, K. Yasuda, Y. Ito, “Pinpoint and bulk electrochemical reduction of insulating silicon dioxide to silicon”, Nat. Mater., **2**, 397 (2003).

[9] K. Yasuda, T. Nohira, Y. H. Ogata, Y. Ito, “Direct electrolytic reduction of solid silicon dioxide in molten LiCl-KCl-$CaCl_2$ at 773 K”, J. Electrochem. Soc., **152**, D208 (2005).

[10] Y. Ma, A. Ido, K. Yasuda, R. Hagiwara, T. Homma, T. Nohira, “Mechanism of electrolytic reduction of SiO_2 at liquid Zn cathode in molten $CaCl_2$”, J. Electrochem. Soc., **166**, D162 (2019).

[11] S. K. Cho, F. R. F. Fan, A. J. Bard, “Electrodeposition of crystalline and photoactive

silicon directly from silicon dioxide nanoparticles in molten $CaCl_2$", Angew. Chem. Int. Ed., **51**, 12740 (2012).

[12] J. Zhao, H. Yin, T. Lim, H. Xie, H. Y. Hsu, F. Forouzan, A. J. Bard, "Electrodeposition of photoactive silicon films for low-cost solar cells", J. Electrochem. Soc., **163**, D506 (2016).

[13] X. Yang, L. Ji, X. Zou, T. Lim, J. Zhao, E. T. Yu, A. J. Bard, "Toward cost-effective manufacturing of silicon solar cells: electrodeposition of high-quality Si films in a $CaCl_2$-based molten salt", Angew. Chem. Int. Ed., **56**, 15078 (2017).

[14] X. Zou, L. J., X. Yang, T. Lim, E. T. Yu, A. J. Bard, "Electrochemical formation of a p–n junction on thin film silicon deposited in molten salt", J. Am. Chem. Soc., **139**, 16060 (2017).

[15] K. Yasuda, K. Saeki, T. Kato, R. Hagiwara, T. Nohira, "Silicon Electrodeposition in a water-soluble KF–KCl molten salt: effects of temperature and current density", J. Electrochem. Soc., **165**, D825 (2018).

[16] Y. Sakanaka, T. Goto, "Electrodeposition of Si film on Ag substrate in molten LiF–NaF–KF directly dissolving SiO_2", Electrochim. Acta, **164**, 139 (2015).

[17] Y. Suzuki, Y. Inoue, M. Yokota, T. Goto, "Effects of oxide ions on the electrodeposition process of silicon in molten fluorides", J. Electrochem. Soc., **166**, D564 (2019).

[18] Y. P. Zaikov, A. A. Redkin, A. A. Apisarov, I. V. Korzun, N. P. Kulik, A. V. Isakov, A. A. Kataev, O. V. Chemezov, "Silica Solubility in Molten Fluoride−Chloride Electrolytes and Density of $KF-KCl-K_2SiF_6-SiO_2$ Melts", J. Chem. Eng. Data, **58**, 932 (2013).

[19] Y. P. Zaykov, A. V. Isakov, I. D. Zakiryanova, O. G. Reznitskikh, O. V. Chemezov,

A. A. Redkin, “Interaction between SiO_2 and a KF−KCl−K_2SiF_6 Melt”, J. Phys. Chem. B, **118**, 1584 (2014).

[20] A. Retsinas, A. G. Kalampounias, G. N. Papatheodorou, “Glass formation and Raman spectra of CaO–SiO_2 glasses towards the orthosilicate limit”, J. Phys. Chem. Solids, **99**, 19 (2016).

[21] A. Rakhmatullin, M. Allix, I. B. Polovov, D. Maltsev, A. V. Chukin, R. Bakirov, C. Bessada, “Combining solid state NMR, powder X-ray diffraction, and DFT calculations for $CsSc_3F_{10}$ structure determination”, J. Alloys Comp., **787**, 1349 (2019).

[22] B. O. Mysen, D. Virgo, C. M. Scare, “Relations between the anionic structure and viscosity of silicate melts—a Raman spectroscopic study”, Am. Mineral., **65**, 690 (1980).

[23] D. Virgo, B. O. Mysen, T. Kushiro, “Anionic constitution of 1-atmosphere silicate melts: implications for the structure of igneous melts”, Science **208**, 1371 (1980).

[24] E. M. Levin, C. R. Robbins, H. F. McMurdie, Phase Diagrams for Ceramists, fifth ed., vol. 1, The American Ceramic Society, 1985.

[25] M. J. Frisch, G. W. Trucks, H. B. Schlegel, G. E. Scuseria, M. A. Robb, J. R. Cheeseman, G. Scalmani, V. Barone, B. Mennucci, G. A. Petersson, H. Nakatsuji, M. Caricato, X. Li, H. P. Hratchian, A. F. Izmaylov, J. Bloino, G. Zheng, J. L. Sonnenberg, M. Hada, M. Ehara, K. Toyota, R. Fukuda, J. Hasegawa, M. Ishida, T. Nakajima, Y. Honda, O. Kitao, H. Nakai, T. Vreven, J. A. Montgomery, Jr., J. E. Peralta, F. Ogliaro, M. Bearpark, J. J. Heyd, E. Brothers, K. N. Kudin, V. N. Staroverov, T. Keith, R. Kobayashi, J. Normand, K. Raghavachari, A. Rendell, J. C. Burant, S. S. Iyengar, J. Tomasi, M. Cossi, N. Rega, J. M. Millam, M. Klene, J. E. Knox, J. B. Cross, V. Bakken, C. Adamo, J. Jaramillo, R. Gomperts, R. E. Stratmann, O. Yazyev, A. J. Austin, R. Cammi, C. Pomelli, J. W. Ochterski, R. L. Martin, K. Morokuma, V. G. Zakrzewski, G. A. Voth, P. Salvador,

J. J. Dannenberg, S. Dapprich, A. D. Daniels, O. Farkas, J. B. Foresman, J. V. Ortiz, J. Cioslowski, D. J. Fox , Gaussian 09, Revision B.01, Wallingford CT (2010).

[26] A. G. Kalampounias, G. N. Papatheodorou, S. N. Yannopoulos, “A temperature-dependent Raman study of the xLiCl-(1–x) TeO_2 glasses and melts”, J. Phys. Chem. Solids, **68**, 1029 (2007).

[27] P. Dumas, J. Corset, W. Carvalho, Y. Levy, Y. Neuman, “Fluorine doped vitreous silica analysis of fiber optic preforms by vibrational spectroscopy”, J. Non-Cryst. Solids, **47**, 239 (1982).

Supplementary data

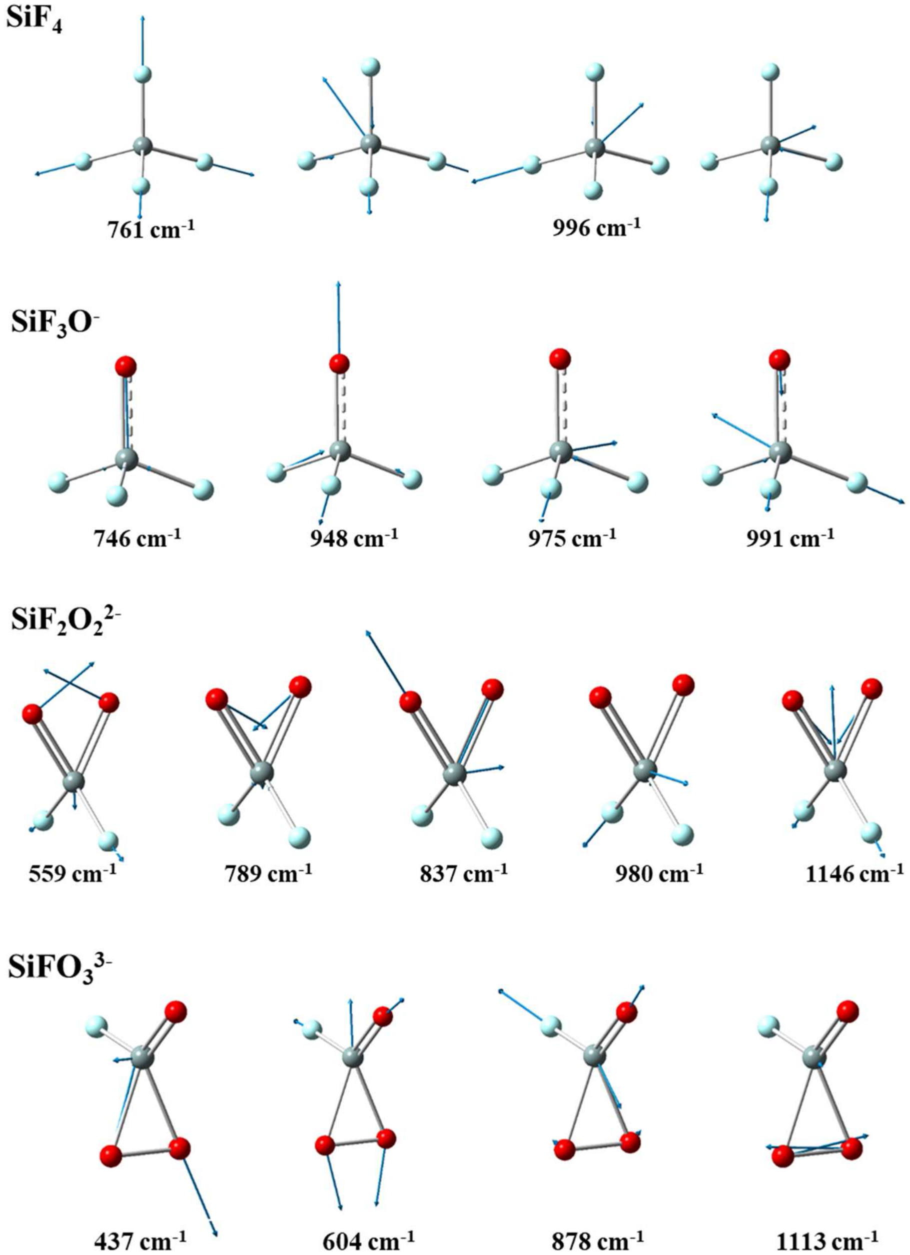

Figure S4-1. Vibrational modes of ion-like species corresponding to each calculated Raman shift wavenumber. The vibrational mode is drawn by displacement vectors.

SiF_3O-Li

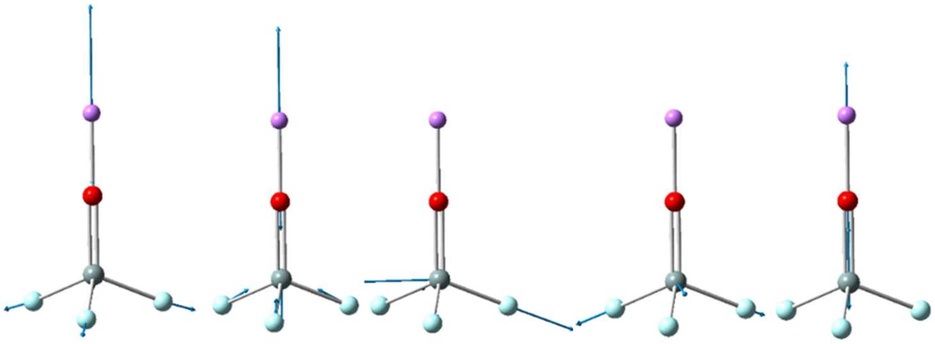

658 cm^{-1} 848 cm^{-1} 906 cm^{-1} 1185 cm^{-1}

SiF_3O-Na

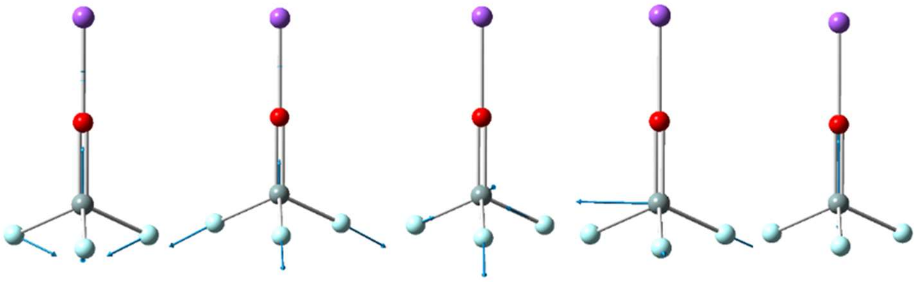

451 cm^{-1} 775 cm^{-1} 887 cm^{-1} 1167 cm^{-1}

SiF_3O-K

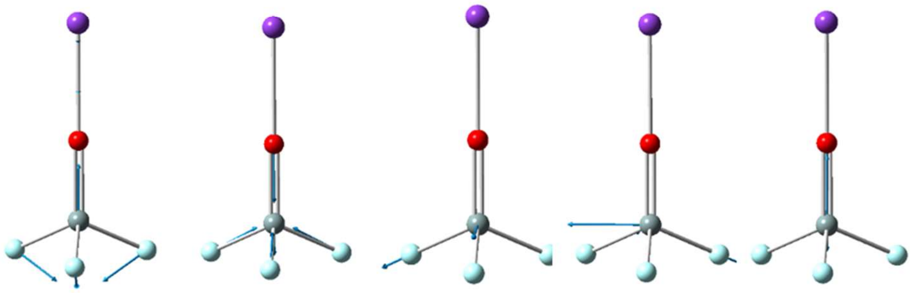

422 cm^{-1} 765 cm^{-1} 881 cm^{-1} 1149 cm^{-1}

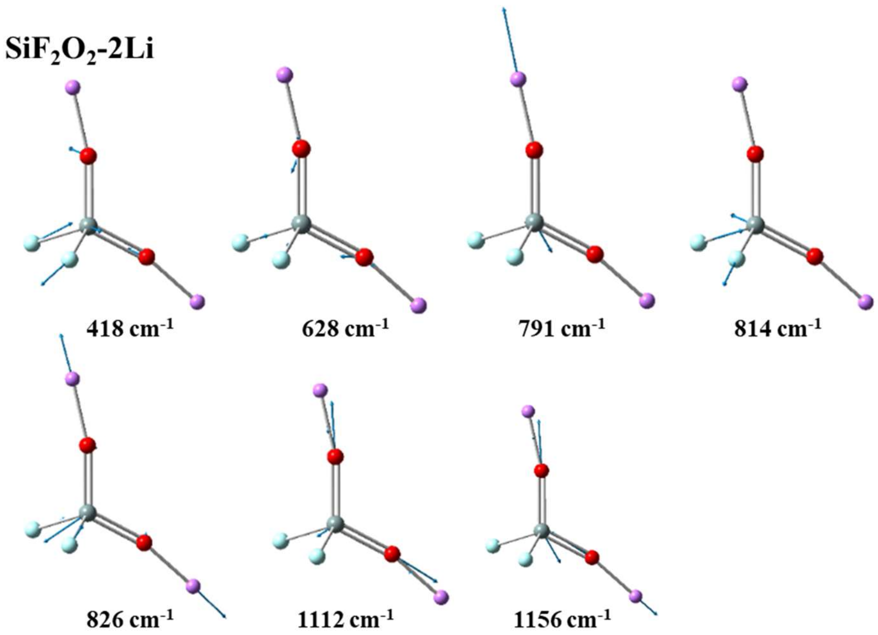

Figure S4-2. Vibrational modes of molecule-like species corresponding to each calculated Raman shift wavenumber. The vibrational mode is drawn by displacement vectors.

CHAPTER 5

Interfacial Phenomena Associated with Electrodeposition of a Reactive Metal (Si, Li) on Liquid Ga Substrates in Propylene Carbonate

5.1. Introduction

Electrochemical reactions between liquid electrolyte/liquid metal substrates historically played a key role in both academic and industrial development of materials processing. One of the best-known studies at the liquid/liquid interface is related to polarography proposed by J. Heyrovský [1]. The study utilizes the dropping of a mercury electrode. Al smelting technology employs a molten fluoride melt/liquid Al cathode interface held above 800 °C [2].

Many studies in the fields of advanced material processing and energy conversion and storage devices [3−10] on the electrochemical reactions at the liquid/liquid interface have recently been published. For example, liquid Cd was used as the cathode in pyrometallugical reprocessing to recover a series of actinides (U, Pu, Np, Am, and Cm) [3−5]. The diffusivity of metals into liquid Cd is measured electrochemically. All-liquid metal batteries, which are comprised of a liquid metal anode/cathode and molten salt electrolyte, have been developed as new candidates for grid-scale batteries [6,7]. Robust liquid metal electrodes, such as the molten Li anode and the molten Li-Bi cathode [8], could prolong battery life.

An electrochemical liquid-liquid-solid (ec-LLS) process was also proposed to fabricate crystalline Si and Ge microwires using a liquid Ga electrode [9,10]. The liquid metal substrate was introduced to initiate the crystal growth of semiconducting materials. However, few studies have been reported on the interfacial phenomena on the liquid metal substrate from the standpoint of macroscopic hydrodynamics, in spite of its technological importance in the fields of solvent extraction and metallurgical processing. The effects of chemical or electrochemical reactions on such interfacial flow behavior has often been neglected.

In-situ optical observations are indispensable to qualitatively comprehend the interfacial phenomena at the liquid/liquid interface. However, the high temperature electric field introduces many technical difficulties. Liquid Ga is now proposed as the liquid metal electrode because of its low melting point of 29.8°C. This chapter introduces an electrochemical cell comprised of a liquid Ga electrode onto which Li or Si is electrodeposited in propylene carbonate (PC) to visualize interfacial phenomena. In regards to Li electrodeposition, many papers have been published involving solid metal substrates for the development of advanced energy storage devices that are superior to conventional lithium batteries [11–16]. The difference between the interfacial phenomena on solid and liquid Ga substrates is also discussed.

5.2. Experimental

The electrolytic cell was assembled in a glove box filled with purified Ar gas, as schematically demonstrated in Fig. 5-1. All electrochemical measurements were conducted under an Ar atmosphere. PC (98.0% FUJIFILM Wako Pure Chemical Corporation) containing various concentrations of $LiClO_4$ (98.0%, FUJIFILM Wako Pure Chemical Corporation) or $SiCl_4$ (>99.0%, FUJIFILM Wako Pure Chemical Corporation) was used as the electrolyte. For Si electrodeposition, tetrabutylammonium hexafluorophosphate (TBAPF$_6$, >95%, FUJIFILM Wako Pure Chemical Corporation) was used as the supporting electrolyte. The initial content of water contamination in purchased PC was reported to be less than 20 ppm. The working electrode was solid and liquid Ga metal (99.99999 %, The Nilaco Corporation). The elliptical solid Ga metal was connected to a Ni wire (99.35%, φ 1 mm, Sumiden Fine Conductors Co., Ltd.) for the electrically conductive lead. The lead was introduced through a high-purity alumina tube (99.5 wt% Al$_2$O$_3$, SSA-S grade, NIKKATO CORPORATION), which prevented contact between the electrolyte and Ni wire. The liquid Ga cathode was contained in a Pyrex beaker (φ 25 × 32 mm) that was also connected to a Ni wire through a high-purity alumina tube. Li wires (φ 3 mm, Chempur) were used as reference and counter electrodes.

The electrode surface area of the solid Ga electrode was determined by elliptical approximation and that of the liquid Ga electrode was defined by the geometric surface area based on the diameter of the beaker. The reactivity of Ga with Ni as an electrical lead could be ignored because the reaction rate of Ga with Ni is too low to influence the experimental results at this temperature.

A potentiostat/galvanostat (VSP, BioLogic) was employed for electrochemical measurements. XRD (MultiFlex, Rigaku Corporation), using Cu Kα radiation, was employed to characterize the deposited samples by potentiostatic electrolysis. The prepared deposit at 15 C cm^{-2} was put on a glass plate in a glove box and wrapped with an X-ray-translucent and flexible film (Pechiney Plastic Packaging, Parafilm), preventing the sample surface from being partially oxidized in the atmospheric air.

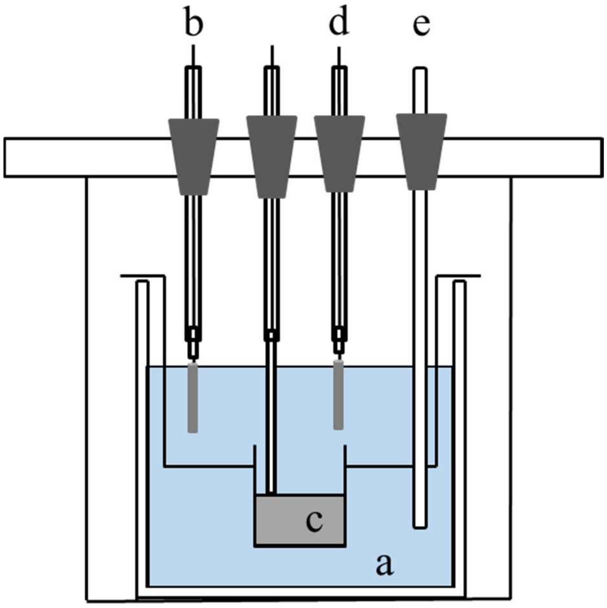

Figure 5-1. Schematic drawing of the experimental setup: (a) PC-$LiClO_4$, (b) Li reference electrode, (c) liquid Ga electrode, (d) Li counter electrode and (e) thermocouple.

5.3. Results and discussion

5.3.1. The initial stage of Li electrodeposition on solid and liquid Ga substrates

In order to elucidate the differences in electrochemical reactions of Li^+ at the interface between PC and liquid or solid Ga substrates, potential sweep measurements were carried out. At the beginning, the linear sweep voltammograms obtained from both solid and liquid Ga substrates were compared. Figures 5-2 (a) and (b) show both voltammograms at various scan rates in PC-$LiClO_4$ (0.1 mol L^{-1}). The reduction currents appeared around 1.0 V during the cathodic potential sweep on both Ga substrates. The reduction peak in CV appeared on the solid Ga substrate, whose peak current increased and peak location shifted to more negative potentials with increasing sweep rate. On the other hand, such a reduction peak cannot be clearly recognized above 20 mV s^{-1} on the liquid Ga cathode. Moreover, the reduction peak location moved a considerable amount toward positive potentials with increasing sweep rate below 10 mV s^{-1}.

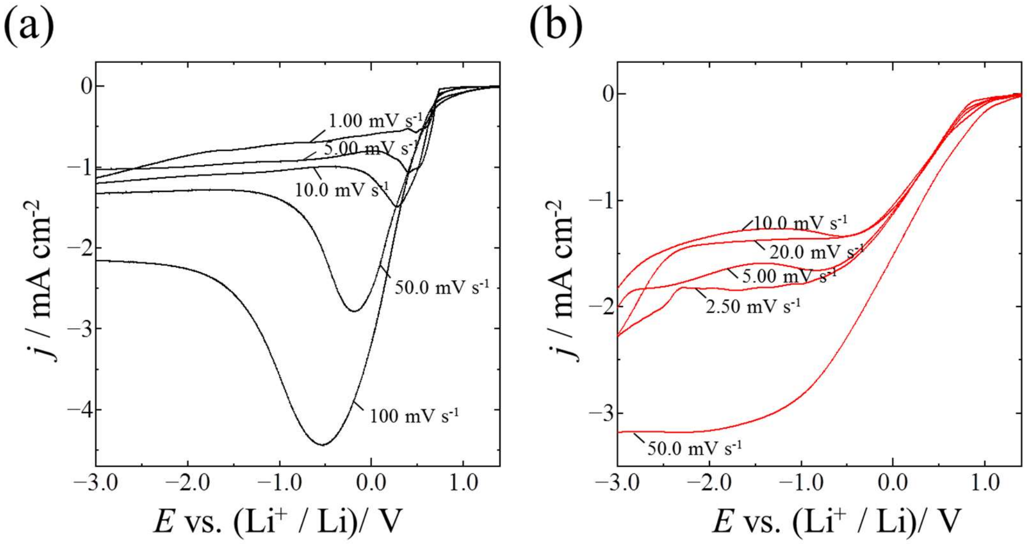

Figure 5-2. Linear sweep voltammograms for a (a) solid Ga electrode at 25°C and (b) liquid Ga electrode at 40°C in PC-$LiClO_4$ (0.1 mol L^{-1}).

Figures 5-3 (a) and (b) show the plots of current peak versus the square root of the scan rate based on the results shown in Fig. 5-2. It is well known that the reduction current increases with increasing scan rates in a diffusion-limited condition [17]. Figure 5-3 (a) shows a good linear correlation between the current peak and the square root of the scan rate. However, this behavior is notably absent in the case of the liquid Ga substrate at 40°C shown in Fig. 5-3 (b). This difference was attributed to the formation of liquid the Ga-Li alloy phase, as expected from the phase diagram in Fig. 5-4 [18]. The alloy phase was formed by increasing the concentration of reduced Li onto liquid Ga. The significantly different shapes of reduction currents in the CVs for the liquid Ga substrate, compared to solid Ga, was therefore caused by the formation of liquid Ga-Li alloy.

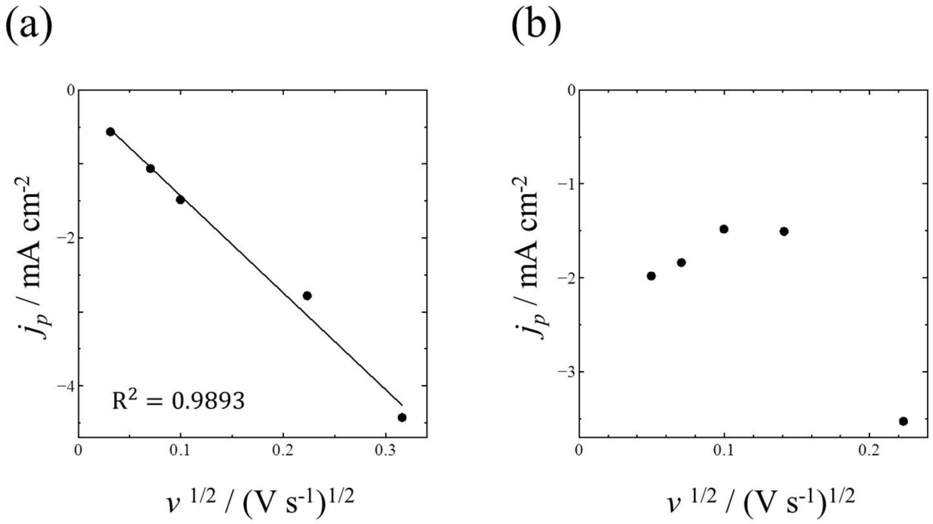

Figure 5-3. Reduction peak current dependence on the square root of the scan rate for a (a) solid Ga electrode at 25°C and (b) liquid Ga electrode at 40°C in PC-LiClO$_4$ (0.1 mol L^{-1}).

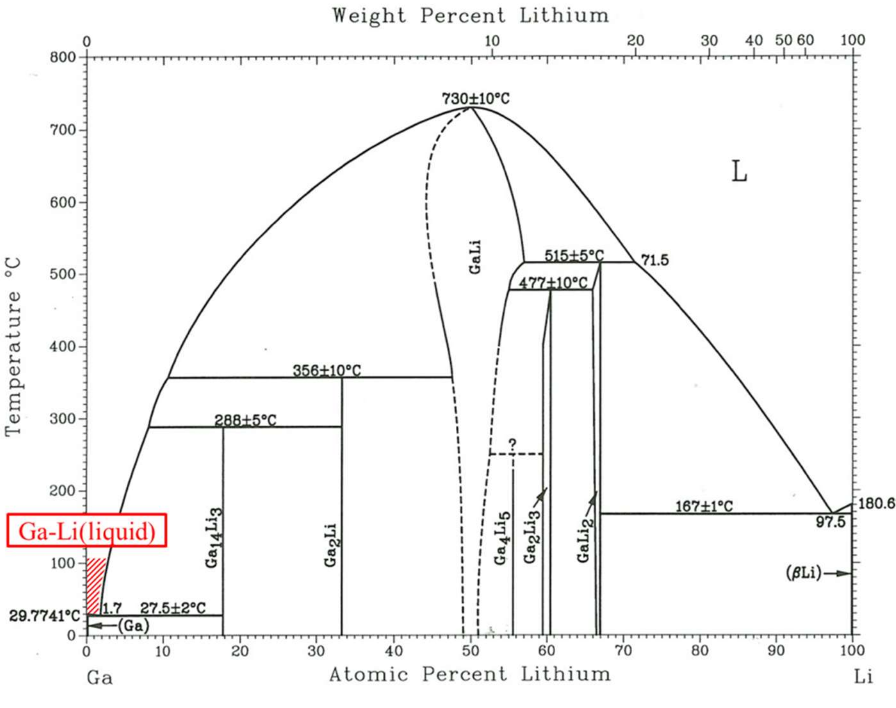

Figure 5-4. Phase diagram of the Ga-Li system [18].

The appearance of the liquid PC/liquid Ga interface was carefully observed using in-situ video imaging. Figure 5-5 shows the time transient of interfacial variations of the liquid Ga electrode from a lateral view recorded during potentiostatic polarization at −1.0 V for 0 min and 10 min in PC-$LiClO_4$ (0.01 mol L^{-1}). The video image reveals interfacial flow phenomena as the potentiostatic operation progressed. Before applying the potential, the liquid Ga electrode top-surface shows a macroscopically convex shape. The interfacial shape appearance begins to change as the potential is applied. A radial flow pattern is induced on the liquid Ga electrode, toward the beaker wall, resulting in a flat shape of the liquid Ga electrode surface. This phenomenon may be partly due to the interfacial tension difference between liquid Ga (electrode) and liquid Ga-Li alloy (formed on the electrode) as well as the Ga surface tension change resulting from the applied potential [19]. The Ga-Li phase diagram in Fig. 5-4 indicates the existence of a Ga-Li (liquid) phase above 29.8°C (the eutectic temperature is 27.5°C).

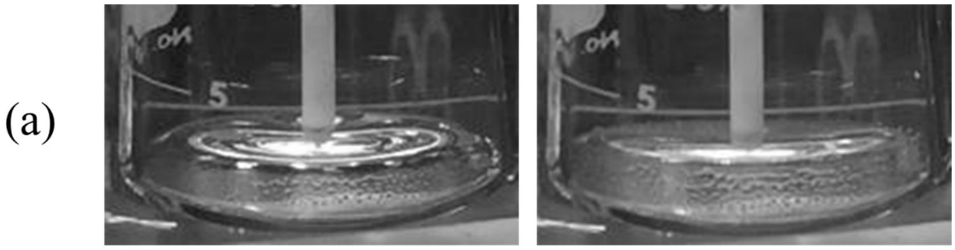

Before electrolysis After 10 min

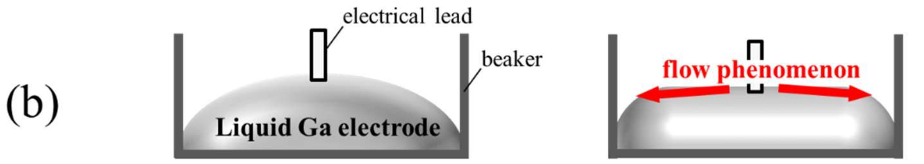

Before electrolysis Time progress of electrolysis

Figure 5-5. (a) Video images and (b) illustrations before and after potentiostatic electrolysis at −1.0 V in PC-$LiClO_4$ (0.01 mol L^{-1}) at 40°C

The difference in electrochemical response between the liquid and solid Ga substrate is also seen in the current-time transients during the initial stage of electrolysis, as shown in Fig. 5-6. The current-time transient curves were obtained by potentiostatic polarization between −1.0 V and 0.75 V in PC-$LiClO_4$ (0.1 mol%) on both substrates. On the solid Ga substrate, the typical current peaks appeared with applied potential, although no current peaks were observed at any potentials on the liquid Ga substrate. The typical peaks observed on the solid Ga substrate represent the growth of solid Ga-Li alloy phase (0, 0.25, 0.50, and 0.75 V) and Li metal phase (−0.50 and −1.0 V) at the PC/solid Ga interface. Figure 5-6 (a) shows increased current density, stemming from expanding surface area corresponding to the growth of the Ga-Li alloy phase and the Li metal phase, followed by decreased current density, from the overlap of the diffusion zone of the Li ion in the electrolyte under diffusion-limited conditions [20]. The rapid current decrease at −0.5 and −1.0 V for the solid Ga electrode may be partly due to solid electrolyte interphase formation on the electrodeposited Li.

On the other hand, the current-time transient on the liquid Ga substrate demonstrated that the electrodeposition mechanism of Li at the PC/liquid Ga substrate interface could not be interpreted by a conventional nucleation and growth mechanism based on a solid metal substrate. The physicochemical aspects of Ga-Li(liquid) phase formation by dissolution of electrodeposited Li atoms into the liquid Ga substrate must be further understood during the initial stages of Li electrodeposition at the liquid/liquid interface.

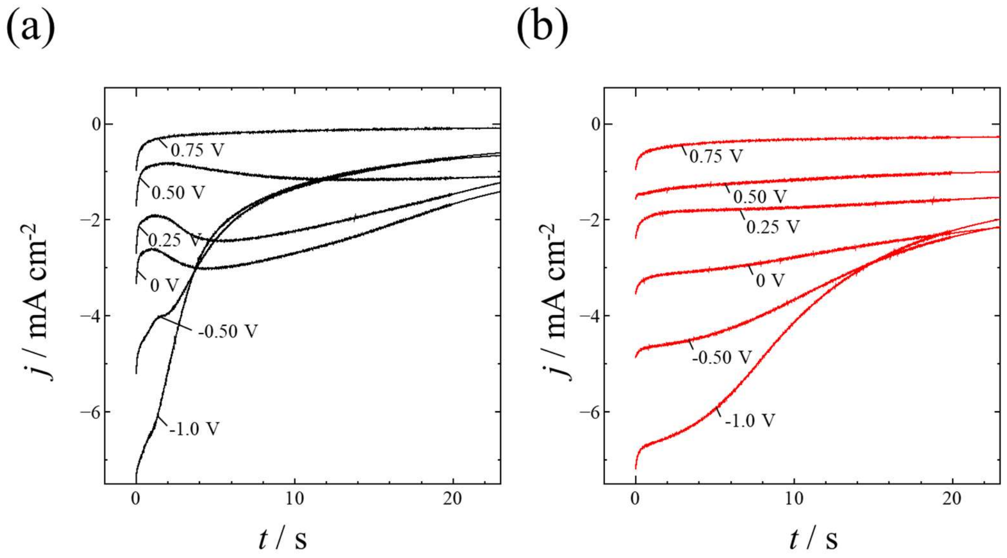

Figure 5-6. Current-time transient curves of potentiostatic polarization for a (a) solid Ga electrode at 25°C and (b) liquid Ga electrode at 40°C in PC-$LiClO_4$ (0.1 mol L^{-1}).

5.3.2. Characterization of electrodeposits at larger electrical charge

In order to characterize the electrodeposition process on solid and liquid Ga substrates, potentiostatic electrolysis was further conducted at −2.8 V. Figure 5-7 shows photographs of solid and liquid Ga substrate surfaces taken for 0, 1.0, and 15 C cm^{-2} at −2.8 V in PC-$LiClO_4$ (1.0 mol L^{-1}). Dendritic growth of Li was observed on the solid Ga substrate with increasing electric charge density. At 15 C cm^{-2}, the surface of the solid Ga substrate became darker due to significant dendritic electrodeposition of Li, resulting in poorer light reflection onto the camera film.

On the other hand, the appearance of the liquid Ga substrate changed from convex curvature to a flat shape from 0 to 1.0 C cm^{-2}. This result corresponds to liquid Ga-Li phase formation at the initial stage, as discussed in Section 5.3.1. In addition, with increasing electric charge density, a $Ga_{14}Li_3$ film was formed on the liquid Ga substrate at 15 C cm^{-2}, which was identified by the XRD shown in Fig. 5-8. This result indicates that the phase formation on the liquid Ga substrate proceeds according to the lever rule in the Ga-Li binary phase diagram.

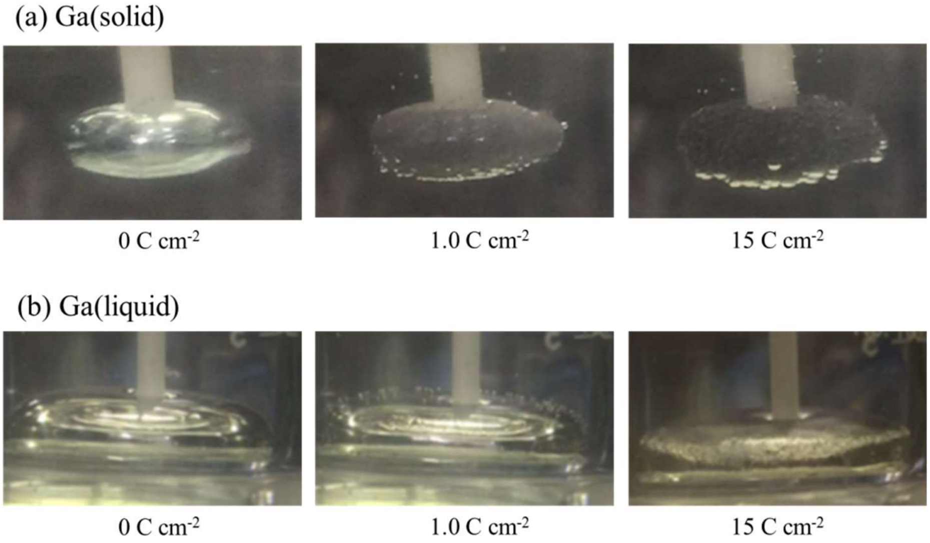

Figure 5-7. Images of a (a) solid Ga electrode at 25 °C and (b) liquid Ga electrode at 40 °C during potentiostatic electrolysis at 0, 1.0, and 15 C cm^{-2} in PC-LiClO$_4$ (1 mol L^{-1}).

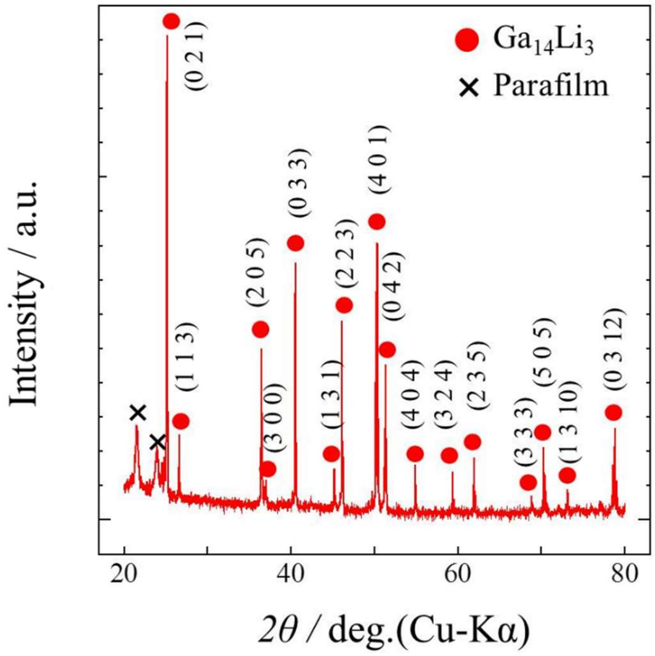

Figure 5-8. XRD pattern of the sample after potentiostatic electrolysis at 40 °C in PC-LiClO$_4$ (1 mol L^{-1}).

5.3.3. A model of the electrodeposition mechanism of Li on liquid Ga

A model of the Li electrodeposition process is proposed based on the experimental results of the initial stage of the liquid PC/liquid Ga interface during Li electrodeposition. Figure 5-9 shows the model, which involves three stages. In the first stage, Li^+ ions dissolved in PC were reduced. Reduced Li atoms are formed on the liquid Ga electrode. The diffusion rate of Li into liquid Ga is low and the concentration of Li at the Li/Ga interface increases slowly to reach the liquidus line shown in Fig. 5-4.

During the second stage, a liquid phase Ga-Li alloy starts to appear. This stage accompanies the flow phenomena at the liquid PC/liquid Ga interface caused by the interfacial tension difference between the liquid Ga and the liquid Ga-Li alloy. It may result from the liquid electrode surface potential gradient as well as the Li concentration difference. The Li composition of the liquid Ga-Li alloy cannot exceed the eutectic composition of 1.7% atomic fraction Li, which is possibly higher at elevated temperatures. In the third stage, a solid phase Ga-Li alloy ($Ga_{14}Li_3$) is formed from the increasing Li concentration on the liquid Ga due to the lever rule in the Ga-Li binary phase diagram.

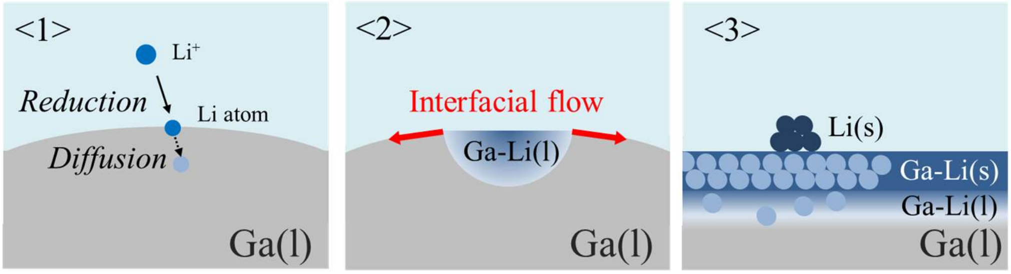

Figure 5-9. Electrodeposition mechanism model of Li on liquid Ga electrodes.

5.3.4. Electrodeposition of Si on liquid Ga substrates

Figure 5-10 shows cyclic voltammograms for solid Ag and liquid Ga substrates in PC containing 0.05 mol L^{-1} $TBAPF_6$ and $SiCl_4$ (0, 0.01, and 0.1 mol L^{-1}) at 40 °C under Ar atmosphere. As can be seen in Fig. 5-10 (a), the cathodic current was increased after adding $SiCl_4$ in the electrolyte when using a Ag substrate, indicating that the Si(IV) ion was electrochemically reduced. The increase of cathodic current was also observed for the liquid Ga substrate, as shown in Fig. 5-10 (b). Figure 5-11 shows the current-time transient curves obtained by potentiostatic polarization at −2.5, −2.8, and −3.1 V on the liquid Ga substrate. The data followed similar behavior to those recorded in the PC-$LiCl_4$ system, shown in Fig. 5-6, suggesting dynamic instability at the liquid metal/liquid electrolyte interface during Si electrodeposition. This result shows that it is necessary to control the interfacial phenomena when fabricating high-quality Si layers on liquid metal cathodes.

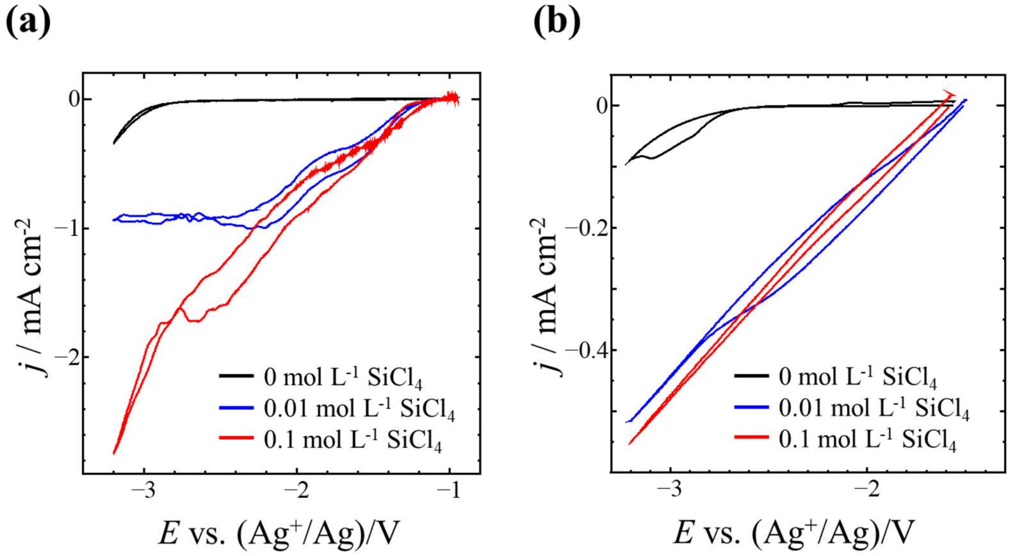

Figure 5-10. Cyclic voltammograms for a (a) solid Ag electrode and (b) liquid Ga electrode in PC containing 0.05 mol L^{-1} $TBAPF_6$ and $SiCl_4$ (0, 0.01, and 0.1 mol L^{-1}) at 40°C.

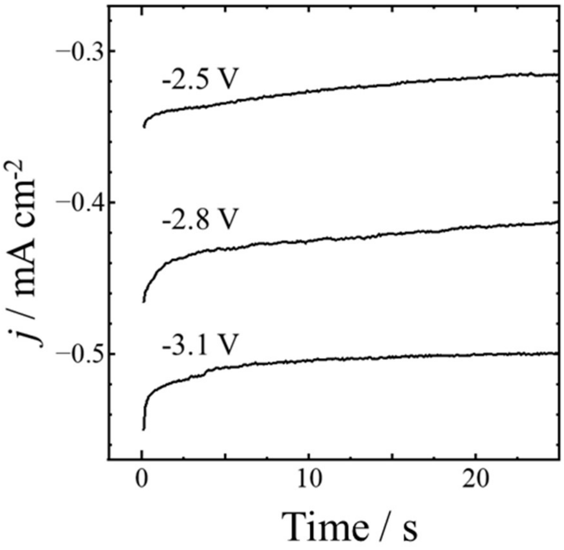

Figure 5-11. Current-time transients for a liquid Ga electrode in PC containing 0.05 mol L^{-1} TBAPF$_6$ and 0.1 mol L^{-1} SiCl$_4$ at 40°C.

5.4. Conclusions

The initial stage of Li electrodeposition at the propylene carbonate/liquid Ga interface was investigated in PC-LiClO$_4$ at 40 °C. Interfacial flow phenomena induced by the interfacial tension difference between liquid Ga and the liquid Ga-Li alloy formed on the liquid Ga substrate were observed under potentiostatic electrolysis at −1.0 V. In addition, a solid Ga$_{14}$Li$_3$ alloy formed on the liquid Ga substrate with larger electrical charge. This indicated that phase formation on the liquid Ga substrate progressed with limited diffusion of electrodeposited Li atoms into the liquid Ga substrate. Future work should consider macroscopic hydrodynamics induced by chemical and electrochemical reactions at the liquid electrolyte/liquid metal interfaces for tailoring electrodeposited film or developing safe and sustainable power storage devices. The electrochemical behavior of silicon ions on the liquid Ga substrate followed similar behavior to those recorded in the PC-LiCl$_4$ system, suggesting dynamic instability at the liquid metal/liquid electrolyte interface during Si electrodeposition.

References

[1] J. Heyrovský, “Elektrolysa se rtufovou kapkovou kathodou”, Chemické Listy, **16**, 256 (1922).

[2] R. Moreau, J. W. Evans, “An analysis of the hydrodynamics of aluminum reduction cells”, J. Electrochem. Soc., **131**, 2251 (1984).

[3] T. Murakami, Y. Sakamura, N. Akiyama, S. Kitawaki, A. Nakayoshi, “Electrochemical measurement of diffusion coefficient of Pu in liquid Cd”, J. Electrochem. Soc., **161**, D3057 (2014).

[4] T. Murakami, Y. Sakamura, N. Akiyama, S. Kitawaki, A. Nakayoshi, T. Koyama, “Electrochemical measurement of diffusion coefficient of actinides and rare earths in liquid Cd”, Procedia Chemistry, **7**, 798 (2012).

[5] T. Koyama, M. Iizuka, N. Kondo, R. Fujita, H. Tanaka, “Electrodeposition of uranium in stirred liquid cadmium cathode”, J. Nucl. Mater., **247**, 227 (1997).

[6] H. Kim, D. A. Boysen, J. M. Newhouse, B. L. Spatocco, B. Chung, P. J. Burke, D. J. Bradwell, K. Jiang, A. A. Tomaszowska, K. Wang, W. Wei, L. A. Ortiz, S. A. Barriga, S. M. Poizeau, D. R. Sadoway, “Liquid metal batteries: past, present, and future”, Chem. Rev., **113**, 2075 (2013).

[7] K. Wang, K. Jiang, B. Chung, T. Ouchi, P. J. Burke, D. A. Boysen, D.J. Bradwell, H. Kim, U. Muecke, D. R. Sadoway, “Lithium–antimony–lead liquid metal battery for grid-level energy storage”, Nature Lett., **514**, 348 (2014).

[8] X. Ning, S. Phadke, B. Chung, H. Yin, P. Burke, D. R. Sadoway, “Self-healing Li–Bi liquid metal battery for grid-scale energy storage”, J. Power Sources, **275**, 370 (2015).

[9] J. Gu, E. Fahrenkrug, S. Maldonado, “Direct electrodeposition of crystalline silicon at low temperatures”, J. Am. Chem. Soc., **135**, 1684 (2013).

[10] L. Ma, E. Fahrenkrug, E. Gerber, A. J. Crowe, F. Venable, B. M. Bartlett, S. Maldonado, “High-performance polycrystalline Ge microwire film anodes for Li ion batteries”, ACS Energy Lett., **2**, 238 (2017).

[11] D. Aurbach, M. L. Daroux, P. W. Faguy, E. Yeager, “Identification of surface films formed on lithium in propylene carbonate solutions”, J. Electrochem. Soc., **134**, 1611 (1987).

[12] K. Kanamura, H. Tamura, Z. Takehara, “XPS analysis of a lithium surface immersed in propylene carbonate solution containing various salts”, J. Electroanal. Chem., **333**, 127 (1992).

[13] M. Inaba, H. Yoshida, Z. Ogumi, T. Abe, Y. Mizutani, M. Asano, “In situ Raman study on electrochemical Li intercalation into graphite”, J. Electrochem. Soc., **142**, 20 (1995).

[14] X. Wang, E. Yasukawa, S. Mori, “Electrochemical behavior of lithium imide/cyclic ether electrolytes for 4 V lithium metal rechargeable batteries”, J. Electrochem. Soc., **146**, 3992 (1999).

[15] R. Selim, P. Bro, “Some observations on rechargeable lithium electrodes in a propylene carbonate electrolyte”, J. Electrochem. Soc., **121**, 1457 (1974).

[16] T. Nishida, K. Nishikawa, M. Rosso, Y. Fukunaka, “Optical observation of Li dendrite growth in ionic liquid”, Electrochim. Acta, **100**, 333 (2013).

[17] J. E. B. Randles, “A cathode ray polarograph. Part II.—The current-voltage curves”, Trans. Faraday Soc., **44**, 327(1948).

[18] T. B. Massalski, Binary Alloy Phase Diagrams, 4th ed., Vol. 2, ASM International, Ohio, 2001.

[19] J. O'M. Bockris, A. K. N. Reddy, Modern Electrochemistry, Vol. 2, Chapter 7,

Plenum Press, New York, 1970.

[20] B. Scharifker, G. J. Hills, "Theoretical and experimental studies of multiple nucleation", Electrochim. Acta, **28**, 879 (1983).

CHAPTER 6

Corrosion Behavior of Stainless Steels and Ni-based Alloys in Chloride Melts

6.1. Introduction

Corrosion behavior of structural materials in high temperature molten salt is necessary to investigate for the design of robust power generation infrastructures, such as molten salt electrolysis and applications of nuclear technology discussed in Chapter 1. It is easy to anticipate that the corrosion of metal at the structural material/high temperature molten salt interface progresses on the moon and Mars because of oxygen generated in the molten salt electrolysis process. In this chapter, corrosion rate of structural materials in high temperature molten salt is assessed by means of a brief and specific method.

Chloride melt is a candidate for molten salt electrolyte and for applications in nuclear technology. For example, a molten salt reactor (MSR) on the moon is a promising power generation infrastructure [1], which uses locally sourced uranium and thorium [2,3]. The MSR, which was first developed at Oak Ridge National Laboratory in the 1950s to 1970s, is one of the nuclear power plant concepts planned for Generation IV systems on Earth [4–6]. Since a nuclear fuel is dissolved into molten salt of the primary loop, MSR use would substantially decrease the amount of high-level radioactive waste originating from nuclear power plants [7]. Recently, M. Yamawaki et al. proposed the new concept of an Integral Molten Salt Fast Reactor (IMSFR), which consists of a combination of an MSR fueled with chloride molten salt and a chloride-based pyrochemical processing subsystem, as a highly efficient transmutation system for transuranium elements [8].

Corrosion of structural materials, which occurs through electrochemical reaction between metals and high temperature molten salt, is a serious problem when considering the practical utilization of molten chloride. Some researchers have focused on the corrosion phenomena of metals in several chloride melts, such as NaCl-KCl-$ZnCl_2$ [9], $MgCl_2$-KCl [10], $MgCl_2$-NaCl-KCl [11], and LiCl-KCl-$EuCl_3$ [12]. NaCl-$CaCl_2$ melt is one of the promising candidates as the molten salt of the primary loop and coolant, however little experimental work has been done on the corrosion behavior of metals in this melt. The suitable metallic element for the structural material must be determined. In order to discuss fundamental corrosion behavior in the melt, it is necessary to examine the corrosion rate of two major types of alloy: stainless steel and Ni-based alloys, such as Inconel and Hastelloy. Two types of electrochemical methods, linear polarization and the electrochemical impedance technique, are investigated in order to understand the comprehensive corrosion behavior of these alloys in NaCl-$CaCl_2$ melt.

6.2. Experimental

NaCl (99.5%, FUJIFILM Wako Pure Chemical Corporation) and $CaCl_2$ (>99.9%, Kojundo Chemical Laboratory Co., Ltd.) were mixed in a eutectic composition (NaCl-$CaCl_2$ = 47.9:52.1 mol%) and placed in an alumina crucible. The mixture was kept under vacuum for more than 48 h at 473 K to expel its water content.

For the electrochemical experiments, all measurements were performed under a dry Ar atmosphere. The cell was heated using a programmable furnace and the temperature of the cell was measured using a chromel-alumel thermocouple with an accuracy of ±1 K. The tested alloys were: SUS304 (POSCO), SUS316 (NIPPON STEEL CORPORATION), SUS430 (JFE Holdings, Inc.), Inconel 600 (Special Metals Corporation), Inconel X750 (Allegheny Technologies Incorporated), Hastelloy C-276 (Nippon Yakin Kogyo Co., Ltd.), and Incoloy 800 (Daido Steel Co., Ltd). Pure Fe, Mo, and Ni plates were also tested. The size of each sample was 1.0 × 0.8 cm. All working electrodes were mechanically polished with fine-grained emery paper followed with 0.05-μm alumina-water suspension to obtain a mirror surface. Before testing, each sample was cleaned ultrasonically with acetone and attached to a Ni wire (99.35%, φ 1 mm, Sumiden Fine Conductors Co., Ltd.) as the electrically conductive lead. The counter electrode was a glassy carbon rod (3-mm diameter, TOKAI CARBON Co., Ltd.). The reference electrode was a Ag wire immersed in eutectic NaCl-$CaCl_2$ melt containing 1 mol% AgCl in an alumina tube provided with a thin bottom. The potential of this electrode was calibrated with reference to that of the Ca(II)/Ca electrode, which was prepared by electrodepositing calcium metal on a nickel wire. A potentiostat/galvanostat (VSP, BioLogic) was used for electrochemical measurements.

The weight fraction of the constituent element for the measured alloys was determined by glow discharge optical emission spectroscopy (GD-OES, GD-Profiler2, HORIBA, Ltd.). The surface chemical states of samples were analyzed by XRD (MultiFlex, Rigaku Corporation) with a Cu Kα line.

6.3. Results and discussion

6.3.1. Linear polarization curves

The linear polarization (LP) technique was carried out to reveal corrosion behavior in the eutectic NaCl-$CaCl_2$ melt. In this technique, corrosion current density I_{corr} and corrosion potential E_{corr} were evaluated by the Tafel gradient. Figure 6-1 shows the LP curves for Fe-based alloys (SUS304, SUS316, and SUS430) at a scan rate of 0.166 mV s^{-1}. Figure 6-2 shows the LP curves of Ni-based alloys (Inconel600, InconelX750, and HastelloyC-276) and Incoloy800. As can be seen in Fig. 6-2, the Ni-based alloy and Incoloy800 exhibited different polarization curves while the stainless steels exhibited similar behavior. Hastelloy C-276 had the most notable corrosion potential, suggesting that it has the highest corrosion resistance among the Ni-based alloys measured. While it is known that Hastelloy alloy has high corrosion resistance in molten fluoride systems, this result shows that Hastelloy alloy has high corrosion resistance even in NaCl-$CaCl_2$ melt.

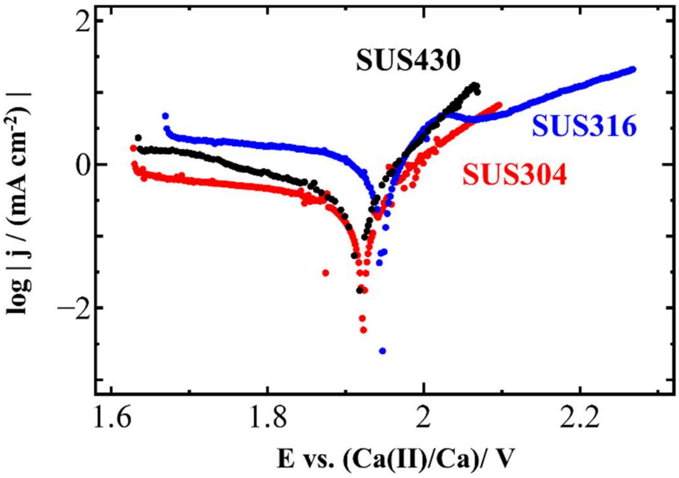

Figure 6-1. Linear sweep polarization curves of stainless steels (SUS304, SUS316, and SUS430).

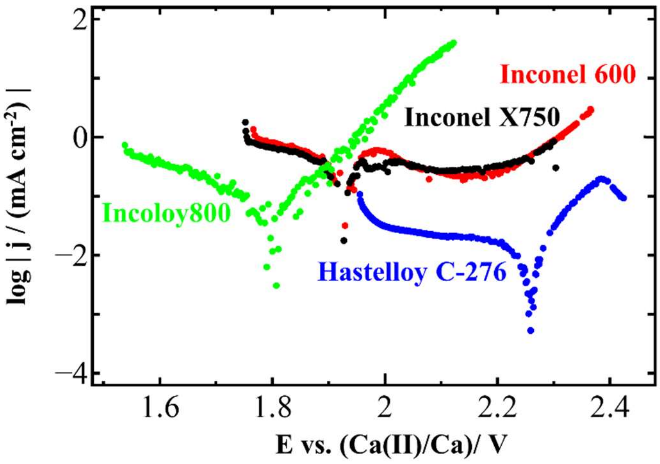

Figure 6-2. Linear sweep polarization curves of Ni-based alloys (Inconel600, InconelX750, and HastelloyC-276) and Incoloy800.

From the results of the LP curves, the corrosion rate of each alloy was calculated based on Eq. (6-1),

$$(Corrosion\ Rate) = \frac{I_{corr} \cdot K}{\rho \Sigma\left(\frac{f_i n_i}{MW_i}\right)} \tag{6-1}$$

where I_{corr} is the corrosion current density, K is a constant equal to 3272 [mm A^{-1} cm^{-1} year^{-1}], ρ is the density of measured samples, f_i is the weight fraction of element i in the alloy, N_i is the number of electrons being transferred in element i per mole, and MW_i is the atomic weight of element i. Tables 6-1 and 6-2 represent the measured values of f_i by GD-OES analysis for stainless steels, Ni-based alloys, and Incoloy800, which were used for calculating corrosion rate. N_i was assumed to be 2 for Fe, Cr, Ni, Mn, Cu, C, Co, and W; 3 for Mo, Nb, Ti, Mo, and V; and 4 for Si. Table 6-3 summarizes the calculated corrosion rates of Fe-based and Ni-based alloys. The corrosion rates of the Fe-based alloys were similar whereas the rates of the Ni-based alloy were different. HastelloyC-276 had the slowest corrosion rate, followed by Incoloy800, InconelX750, and Inconel600. Also, the Ni-based alloys tended to have a slower corrosion rate than Fe-based alloys, which indicates that Ni-based alloys have high corrosion resistance in the melt.

Table 6-1. The weight fraction of constituent element *i*, (f_i), used for calculating corrosion rate (Eq. (6-1)) for stainless steels.

f_i (wt.%)	SUS304	SUS316	SUS430
Fe	75.32	72.61	84.13
Cr	16.46	15.01	14.77
Ni	6.47	8.15	0.09
Mn	0.85	0.90	0.47
Si	0.40	0.35	0.25
Cu	0.27	0.22	0.08
C	0.15	0.06	0.14
Co	0.08	0.07	0.03
Mo	0.00	2.62	0.04
Al	0.00	0.01	0.00

Table 6-2. The weight fraction of constituent element i, (f_i), used for calculating corrosion rate (Eq. (6-1)) for Ni-based alloys and Incoloy800.

f_i (wt.%)	Inconel600	InconelX750	HastelloyC-276	Incoloy800
Fe	7.91	5.32	4.83	49.42
Cr	16.49	17.03	12.11	18.34
Ni	74.62	72.68	68.35	29.50
Mn	0.20	0.15	0.36	0.80
Si	0.22	0.10	0.09	0.23
Cu	0.03	0.03	0.08	0.17
C	0.04	0.05	0.01	0.16
Co	0.02	0.08	0.06	0.04
Mo	0.17	0.00	12.75	0.56
Al	0.16	1.02	0.09	0.44
Ti	0.14	2.20	0.01	0.35
Nb	0.00	1.34	0.00	0.00
W	0.00	0.00	1.25	0.00
V	0.00	0.00	0.02	0.00

Table 6-3. Corrosion data of stainless steels (SUS304, SUS316, and SUS430), Ni-based alloys (Inconel600, InconelX750, and HastelloyC-276), and Incoloy800.

Sample	E_{corr} / V	I_{corr} / μA cm^{-2}	Corrosion rate / mm year^{-1}	R_{ct} / Ω cm^2
SUS304	1.92	415	4.66	176
SUS316	1.96	1136	12.8	225
SUS430	1.92	544	6.26	937
Incoloy800	1.74	99.0	1.11	411
Inconel600	1.92	430	4.72	1069
InconelX750	1.88	369	4.26	827
HastelloyC-276	2.21	24.0	0.240	894

6.3.2. Electrochemical impedance spectroscopy

In this section, the corrosion behavior of each alloy was evaluated using the electrochemical impedance spectroscopy (EIS) method, which is the other method for investigating corrosion behavior. The EIS method is used to identify and quantify the physicochemical processes occurring at the metal/molten salt interface depending on different AC frequencies [11]. Figures 6-3 and 6-4 show Nyquist plots of the stainless steels and the Ni-based alloys. The data were obtained in the frequency range between 100 kHz and 10 mHz with the amplitude of ±10 mV at E_{corr} of each sample. The E_{corr} value was derived from LP measurements, as shown in Table 6-3. The curves drawn by the solid lines in Figs. 6-3 and 6-4 show the fitting curve by means of EC-Lab software (ver. 11.30, BioLogic). Each fitting curve was drawn based on the equivalent circuit shown in Fig. 6-5. In addition, the charge transfer resistance (R_{ct}) of each material obtained from the fitting result is summarized in Table 6-3. Table 6-3 indicates that the parameter R_{ct} for the corrosion of Inconel600 had the largest value, then HastelloyC-276, InconelX750, and Incoloy800, except stainless steels. Comparing the results of EIS with the results of the LP technique, Ni-based alloys have higher corrosion resistance than stainless steels in the NaCl-$CaCl_2$ melt.

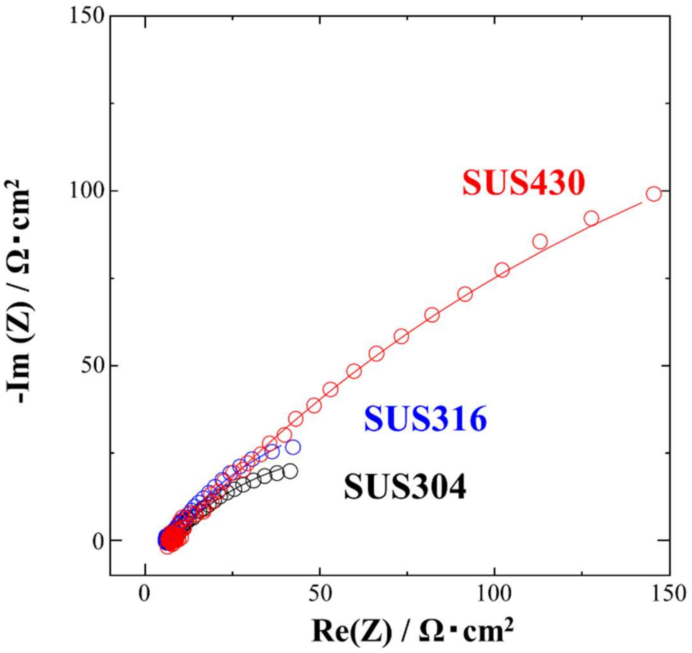

Figure 6-3. Nyquist plots of stainless steels (SUS304, SUS316, and SUS430).

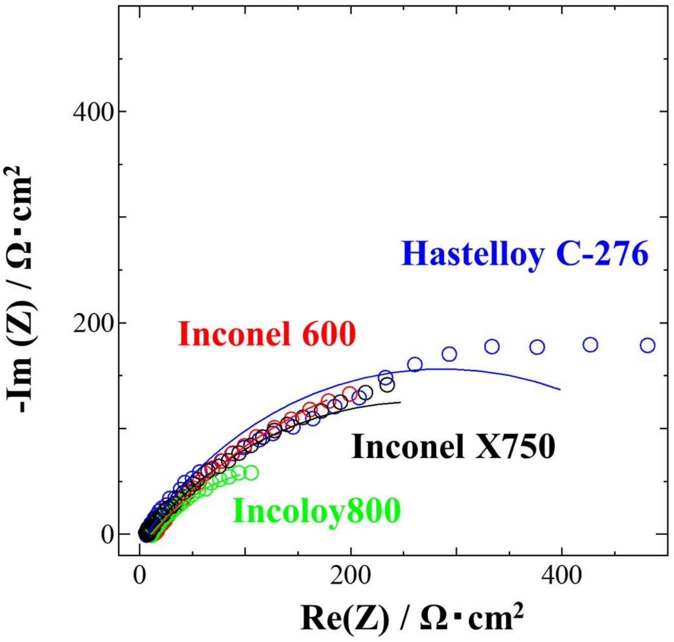

Figure 6-4. Nyquist plots of Ni-based alloys (Inconel600, InconelX750, and HastelloyC-276) and Incoloy800.

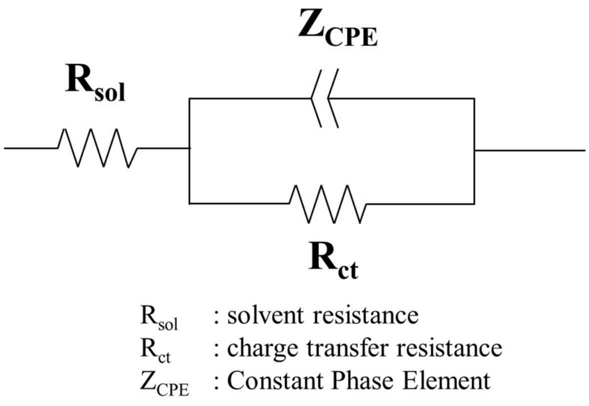

Figure 6-5. Equivalent circuit.

6.3.3. Corrosion behavior of pure Fe, Ni and Mo metals

From the result of the corrosion behavior of Fe-based and Ni-based alloys by means of the electrochemical method, major constituent elements such as Fe, Ni, and Mo are considered to have a significant influence on the corrosion behavior in NaCl-$CaCl_2$

melt. In order to investigate the corrosion process of these metals, LP and EIS measurements were performed using pure Fe, Ni, and Mo substrates. Figure 6-6 shows the LP curves and Fig. 6-7 shows the Nyquist plots of pure Fe, Ni, and Mo metals. Table 6-4 summarize the corrosion rates calculated based on Eq. (6-1). As can be seen in Table 6-4, pure Mo and Ni metals exhibited the lowest corrosion rate and highest charge transfer resistance, while pure Fe metal exhibited poor corrosion resistance in both LP and EIS measurements. One reason for the poor corrosion behavior of Fe metal was the formation of Fe_3O_4 phase, as evident from Fig. 6-8, which demonstrates XRD patterns of pure Fe and Ni plates before and after immersion for 18 h in NaCl-$CaCl_2$ melt. In the same condition, a phase transition of the Ni plate did not occur.

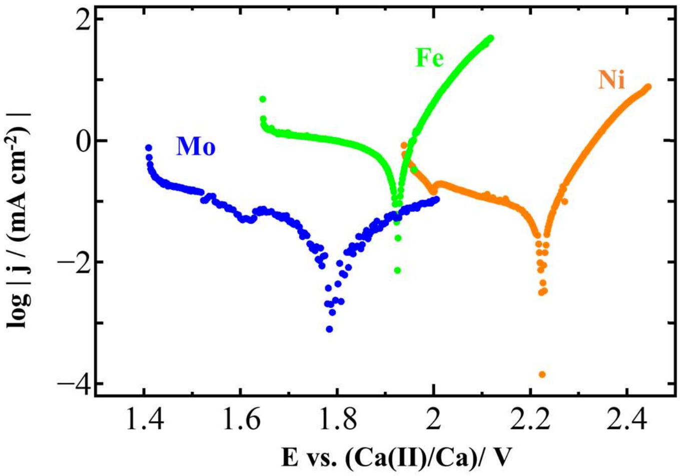

Figure 6-6. Linear sweep polarization curves of pure metals (Fe, Ni, and Mo).

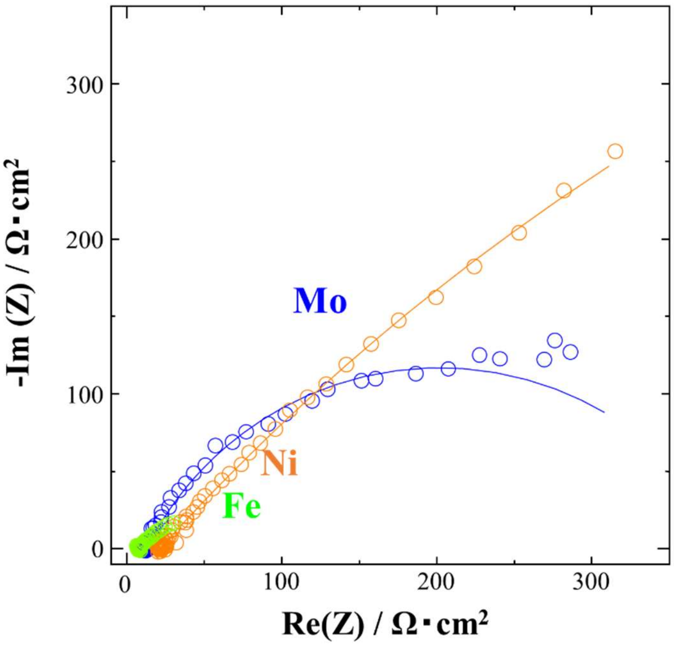

Figure 6-7. Nyquist plots of pure metals (Fe, Ni, and Mo).

Table 6-4. Corrosion data of pure metals (Fe, Ni, and Mo).

Sample	E_{corr} / V	I_{corr} / µA cm^{-2}	Corrosion rate / mm $year^{-1}$	R_{ct} / Ω cm^2
Fe	1.93	644	7.47	154
Ni	2.23	62.4	0.670	3.51×10^3
Mo	1.79	30.0	0.300	604

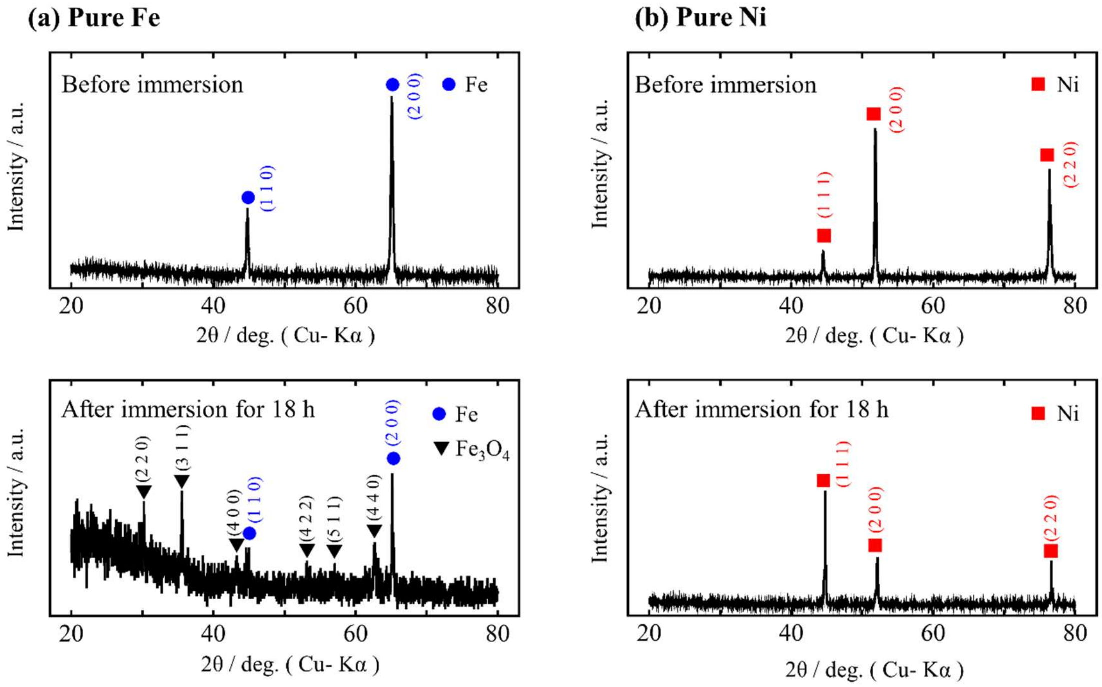

Figure 6-8. XRD patterns of pure Fe and Ni plates before and after immersion for 18 h in NaCl-$CaCl_2$ melt.

6.4. Conclusions

In this chapter, the corrosion behavior of stainless steels (SUS304, SUS316, and SUS430), Ni-based alloys (Inconel600, InconelX750, and HastelloyC-276), and Incoloy800 in NaCl-$CaCl_2$ melt at 823 K was investigated by electrochemical techniques. The LP technique revealed that Ni-based alloys have higher corrosion resistance than stainless steels, which was also indicated by EIS. HastelloyC-276 exhibited the lowest corrosion rate, 0.240 mm year^{-1}, which was estimated from corrosion current density. In addition, XRD analysis of pure Fe and Ni plates before and after immersion for 18 h into the melt indicated a reason for the poor corrosion behavior of Fe metal was the formation of the Fe_3O_4 phase.

References

[1] A. Meurisse, J. Carpenter, “Past, present and future rationale for space resource utilisation”, Planet. Space Sci., **182**, 104853 (2020).

[2] N. Yamashita, N. Hasebe, R. C. Reedy, S. Kobayashi, Y. Karouji, M. Hareyama, E. Shibamura, M. N. Kobayashi, O. Okudaira, C. d’Uston, O. Gasnault, O. Forni, K. J. Kim, “Uranium on the Moon: Global distribution and U/Th ratio”, Geophys. Res. Lett., **37**, L10201 (2010).

[3] J. J. Hagerty, D. J. Lawrence, B. R. Hawke, L. R. Gaddis, “Thorium abundances on the Aristarchus plateau: Insights into the composition of the Aristarchus pyroclastic glass deposits”, J. Geophys. Res., **114**, E04002 (2009).

[4] Tim. Abram, S. Ion, “Generation-IV nuclear power: A review of the state of the science”, Energy Policy, **36**, 4323 (2020).

[5] I. K. Aji, T. Tatsuya, M. Kinoshita, T. Okawa, “An Experimental and Numerical Study of Wall Effect on Freeze Valve Performance in a Molten Salt Reactor”, J. Nucl. Eng. Radiat. Sci., **6**, 1 (2020).

[6] M. Taira, Y. Arita, M. Yamawaki, “The Evaporation Behavior of Volatile Fission Products in FLiNaK Salt,” J. Sci. Technol., **5**, 1 (2017).

[7] M. Yamawaki, Y. Arita, K. Fukumoto, M. Taira, “Evaluation study of source term for severe accident analysis of molten salt reactors,” J. Plasma Fusion Res. Ser., **11**, 113 (2015).

[8] M. Yamawaki, T. Koyama, “Reducing the Burden of High Level Radioactive Waste with Transmutation —Proposal of Integral Molten Salt Fast Reactor (IMSFR),” J. Nucl. Radiochem. Sci., **16**, 1 (2016).

[9] K. Vignarooban, P. Pugazhendhi, C. Tucker, D. Gervasio, A.M. Kannan, “Corrosion

resistance of Hastelloys in molten metal-chloride heat-transfer fluids for concentrating solar power applications”, Sol. Energy, **103**, 62 (2014).

[10] J. C. Gomez-Vidal, A. G. Fernandez, R. Tirawat, C. Turchi, W. Huddleston, “Corrosion resistance of alumina forming alloys against molten chlorides for energy production. II: electrochemical impedance spectroscopy under thermal cycling conditions” Sol. Energy Mater. Sol. Cell., **166**, 234 (2017).

[11] A.G. Fernández, L.F. Cabeza, “Corrosion evaluation of eutectic chloride molten salt for new generation of CSP plants. Part 1: Thermal treatment assessment”, J. Energy Storage, **27**, 101125 (2020).

[12] S. Guo, W. Zhuo, Y. Wang, J. Zhang, “Europium induced alloy corrosion and cracking in molten chloride media for nuclear applications”, Corros. Sci., **163**, 108279 (2000).

CHAPTER 7

Corrosion of Behavior of JLF-1 Steel in LiF-NaF-KF Melt

7.1. Introduction

As mentioned in Chapter 6, Ni-based alloys, especially the Hastelloy alloy, exhibited high corrosion characteristics in a chloride melt. However, from a perspective of in-situ resource utilization on the moon, Fe-based materials are more suitable than Ni-based materials because of their abundance in the lunar regolith, as shown in Table 1-1. In this chapter, JLF-1 steel (Fe-9Cr-2W, a RAFM steel) is the focus as the structural material for a nuclear fission or fusion reactor.

High temperature molten salt is a candidate for the liquid blanket in a nuclear fission or fusion reactor [1–3]. In order to construct these infrastructures as a long-term power generation system on the moon and Mars, a robust structural material in molten salts is needed. Fluoride melt, as well as chloride melt, is a candidate for the liquid blanket. For example, LiF-NaF-KF melt is expected to be the liquid blanket at present. As for the structural material, RAFM steels are proposed as structural materials for the blanket. Kondo et al. [4, 5] have shown good compatibility between JLF-1 steel and LiF-NaF-KF melt under limited conditions. In order to understand these corrosion behaviors and extend them to the blanket condition, the elementary process of corrosion must be revealed by microstructural observations and electrochemical measurements.

As discussed in Chapter 6, electrochemical measurements are advantageous for determining a corrosion process as an electrochemical response, although, conventional weight change measurement requires a long time. EIS is the other method previously discussed for evaluating corrosion behavior of metals in molten salt. For example, it has been reported that the corrosion mechanism of major constituent elements of austenitic steels in a LiF-NaF-KF melt at 973 K could be evaluated by EIS with their equivalent circuits [6]. In this chapter, the electrochemical corrosion characteristics of JLF-1 steel was investigated in the LiF-NaF-KF melt at 773 K. Moreover, the constituent elements of JLF-1 steel, Fe, Cr and W, were measured by the EIS method in order to discuss the fundamental corrosion processes of JLF-1 steel in the melt.

7.2. Experimental

LiF (98.0%, FUJIFILM Wako Pure Chemical Corporation), NaF (99.0%, FUJIFILM Wako Pure Chemical Corporation), and KF (99.0%, FUJIFILM Wako Pure Chemical Corporation) were used as the starting materials. The reagents were mixed in eutectic compositions and then the powder was kept under vacuum for more than 48 h at 473 K to eliminate any water. The LiF-NaF-KF mixture was melted at 773 K in an alumina crucible and kept under an Ar gas flow for 12 h or more.

Disks of JLF-1 steel (Fe-9Cr-2W, detailed chemical composition is described in Table 7-1 [7]), pure Fe (purity 99.99%), pure Cr (purity 99.99%), pure W (purity 99.9%) and pure Ni (purity >99%) were mechanically polished with a diameter of 6.0 mm and a thickness of 0.3 mm. A disk with a pure Ni wire (purity >99.9%) connected by spot welding and ultrasonically cleaned in acetone was used for the immersion test. The disk part of the sample was completely immersed in LiF-NaF-KF melt.

Table 7-1. Chemical composition of JLF-1 steel (wt%) [7].

Fe	Cr	W	C	Mn	V
Bal.	9.00	1.98	0.09	0.49	0.20
Ta	O	N	P	S	
0.083	0.0019	0.0150	< 0.003	0.0005	

Figure 7-1 shows a schematic illustration of the experimental apparatus. The working electrode, the reference electrode, and the counter electrode were the tested samples, a pure Ni wire, and a glassy carbon rod (99.9999%, ~3-mm in diameter, ~1.5-cm in length was immersed), respectively. The pure nickel wire acted as a QRE. All the electrodes were connected to a potentiostat/galvanostat (VSP, BioLogic). For EIS, the samples were immersed into the LiF-NaF-KF melt and 10 min later the frequency changed from 10 kHz to 1 mHz with six points recorded per decade. The voltage amplitude for the alternating current was 10 mV. Based on the results, the equivalent circuits were estimated by EC-Lab (ver. 11.30, BioLogic) software.

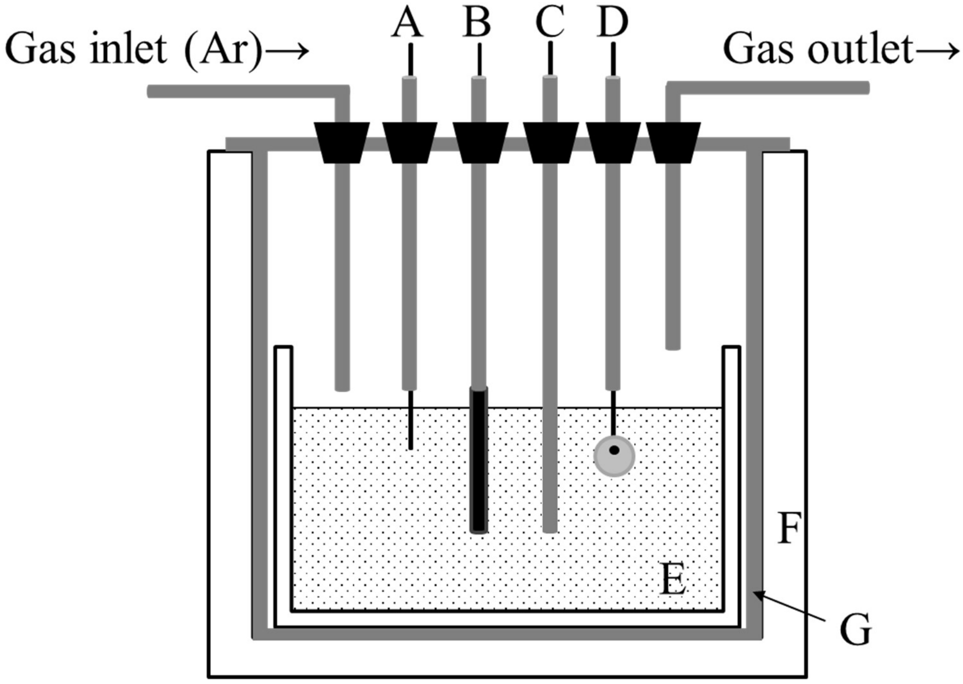

A: Quasi-reference electrode (Ni)
B: Counter electrode (glassy carbon)
C: Thermocouple
D: Working electrode (JLF-1 steel, Fe, Cr, W, and Ni)
E: Electrolyte (LiF-NaF-KF melt)
F: Electric furnace
G: Stainless steel holder

Figure 7-1. Schematic image of the apparatus of the electrochemical cell. The working electrode was the sample (JLF-1 steel and pure Fe, Cr, W, and Ni), the reference electrode was the pure Ni wire, and the counter electrode was the glassy carbon rod.

After the impedance measurement, all samples were ultrasonically cleaned in ion exchanged water and ethanol to observe sample surfaces by SEM (JSM-5600, JEOL Ltd.). The JLF-1 steel sample was picked up and thinned by focused ion beam fabrication to observe the cross section by TEM (JEM-2800, JEOL Ltd.) with EDS (JED-2300, JEOL

Ltd.).

7.3. Results and discussion

7.3.1. Electrochemical impedance spectroscopy

The JLF-1 steel, pure Fe, pure Cr, pure W, and pure Ni in LiF-NaF-KF melt at 773 K was investigated by EIS. Figure 7-2 shows Bode plots from 10 kHz to 10 mHz for each sample. In the figures, points and curves represent the experimental data and fitting results by the equivalent circuit, respectively, as shown in Fig. 7-3. From the results of EIS, charge transfer resistance, R_{ct}, was evaluated to be 96.1 Ω cm^2 for JLF-1 steel, 826 Ω cm^2 for Fe, 631 Ω cm^2 for Ni, 27 Ω cm^2 for Cr, and 382 Ω cm^2 for W. The Fe, Ni, and W substrates exhibited higher charge transfer resistance than JLF-1 steel. In general, R_{ct} is negatively correlated to the corrosion rate and, therefore, the higher the R_{ct} value, the higher the corrosion resistance. Thus, it has been found that in the LiF-NaF-KF melt, the corrosion resistance of JLF-1 steel was higher than that of pure Cr but lower than that of pure Fe, W, and Ni. Interestingly, unlike the EIS results in the NaCl-$CaCl_2$ melt, as discussed in Chapter 6, a different tendency was observed in the LiF-NaF-KF melt; pure Fe could have higher corrosion resistance in fluoride melts than in chloride melts. In addition, it is suggested that the presence of Ni and W elements in steels improve the corrosion resistance of JLF-1 steel in the fluoride melt. It should, however, be noted that the plotted data slightly deviated from the fitting curve, especially in the case of the Fe substrate. Thus, the morphological change of the samples was investigated.

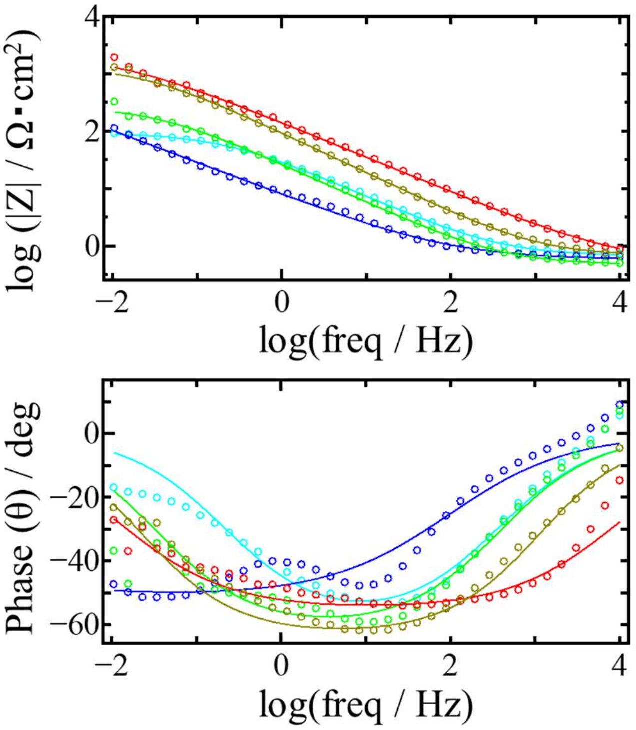

Figure 7-2. Bode plots of JLF-1 steel (green), pure Fe (blue), pure Cr (light blue), pure W (yellow), and pure Ni (red) in the LiF-NaF-KF melt at 773 K. Points represent the experimental data and solid lines represent fitting curves obtained using the equivalent circuit illustrated in Fig. 7-3.

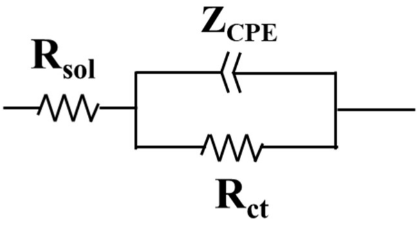

R_{sol} : solvent resistance
R_{ct} : charge transfer resistance
Z_{CPE} : Constant Phase Element

Figure 7-3. Equivalent circuit.

7.3.2. Surface analysis

Figure 7-4 exhibits the morphological surface changes of each sample by of SEM analysis. From Fig. 7-4, the corrosion characteristic of pure Fe was found to be intergranular corrosion at grain boundaries. Also, the corrosion behavior of pure Cr was found to be pitting corrosion with small pits with an average diameter of ~40 μm and large pits likely created by the merging of small pits. Since the morphological changes of Ni and W surfaces were small before and after the immersion test, the corrosion mechanism of pure W and Ni is entire surface corrosion. The corroded surface of JLF-1 steel slightly remained as prior austenitic grain boundaries with an average diameter of ~40 μm and packet boundaries with an average diameter of ~10 μm. Further, there were drop-out traces with an interval of 1 μm or less.

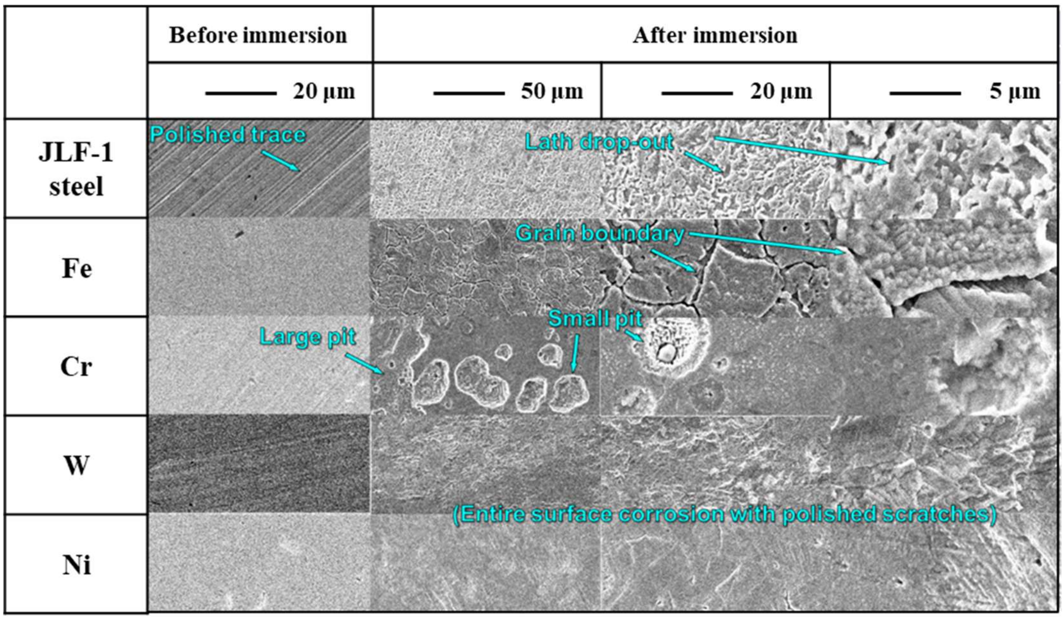

Figure 7-4. SEM images of JLF-1 steel and pure Fe, Cr, W and Ni before and after immersion for ~30 min in LiF-NaF-KF melt at 773 K.

Figure 7-5 illustrates the TEM cross-sectional image of JLF-1 steel after immersion for approximately 30 min in LiF-NaF-KF melt at 773 K. From Fig. 7-5, a drop-out area ~0.5-μm in size was observed. According to ref. [7], the lath width in the JLF-1 steel was found to have a size of 0.50 μm. Thus, the crack of JLF-1 steel, as shown in the top of Fig. 7-5, was the lath drop-out. From this result, the corrosion mechanism of JLF-1 steel was suggested to be intergranular corrosion, which was affected by the characteristic of Fe at lath boundaries, according to the following mechanism. In general, the mechanism of intergranular corrosion is explained by the electrochemical reactions at a grain boundary. EDS analysis at the lath boundaries revealed an area of Cr rich precipitations. It has been reported that the precipitation of carbides, $M_{23}C_6$ (M is Fe, Cr, W, etc.), at lath boundaries was observed in a similar RAFM steel [8]. Thus, these precipitations in the measurement were considered to be composed of chromium carbide, such as $Cr_{23}C_6$. Therefore, the electrochemical reaction at lath boundaries was considered to be oxidation of Cr, which resulted in the intergranular corrosion at the lath boundaries.

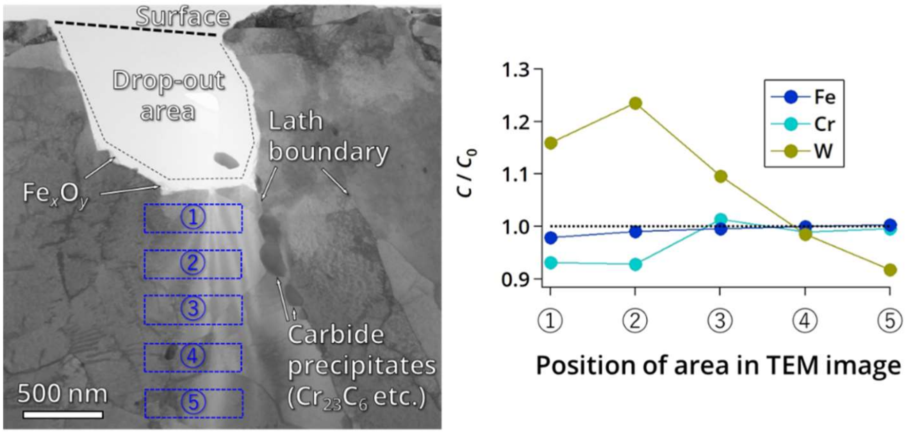

Figure 7-5. TEM image (left) and EDS chemical composition (right) of a cross section of JLF-1 steel after the impedance measurement. The Y-axis (C/C_0) is the concentration of each element after the impedance measurement divided by the initial concentration in Table 7-1.

The EDS analysis in Fig. 7-5 showed that the chemical composition of W in JLF-1 steel was higher at the surface than in the bulk. This result indicated that elemental Cr, which has low corrosion resistance from EIS measurements, dissolved into molten salt first, and Ni and W elements, which have high corrosion resistance, remained in the JLF-1 steel. Therefore, in order to develop a high corrosion resistance material in the LiF-NaF-KF melt, it is effective to reduce the Cr composition and increase the Ni and W composition in JLF-1 steel. However, in a fusion reactor environment, pure Ni creates voids and thus causes swelling [9]. Furthermore, Ni produces a long half-life nucleus by deuterium-tritium neutron irradiation. Thus, Ni use has been avoided in fusion blankets. On the other hand, pure W, which has high corrosion resistance from EIS, is a candidate for a fusion reactor component, such as a plasma facing wall [10]. Since pure W is not suitable as a structural material because of its brittleness, the results of this chapter recommend the utilization of W as a constituent element of steels in molten salt. For future work, corrosion characteristics of Fe-W alloys should be investigated to develop robust structural materials for a lunar nuclear fusion reactor that uses molten fluoride salts.

7.4. Conclusions

In this chapter, the corrosion characteristics of JLF-1 steel in fluoride melts were investigated. The corrosion processes of JLF-1 steel and its major constituent elements, Fe, Ni, Cr, and W, were investigated by EIS in a LiF-NaF-KF melt at 723 K, and by SEM, TEM, and EDS analysis. The results are summarized as follows.

(1) From the impedance measurement, Fe, Ni, and W metals exhibited higher charge transfer resistance than JLF-1 steel.

(2) The cross-sectional TEM image showed that the chemical composition of W in JLF-

1 steel was higher near the surface than in the bulk, which indicated higher corrosion resistance of W compared to Cr.

(3) The dominant corrosion mechanism of JLF-1 steel was intergranular corrosion at lath boundaries, which resulted in lath drop-out. For the constituent elements, intergranular corrosion at grain boundaries for pure Fe, pitting corrosion for pure Cr, and entire surface corrosion for pure W and Ni, was observed.

Future work should investigate the relationship between the composition of W in steels and corrosion phenomena to develop robust structural materials for molten fluoride blankets for a lunar nuclear fusion reactor.

References

[1] T. Ihli, T. K. Basu, L. M. Giancarli, S. Konishi, S. Malang, F. Najmabadi, S. Nishio, A. R. Raffray, C. V. S. Rao, A. Sagara, Y. Wu, "Review of blanket designs for advanced fusion reactors", Fusion Eng. Des., **83**, 912 (2008).

[2] R. R. Romatoski, L. W. Hu, "Fluoride salt coolant properties for nuclear reactor applications: A review", Ann. Nucl. Energy., **109**, 635 (2017).

[3] J. Miyazawa, H. Tamura, T. Tanaka, T. Murase, T. Goto, N. Yanagi, R. Sakamoto, A. Sagara, the FFHR Design Group, "Cartridge-Type Helical Blankets Aiming at Easy Construction and Maintenance for the FFHR-d1", Plasma Fusion Res., **12**, 1405017 (2017).

[4] M. Kondo, T. Nagasaka, V. Tsisar, A. Sagara, T. Muroga, T. Watanabe, T. Oshima, Y. Yokoyama, H. Miyamoto, E. Nakamura, N. Fujii, "Corrosion of reduced activation ferritic martensitic steel JLF-1 in purified Flinak at static and flowing conditions", Fusion Eng. Des., **85**, 1430 (2010).

[5] M. Kondo, T. Nagasaka, Q. Xu, T. Muroga, A. Sagara, N. Noda, D. Ninomiya, M. Nagura, A. Suzuki, T. Terai, N. Fujii, "Corrosion characteristics of reduced activation ferritic steel,JLF-1 (8.92Cr–2W) in molten salts Flibe and Flinak", Fusion Eng. Des., **84**, 1081 (2009).

[6] Y. X. Xu, Y. L. Wang, C. L. Zeng, "Electrochemical Studies of the Corrosion of Pure Fe, Ni and Cr in Molten (Li,Na,K)F", High Temp. Mater. Proc., **33**, 269 (2014).

[7] Y. Li, Q. Huang, Y. Wu, T. Nagasaka, T. Muroga, "Mechanical properties and microstructures of Chinalow activation martensitic steel compared with JLF-1", J. Nucl. Mater., **117**, 367 (2007).

[8] H. Tanigawa, H. Sakasegawa, R. L. Klueh, "Irradiation Effects on Precipitation

in Reduced-Activation Ferritic/Martensitic Steels", Mater. Trans., **46**, 469 (2005).

[9] T. Muroga, H. Watanabe, K. Araki, N.Yoshida, "Fission-fusion correlation of void swelling in pure nickel", J. Nucl. Mater., **155**, 1290 (1988).

[10] V. Philipps, "Tungsten as material for plasma-facing components in fusion devices", J. Nucl. Mater., **415**, S2 (2011).

CHAPTER 8

General Conclusions

High temperature molten salt plays a key role in power generation systems such as solar cells, nuclear fission reactor, and nuclear fusion reactor on the moon and Mars. In this thesis, the physicochemical phenomena of metallic atoms, metallic ions, and its oxides in molten halides were investigated in order to obtain fundamental knowledges for electrochemical/materials science and to develop electrochemical processing in molten salt for in-situ resource utilization. The significant effects of melt structure, melt composition, and interfacial flow phenomena on the Si electrodeposition process was discussed. The corrosion behavior of major alloys and a unique steel in molten halides was also discussed. The findings of this study indicate that fundamental properties such as thermophysical, electrochemical, and hydrodynamic property of molten salt have a significant effect on kinetic process of Si electrodeposition, transportation process of reactive metals at liquid metal cathode/liquid electrolyte interface, and corrosion process of structural materials. To develop the electrochemical processing for ISRU much further, fundamental data related to molten oxide electrolysis, inert anode materials, and materials tailoring under microgravitational environment should be acquired by means of computational chemical engineering and experimental study.

The results obtained in this study can be summarized as follows.

In Chapter 3, the effects of O^{2-} ions on the electrodeposition process of Si films in a molten LiF-NaF-KF melt were discussed. The reduction currents, which were attributed to the reduction of silicon ions, increased significantly by the addition of Li_2O; moreover, the thickness and current efficiency of the electrodeposited polycrystalline Si layer prepared by potentiostatic electrolysis was improved. These results indicated that the O^{2-} ions changed the coordination structure of silicon ions in molten fluorides and that the design of the molten salts bath is a key factor for fabricating high-quality Si layers with high current efficiency.

In Chapter 4, the melt structures of LiF-KF, LiF-NaF, and NaF-KF melts with SiO_2, were investigated through Raman spectroscopy and DFT calculations. The interactions between silicon ions and constituent ions of the fluoride melts were identified. The obtained spectra exhibited good agreement with the calculated data and two types of coordination structures were characterized: ion-like structure, such as $SiF_2O_2^{2-}$ and $Si_2O_5^{2-}$, and molecule-like structure, such as SiF_3O-Li and SiF_2O_2-2Li. Moreover, when Li_2O was added as a source of O^{2-}, remarkable bands attributed to the ion-like structure of $SiFO_3^{3-}$ and SiF_3O^- appeared in the Raman spectra. This indicated that O^{2-} ions have potential to promote the formation of oxyfluoride monomers by cleaving the Si-O-Si bands of $Si_2O_5^{2-}$ ions or SiO_2.

In Chapter 5, unique interfacial phenomena on liquid metal cathodes were investigated. To visualize the liquid electrolyte/liquid metal cathode interface, a low temperature aprotic electrolyte, PC, and a low melting point metal, Ga, was used as the cathode. Li electrodeposition on the liquid Ga substrates was carried out in PC-$LiClO_4$ at

40 °C. It was found that interfacial flow phenomena were induced by differences in interfacial tension between the liquid Ga and the liquid Ga-Li alloy formed on the substrate under potentiostatic electrolysis at −1.0 V (versus Li^+/Li), which caused interfacial shape change of the liquid Ga electrode. Moreover, a significant difference in electrochemical response between liquid and solid Ga substrates was also noticed while employing the current-time transient technique. These experimental results suggest that the process of liquid Ga-Li phase formation, by the dissolution of electrodeposited Li atoms into the liquid Ga substrate, dominated during the initial stage of Li electrodeposition. In addition, the electrochemical behavior of silicon ions on the liquid Ga substrate followed similar behavior to those recorded in the PC-$LiCl_4$ system, suggesting dynamic instability at the liquid metal/liquid electrolyte interface during Si electrodeposition. These results provide new insight into the design of electrochemical processing involving a liquid electrolyte/liquid metal interface.

In Chapter 6, the corrosion characteristics of stainless steels (SUS304, SUS316, and SUS430), Ni-based alloys (Inconel600, InconelX750, and HastelloyC-276) and Incoloy800 were investigated in a NaCl-$CaCl_2$ melt at 823 K to evaluate corrosion resistance of structural materials. Electrochemical techniques revealed that Ni-based alloys have higher corrosion resistance in the melt than Fe-based alloys. HastelloyC-276 exhibited the lowest corrosion rate, 0.240 mm $year^{-1}$, which was estimated from corrosion current density by LP measurements. Moreover, surface analysis indicated that the reason for the poor corrosion properties of Fe metal was the formation of the Fe_3O_4 phase.

In Chapter 7, JLF-1 steel was investigated as a unique structural material for nuclear fusion reactors. The corrosion processes of JLF-1 steel and its major constituent elements (Fe, Ni, Cr, and W) in LiF-NaF-KF melt at 723 K were discussed by means of EIS, SEM, TEM, and EDS analysis. The results showed the chemical composition of W in JLF-1 steel was higher near the surface than in the bulk after immersion, which indicated higher corrosion resistance of W. Also, the dominant corrosion mechanism of JLF-1 steel was intergranular corrosion at lath boundaries, which resulted in lath drop-out. It was found that the composition of W in steels plays a key role in developing robust structural materials in molten fluoride for lunar and Martian nuclear fusion reactors.

List of Publications

The main parts of this thesis have been published, or are being submitted for publication, as follows.

Y. Suzuki, M. Yokota, Y. Sakanaka, Y. Fukunaka, T. Goto, "Electrodeposition of Si in Molten LiF-NaF-KF Mixed with Various Sized SiO_2 Particles", ECS Trans., **80**, 823 (2017).

Y. Suzuki, Y. Fukunaka, T. Goto, “Interfacial phenomena associated with Li electrodeposition on liquid Ga substrates in propylene carbonate”, Electrochem. Commun., **100**, 20 (2019).

Y. Suzuki, Y. Inoue, M. Yokota, T. Goto, “Effects of Oxide Ions on the Electrodeposition Process of Silicon in Molten Fluorides”, J. Electrochem. Soc., **166**, D564 (2019).

Y. Suzuki, T. Park, K. Hachiya, T. Goto, “Raman Spectroscopy for Determination of Silicon Oxyfluoride Structure in Fluoride Melts”, J. Fluorine Chem., **238**, 109616 (2020).

G. Yamazaki, Y. Suzuki, T. Goto, T. Nagasaka, D. Nagata, J. Shen, K. Saito, T. Watanabe, “Microscopic corrosion process and electrochemical property of JLF-1 steel (Fe-9Cr-2W) in the molten salt, LiF-NaF-KF”, Fusion Sci. Technol., submitted.

Acknowledgments

The author would like to thank Prof. Takuya Goto for his constant supervision over all the chapters of this thesis and for fruitful discussions, helpful advice, and great support throughout my Ph.D. study.

The author would like to extend my sincere appreciation to Prof. Masatsugu Morimitsu for his valuable advice and suggestions. The author would like to thank Prof. Yuko Inatomi for his fruitful discussions and valuable comments.

Special thanks are given to Prof. Yasuhiro Fukunaka for his helpful instructions on this thesis and kind encouragement throughout my Ph.D. study.

The author would like to thank Prof. Kan Hachiya for his help on experimental techniques and discussions of the results.

The author would like to thank all the members of Prof. Goto's laboratory for their help, lively discussions, and warm encouragement throughout the study.

Finally, I would like to thank my parents and sister for their deep understanding and support.

Yuta Suzuki

March 2021